Implementation of SELEX technique on Lab-on-Chip systems

Department of Information, Electronics and Telecommunication Engineering

PhD degree in Information and Communication Technology – XXIX Cycle

Candidate
Giulia Petrucci
ID number 1148027

Thesis Advisor
Prof. Domenico Caputo

A thesis submitted in partial fulfillment of the requirements
for the degree of Doctor of Philosophy in Information and Communication Technology

January 2017

Thesis defended on February 27th, 2017
in front of a Board of Examiners composed by:

Prof. Piero Tognolatti
Prof. Fortunato Santucci
Prof. Eugenio Martinelli
Prof. Elena Pettinelli
Prof. Elio Di Claudio

Implementation of SELEX technique on Lab-on-Chip systems
Ph.D. thesis. Sapienza – University of Rome

This thesis has been typeset by LaTeX and the Sapthesis class.

Version: March 1, 2017

Author's email: giulia.petrucci@uniroma1.it

Contents

List of Figures

List of Tables

Introduction

This thesis presents the design and the experimental development of a compact and high sensitive Lab-on-Chip (LoC) system suitable for the implementation of SELEX technique. SELEX (Systematic Evolution of Ligands by EXponential enrichment) is a combinatorial technique used in molecular biology to produce copies of the same nucleotide and to select a strand of DNA (aptamer) specific for a target molecule. The proposed Lab-On-Chip system includes the following functional units: an amplification module based on the PCR technique; a separation module able to obtain a single strand DNA from a double strand DNA and a selection module for the specific selection of the aptamer. These functionalities are implemented combining microfluidic components (micro-channels and micro-valves), electronic devices (amorphous silicon photosensors, thin film heaters, temperature sensors) and bioanalytical procedure. Notwithstanding, there are several challenges and limitations on the way that need to be appropriately addressed. For these reason it will become evident that the different module developments go hand-in-hand and need for a multidisciplinary approach.

The work is part of a project involving the amorphous Silicon Devices and Systems Group (aSiDaS) from "Sapienza" University of Rome. In particular the experiment took place thanks to the Laboratory of Microelectronic Technologies and the Characterization Laboratory at DIET- Sapienza (Department of Information, Electronics and Telecommunication Engineering) and the Department of Chemistry at "Sapienza" University of Rome.

Thesis outline

The thesis includes the Introduction, five main chapters and the Conclusions.
The *Introduction* presents the abstract of the thesis and overviews the basic concepts of (i) Lab-on-Chip, (ii) Microfluidics, (iii) Aptamers and (iv) SELEX technique.
Chapter 1 describes our idea of SELEX process whose detailed steps are established according to the biological requirements. A first design of the SELEX chip is presented: a glass substrate including electronics devices and microfluidic network.
Chapter 2 presents the design of a multifunctional platform, the DARWIN'S (DNA Amplification Reactor With Integrated Network (of) Sensors), that can be used to test the functional modules of the SELEX chip. This platform hosts thin film heater for thermal treatment and amorphous silicon sensors for temperature control and on chip detection.
In *Chapter 3*, after a general introduction on microfluidics, the design and fabrication

of the microfluidic part is presented. The results achieved during my staying in the laboratory of the INESC-MN (Instituto de Engenharia de Sistemas e Computadores para os Microsistemas e as Nanotecnologias) research center in Lisbon are also reported.

The experiments with the DARWIN'S platform for the different SELEX modules are described in *Chapter 4*. Experiments performed on other topics related to my PhD project are also presented.

Taking into account all the experimental results, *Chapter 5* presents the chip design for the totally integrated SELEX process.

Finally the Conclusions summarize the achievements of the thesis alongside the suggestions for future work.

Lab-on-Chip

Lab-on-Chip are miniaturized systems able to perform biomolecular analysis in shorter time and with lower reagent consumption than a standard laboratory [50]. When fully developed, a LoC contains elements for the acquisition, pretreatment, separation, post-treatment and detection of a variety of samples. The most important advantage is the possibility to create complete analytical microsystems by downsizing and by integrating various functional modules into a single device yielding a sensor-like system with fast response time, low sample consumption and on-site operation [58]. Such functional modules may include those capable of samples injection, reaction, separation and detection.

This technology is gaining great interest due to the many possibilities that it offers in the fields of life sciences, from parallel analysis in genomics [37]; [39] to point-of-care devices [48] in medical diagnostics.

It was in 1990 that the concept of "miniaturized total chemical analysis system" was proposed by Manz et al. [58]. In that silicon chip analyzers incorporating sample pretreatment, separation, and detection played a fundamental role. It was envisioned as a new concept for chemical sensing, needed since sensors at that time were not providing the best results in terms of selectivity and lifetime. Initially, the main reason for miniaturization was therefore to enhance the analytical performance of the device rather than to reduce its size. However, it was also recognized that a small size presented the advantage of a smaller consumption of carrier, reagent, and mobile phase.

Moreover, the total chemical analysis system scheme provided an integration of separation techniques that could enable the monitoring of many components within a single device. Such a system was envisioned capable of performing sample handling, analysis (e.g., chromatography, electrophoresis), and detection and incorporating control of mass transport and measurements.

Many of the functions implemented by a LoC often require a thermal control of the process, which is frequently implemented by thin film heaters with integrated temperature sensors. Typical applications include flow control through thermally actuated micro pumps [101] and/or micro valves [102], or temperature control in bio analysis applications, as for example in the Polymerase Chain Reaction (PCR) technique [46]; [100].

Microfluidics

The simplest and most straightforward – although trivial – way of introducing the topic of microfluidics is by its definition: microfluidics is the field of science and engineering that deals with the controlling and handling of fluids in micron-sized structures, which translates into volumes in the order of the *μl-nl* [97]. These structures are typically channels, wells or chambers, that are used as fluid routers, reactions zones or cell growing areas.

The most immediate advantages of microfluidics are related to scale: when compared to equivalent macroscopic systems, only a fraction of the reagents are required, devices have a smaller footprint, some reactions times are improved and huge parallelization can be achieved in a small area [36]; [62]. Some other, perhaps more subtle, advantages are related to how physical phenomena change when scaling down from macro to microscale. In the analytical microsystems the miniaturization is more than a simply downscaling of well-known systems since the relative importance of forces and processes changes with scale. In order to describe the behavior of these systems one approach employed dimensionless parameters to correlate in an easy way experimental results when a great deal of variables are involved and are defined in terms of parameters that are assumed to be constant through the whole system under study. The Reynolds number, for example, used to characterize laminar and turbulent flow regimes, is one of the dimensionless parameters well known in fluidics and widely used in the design of a LoC. In fact, a relevant feature of these devices is the possibility of handling fluidics on the nanoliter and even picoliter scale by using microfluidics techniques.

Microfluidics stepped into the limelight in the late 1990's with the development of rapid prototyping and soft lithography techniques [26]; [99], which allowed devices to be built faster and cheaper. These techniques also introduced materials such as polydimethylsiloxane (PDMS), that is currently the elastomer of choice for the fabrication of the vast majority of microfluidic devices [74]. Since the time when the first LoC has been proposed, stacked modular devices in silicon and plexiglass were designed and tested in an effort to surpass the limitations in the integration of valves, pump, and detection systems, in miniaturized flow injection analysis [32]. Also Electroosmotic pumps, characterized by the absence of mechanically moving parts, were directed to optimized injection and separation procedures by the switching of voltages between reagents, mobile phase and waste reservoirs [59]. One of the cornerstones of microfluidics has always been its biological applications [98], and throughout the last decade microfluidic devices have grown in complexity. Nowadays, not only they provide viable alternatives to macroscopic platforms, they are also able to efficiently tackle problems for which typical macroscopic approaches offer no practical solution.

Aptamers

Conventional immunochemical assays, based on the specific recognition process between an antibody and an antigen, are widely applied to clinical diagnostics, environmental analysis and food safety assessment [56]. Examples of experimental

applications that use antibodies are Western blot, Immunohistochemistry and Immunocytochemistry, Enzyme-Linked Immunosorbent Assay (ELISA), Lateral Flow Immunoassay, Immunoprecipitation, and Flow Cytometry. Recently, the use of aptamers instead of antibodies, as recognition and detection molecules, has been shown advantageous. Aptamers are artificial single-stranded DNA or RNA sequences (more recently, peptides) that fold into secondary and tertiary structures making them various target ligands, including small-molecule drugs, peptides, proteins and cells, with extremely high affinity and specificity [45]; [85].

While analogous to antibodies, and having dissociation constants in the nanomolar range (similar to monoclonal antibodies), the use of aptamers as receptors has been shown to be advantageous over the antibodies in certain scenarios. First, aptamers are selected in vitro by biomolecular technique (SELEX- Systematic Evolution of Ligands by EXponential enrichment) overcoming the use of cell lines or animals, as it is necessary for antibody generation. Second, aptamers, once selected, can be synthesized chemically, allowing their relatively low cost, large-scale production with high purity and low batch-to-batch variability. Third, aptamers are more stable to temperature and pH than antibodies. Aptamers have been widely applied for detection of several targets both in solution and coupled to different nanomaterials to generate aptamer-based sensors (aptasensors) that exhibit high sensitivity as well as specificity [20].

SELEX technique

SELEX was independently developed by two laboratories of Ellington and Szostak (1990) and Tuerk and Gold (1990) more than two decades ago. Since then, it is has undergone numerous modifications and improvements. The conventional SELEX is a well-described technology [95]. Generation of aptamers using this method lasts from few weeks up to a month. Several selection steps are introduced during conventional SELEX depending on the type of the desired aptamer (see Table 0.1).

Conventional SELEX is a well-established and effective method but due to its large time- and labor-consumption, continuous development of alternative methods for aptamer selection has been inevitable [61]; [24].

Generally the SELEX process starts with the generation of a random library with a great number of random nucleotide sequences (10^{13}-10^{16}), which are incubated with the desired target molecule under conditions suitable for binding. Next, the unbound single-stranded DNA (ssDNA) are partitioned from those bound specifically to the target molecule, then eluted from the target molecules, while the molecules bound specifically to the target molecule are first unbounded from the target, then amplified by polymerase chain reaction (PCR). This procedure is reiterated for multiple rounds (typically 8-15) until the bound sequences are enriched. SELEX process requires the use of bulky equipment such as shaker and PCR machines and the use of large amount of reagents and samples. Recently, literature shows an increased interest in developing miniaturized platforms, which combine microfluidic and micro-electromechanical systems (MEMS) technologies for the miniaturization and automation of the SELEX process with implications in terms of reduction of time and improved efficiency of the whole process. These systems are based

Table 0.1. SELEX methods to select aptamers.

SELEX Method	Description	Reference
FluMag-SELEX	Aptamers are selected from a library modified with fluorescein. In addition, the target is immobilized on magnetic beads as opposed to agarose.	[87], [88]
Microfluidic SELEX	Aptamers are selected on a miniature, automated SELEX platform based on microfluidic technologies	[44], [55],[42]
Generic SELEX	Neither specialized equipment or significantly adapted methods were used compared to the original selection experiments	[30], [75], [29], [95]
Cell-SELEX	Methods were adapted specifically for the selection of aptamers that have affinity for whole cells	[83], [19], [80]
CE-SELEX (capillary electrophoresis SELEX)	In this method, partitioning of bound and non-specific binding oligonucleotides is performed using capillary electrophoresis	[53], [63], [94], [27]
Non-SELEX	Aptamers are selected after multiple steps of partitioning but without amplification	[7], [6], [2]
Automated SELEX	Aptamers are selected within an automated system, decreasing labour and processing time	[43], [18], [35], [31]

on microfluidic chip in which magnetic beads functionalized and located into a microfluidic channel are brought into contact with the target molecule [42]; [54]. Other works, as reported in Table 0.1, also show the aptamer selection by coated magnetic nanoparticles, PCR amplification and double stranded DNA (dsDNA) denaturation in the same chamber of a single microfluidic chip [55].

In order to improve the SELEX process in terms of time and costs, in this work we focused on the development of a versatile device for DNA amplification and dsDNA separation, which can be used in combination with the standard SELEX process and in perspective, incorporated within a full on-chip integrated SELEX system.

Since SELEX implies interdisciplinary know-hows, different collaborations have been started with the Genomic Technologies Laboratory of CNR- Institute of Clinical Physiology -IFC-CNR- PISA (Dr. Lorena Tedeschi and Prof. Claudio Dominici), the Department of Chemistry at "Sapienza" University of Rome (Dr. Francesca Costantini, PhD) and the Department of Chemistry and Institute of Biochemistry at Carleton University- Ottawa (Prof. Maria DeRosa, Ph.D).

Keywords: Lab-on-Chip, SELEX, a-Si:H sensors, Thin film technologies, Heaters, Microfluidics, PDMS, micro valve, PCR, DNA, Surface functionalization.

Chapter 1

Proposed SELEX

The proposed SELEX is implemented combining microfluidic components (micro-channels and micro-valves), electronic devices (amorphous silicon photosensors, thin film heaters, temperature sensors) and bioanalytical procedure. The main functional units are:

a) a selection module for the specific selection of the aptamer. This module is constituted by a glass surface functionalized with polymer brushes that is able to immobilize the target molecules (Fig. 1.1);
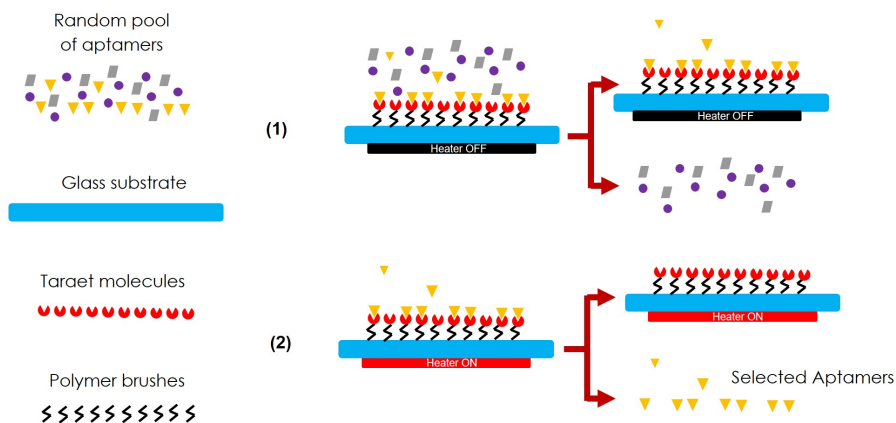
Figure 1.1. Schematic representation of SELEX positive selection. The random pool is incubated with the target molecules (1): unbound molecules are flushed away to the waste and the selected aptamers are collected from the target/DNA complex heating the solution (2).

b) an amplification module based on the Polymerase Chain Reaction (PCR) technique. This is a microfluidic chamber where all the ingredients for the DNA amplification are mixed. In particular, the double DNA strands have a fluorescent molecule at one end and a biotin molecule at the other end (Fig. 1.2);
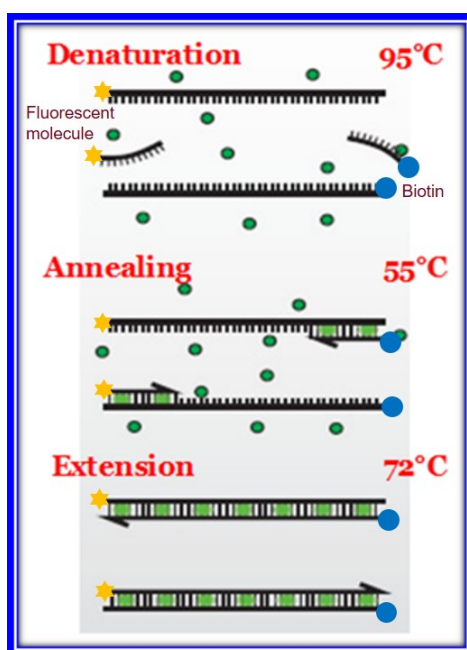
Figure 1.2. Schematic representation of SELEX PCR steps: denaturation, annealing and extension.

c) a separation or denaturation module able to obtain a single strand DNA from the amplified double strand DNA. This is made of a glass substrate functionalized with polymer brushes able to immobilize molecule of streptavidin (Fig. 1.3).
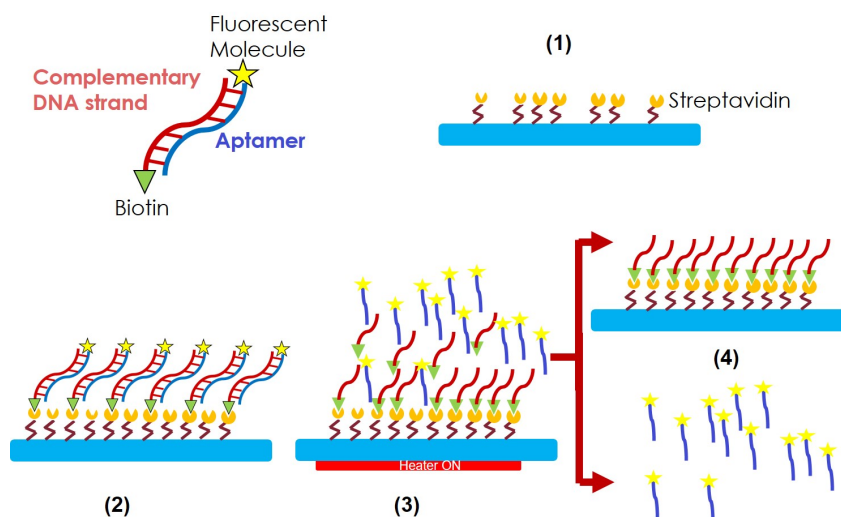
Figure 1.3. Schematic representation of SELEX separation module. The DNA strand with biotinylated end binds to the immobilized streptavidin molecules (2). Heating the solution (3), ssDNA are released and collected by flushing a buffer solution (4).

I now want to go into rather more detail regarding these steps. The sample is constituted by a random pool of aptamers containing the desired aptamer. The starting point is a sample pretreatment with an off-chip step. The first on-chip step is the polymerase chain reaction. It is a technique used in molecular biology to amplify a single copy or a few copies of a piece of DNA across several orders of magnitude, generating thousands to millions of copies of a particular DNA sequence. The method relies on thermal cycling, consisting of cycles of repeated heating and cooling of the reaction for DNA melting and enzymatic replication of the DNA. Primers (short DNA fragments) containing sequences complementary to the target region along with a DNA polymerase are key components to enable selective and repeated amplification. The primers and reagents used in these PCR cycles are designed in such a way that the amplified ds-DNA will have at one end a fluorescein molecule and at the other end a biotin molecule (see Fig. 1.2).

After this amplification step, it is necessary that these ds-DNAs become single strand in order to be captured by the target molecule. This separation will be implemented taking advantage of the strong bond between *streptavidin* and *biotin*: streptavidin molecules are immobilized on the surface and when the ds-DNA is injected, biotin binds to the streptavidin (see Fig. 1.3(2)). Heating this site at 90-95°C causes the separation of the two strands while it is not able to break the biotin-streptadivin bond. The injection of a buffer solution will move the ss-DNA labeled with the fluorescent molecule towards the following site whose surface hosts the target molecules, leaving the ss-DNA labeled with biotin attached to the immobilized streptavidin.

The selection of the specific aptamer occurs through three types of methods (positive, negative and competitive), shown in Fig. 1.4.
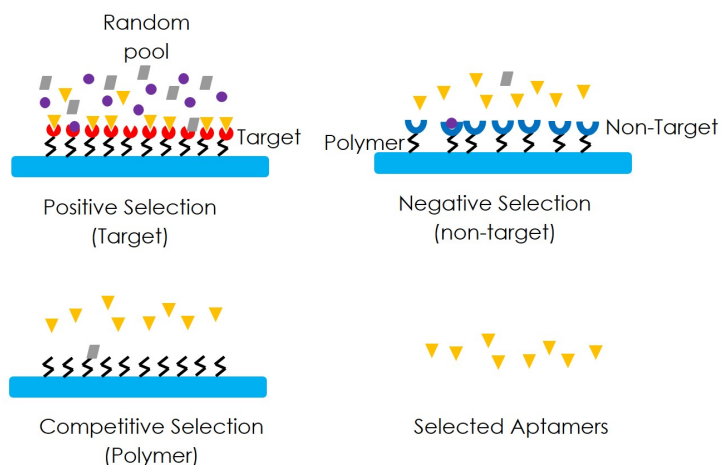
Figure 1.4. Different selection steps: in the upper part, positive and negative selection, with target molecules and non target molecules respectively immobilized on polymer brushes; in the bottom part, competitive selection (glass substrate functionalized with only polymer) and resulting amplified aptamers.

The site devoted to the positive selection will be functionalized with the target molecules (reported in red in Fig. 1.4); the site for the negative selection will be functionalized with a non-target molecule (reported in blue in Fig. 1.4); the site for the competitive selection will be functionalized only with polymer (black lines).

In the positive selection, aptamers (ss-DNA labeled with the fluorescent molecule) bind to the target immobilized on the surface, the non-specific amplified DNA or other PCR products should not attach to the target molecules. Any non-binders are eliminated by means of washing solution, leaving attached only the specific aptamer. By the injection of a buffer drop and its heating, it is possible to break the hydrogen bonds holding the aptamers onto the target and move the drop of buffer containing the single strand DNA towards the site where a new PCR can occur. The negative and competitive selections are utilized only to increase the purity of the aptamer and therefore can be used only in the last SELEX cycles.

The detailed on-chip SELEX operation steps have been established according to these biological requirements leading to the flow-chart reported in Fig. 1.5.

In particular the steps are:

- Off-chip pre-treatment of the sample (containing the single strand DNA labeled with a fluorescent molecule and the complementary single strand DNA labeled with the biotin);

- Injection of the pre-treated sample drop into the *amplification site*;

- Injection of the PCR reagents;

- PCR implementation;

- Movement toward the *separation site* of the PCR products;

- Incubation for a determined amount of time to allow the interaction streptavidin-biotin;

- Elimination of any PCR waste products (washing water at T_{amb});

- Separation of ds-DNA by heating (at 90-95°C) and movement toward the *selection site* of the ss-DNA;

- Formation of binding between aptamers and target;

- Elimination of any non-binders by means of washing solution. This should leave the binders (aptamers) behind;

- Injection of a drop of buffer and its heating to break any hydrogen bonds holding the aptamers onto the target;

- Movement of the drop of buffer containing the single strand DNA toward the *amplification site* where PCR can occur;

- Injection of the PCR reagent;

- PCR implementation;

- . . .
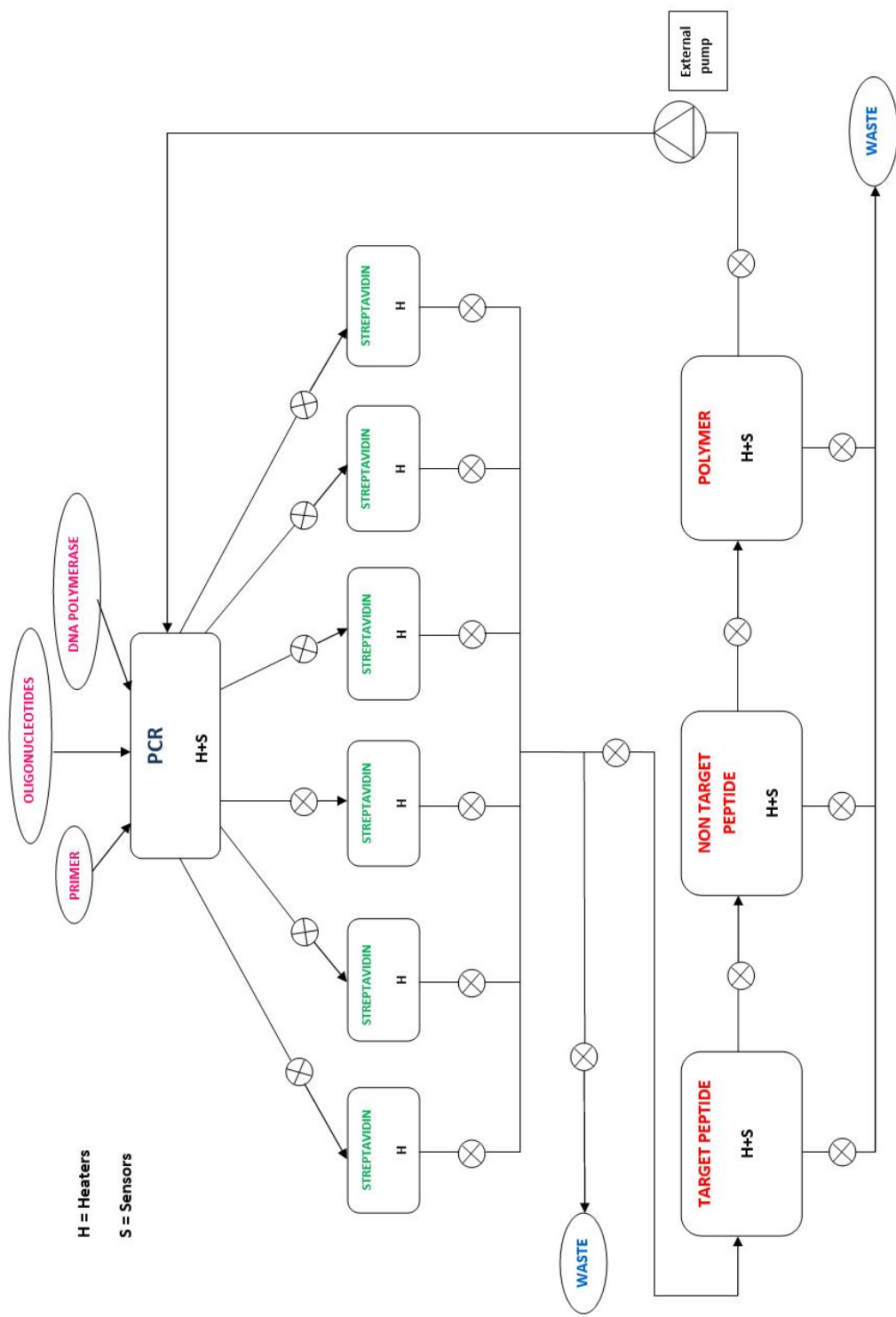
Figure 1.5. Flow-chart of the proposed SELEX steps.

These steps will be implemented n times to enhance the purity and amount of selected aptamers. After n cycles we obtain the desired amplified aptamers. The biotin-streptavidin bond is very difficult to break without damaging other polymers or other structures on the glass. Therefore, it is not possible to use the same separation site more than once and a number of these sites equal to the SELEX cycles is necessary.

A possible implementation of the system on a glass substrate including microfluidic network, valves (white circles), heaters and sensors is shown in Fig. 1.6.
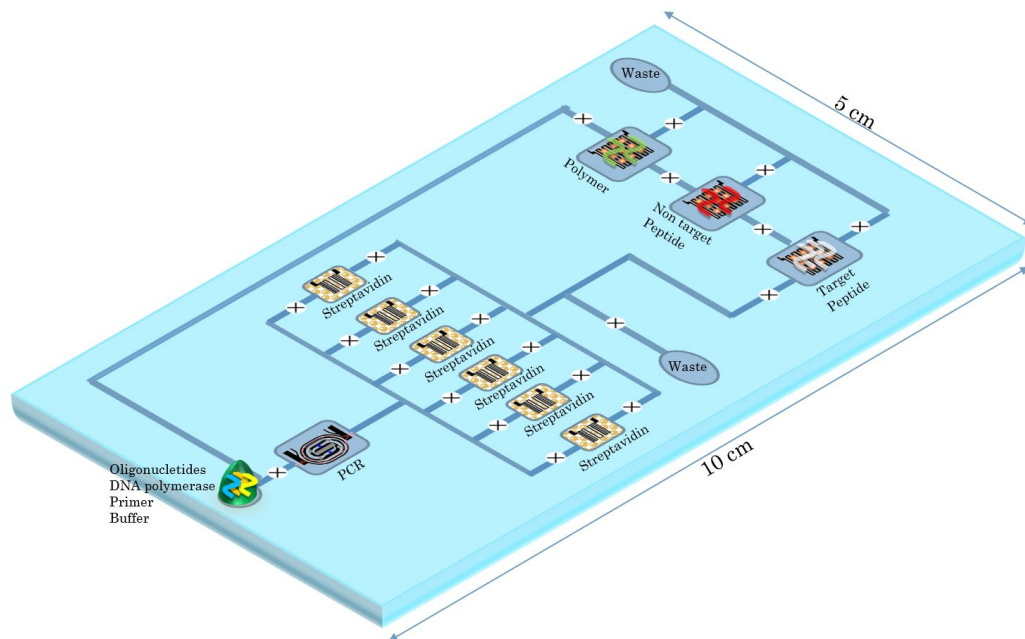
Figure 1.6. Sketch of the SELEX-chip.

1.1 Multifunctional platform: DARWIN'S

Considering the complexity of the SELEX technique, it was decided to implement the different modules independently, taking into account the technological compatibility with the other ones.
To this aim, I have developed a multifunctional platform (System-on-Glass, SoG), named DARWIN'S (DNA Amplification Reactor With Integrated Network (of) Sensors). It hosts:

- *thin metal films* acting as heating sources;

- *hydrogenated amorphous silicon diodes* acting both as temperature sensors to monitor the temperature distribution and photosensors for the on-chip detection;

- a *ground plane* ensuring that the heater operation does not affect the photodiode currents.

Depending on the functional module to be implemented, the DARWIN'S has been optically and thermally coupled with another glass hosting a properly designed microfluidic network made in polydimethylsiloxane (PDMS).

1.1.1   Site for PCR amplification

The structure of the proposed LoC system for the PCR module comprises:

1. a microfluidic network, made in PDMS, that includes a channel for inlet and outlet, a chamber for the PCR and two thermo-actuated valves (the chamber is isolated when they are activated).

2. three thin film heaters. Two of them are located near the inlet and outlet positions of the chamber to actuate the valves and isolate the chamber, while the last one, positioned below the chamber, is dedicated to the PCR thermal cycles.

3. temperature sensors and photosensors (by using amorphous silicon diodes).

A glass substrate hosts the microfluidic network and another glass hosts the sensors on one side and the heaters on the opposite side.

In particular, thermo-actuated microvalves are designed on the device and since their working principle relies on the thermally-actuated deflection of a PDMS membrane to close the channel, the microfluidic network is the combination of two PDMS layers: the control layer, which implements the thermo-actuated valves, and the flow layer, which includes the microfluidic channel and the process chamber. The two PDMS structures are merged using the partial curing method and subsequently the overall microfluidic device is bonded on a glass to couple with the one hosting heaters and sensors. The structure is shown in the Fig. 1.7.

Figure 1.7. General cross section of the device: in pink the PDMS microfluidic network (valves and process chamber) is reported, in blue the glass, in red the heaters and in dark red the sensors. Fluorescent molecules (yellow) can be detected by on chip integrated photosensors.

The solution to be amplified is injected in the microfluidic channel through the inlet. As soon as the channel and the PCR chamber are filled, the two heaters below the valves are actuated. Indeed, applying power to the heaters, the air contained in the valve reservoir heats up and increases its volume creating a pressure that pushes up the PDMS membrane into the channel. As the valves are closed, the PCR cycle can occur by turning on the heater below the PCR chamber. The real time monitoring of the DNA amplification can be performed by the amorphous silicon sensors, which quantify the luminescence produced during the PCR process.

1.1.2 Site for DNA strands separation

In order to obtain a ssDNA pool for the aptamer selection towards the selected target, the amplified dsDNA must be separated. This step is usually performed using streptavidin-coated resin through which the dsDNA, having one of the strands labeled with biotin, is brought into contact (Fig. 1.8). After several washing steps and the elution of the non-biotinylated strand the ssDNA is achieved [60].
This "Separation module" is a glass-PDMS microfluidic chip functionalized with streptavidin, by means of poly(2-hydroxyethyl methacrylate) (PHEMA) polymer brushes, where the dsDNA is separated. Another glass will host a thin film metal heater dedicated to the heating the site at 90-95°C for the separation of the two strands. External microfluidic pumps are necessary for the fluid movement.
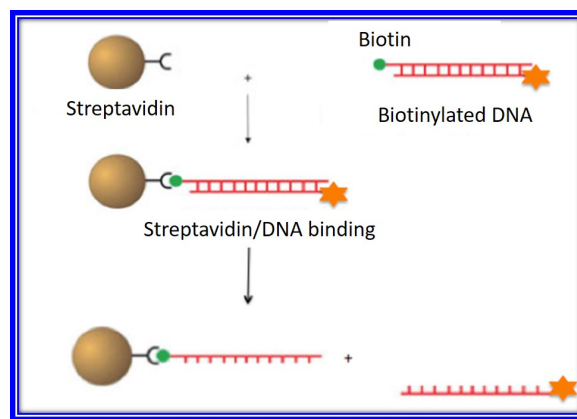
Figure 1.8. Schematic representation of SELEX separation module, using the streptavidin-biotin bond.

1.1.3 Site for aptamers selection

Similar to the other ones, the structure of the proposed system for this "Selection module" will comprise:

1. a microfluidic network, made in PDMS (polydimethylsiloxane), that includes a serpentine chamber for the selection and two thermo-actuated valves (activated to allow the chamber isolation);

2. a functionalized glass with the desired target hosting the PDMS network;

3. a glass hosting a thin film heater dedicated to the heating step;

4. temperature sensors to monitor the temperature.

Chapter 2

DARWIN'S[1]

This chapter presents the integration on a single glass substrate of different thin film technologies in order to develop a multifunctional platform suitable for liquid handling, on-chip thermal treatments and on-chip detection of biomolecules. As mentioned, we refer to the whole structure as *DARWIN'S* (DNA Amplification Reactor With Integrated Network (of) Sensors) or *System-on-Glass* (SoG): its design has been made taking into account the compatibility between the different manufacturing technologies and the characteristics of the glass substrate.

The SoG combines two main modules with specific functions in the sample-treatment process: i) *thin film resistors* acting as heaters to induce temperature variation in a well-defined area of the glass substrate; ii) *thin film sensors* for the temperature control and for the optical detection of molecules. All the devices are electrically connected, through metal contacts positioned on the glass edge, to an electronic system that drives the heaters and reads the sensor output signals. The electronic system, developed by another PhD student, is composed by two different boards, one controls the temperature and the other one reads the optical signals [15].

Stacked layers of thin film metals have been selected as heaters [78], while hydrogenated amorphous silicon (a-Si:H) diode has been chosen as basic structure for the thin film sensors [72]. The low deposition temperature (below 250°C) and the optoelectronic characteristics of the a-Si:H make this material one of the most promising for the fabrication of thin film devices on glass substrate both in large area electronics [9] and in sensor applications [22]; [49]. In particular, recently our research group proposed the use of p-doped/intrinsic/n-doped a-Si:H junction as both photosensors [16]; [15]; [17] and temperature sensors [12].

Different bio-analytical procedures can be implemented by coupling the SoG with a specific microfluidic network. Particularly, we tested the functionality of the system in the three different modules for the SELEX chip: aptamers selection, PCR amplification and DNA strands separation, described in the following chapters.

The SoG operation during the thermal treatment of biomolecules is reported in Fig. 2.1. The Fig. 2.1a shows the top view of the microfluidic network (grey region) including the process chamber (serpentine shape) and the microvalves (green region). The working principle of the microvalves relies on the thermally-actuated deflection

---

[1]This chapter is based on the article *"Multifunctional System-on-Glass for Lab-on-Chip applications."* Petrucci, G., et al., Biosensors and Bioelectronics (2016) [70]
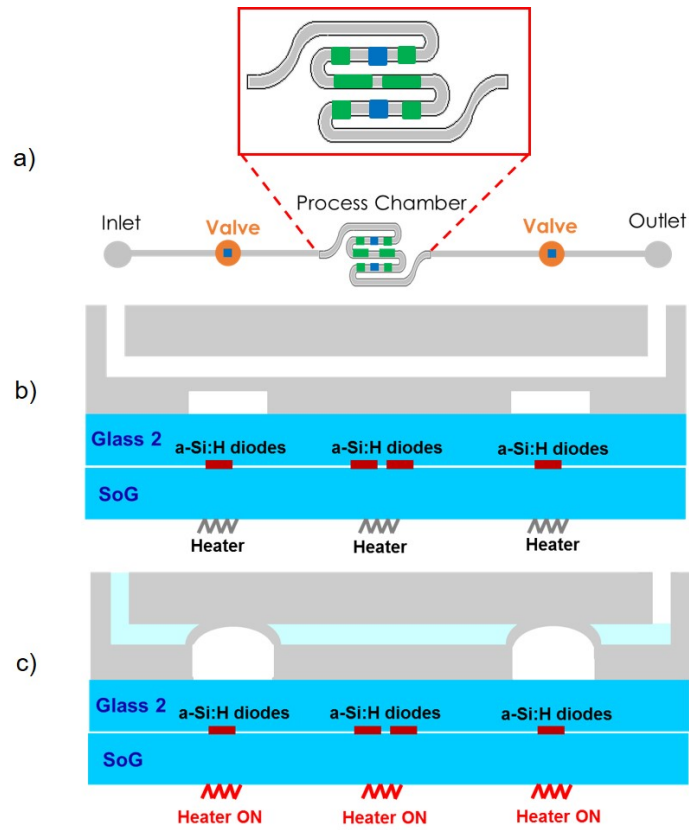
Figure 2.1. Schematic illustration of the operation of the SoG, integrating thin film metal heaters and a-Si:H diodes, coupled with a microfluidic network. Top view of the microfluidic network showing in the zoom the alignment with the a-Si:H diodes. Temperature sensors ($800 \times 800 \mu m^2$) are reported in blue, while the photosensors ($1100 \times 1100 \mu m^2$ and $3150 \times 1100 \mu m^2$) are reported in green (a); cross section of the system with microvalves in OFF (b) and ON (c) conditions.

of a PDMS membrane to close the channels. For this reason, the microfluidic network is the combination of two PDMS layers: the control layer, which implements the thermo-actuated valves, and the flow layer, which includes the microfluidic channel and the process chamber. Fig. 2.1b and Fig. 2.1c represent the cross sections of the SoG optically coupled to the microfluidic chip. Three thin film heaters are present: two of them actuate the valves, while the central one performs the thermal treatment of the analyte in the process chamber. Just to briefly remind, after inserting the liquid from the inlet (see Fig. 2.1b), the two heaters located under the valves are turned ON. The resulting heat increases the temperature inside the air chamber, pushing up the valve membrane and closing the channel (Fig. 2.1c). Subsequently, it is possible to turn ON the heater under the process chamber to provide the thermal energy for the analyte treatment or for the biomolecular analysis.

2.1 Device design

The DARWIN'S development started from the design of the single modules, taking into account the compatibility of the different fabrication technologies and the integration issues deriving from the combination of the electronic devices on a single substrate.

2.1.1 Heater design

The thin film heaters designed for our purposes base their operation on the Joule effect, for which a conductor crossed by an electric current dissipates energy as heat, depending on the intensity of the electric current passing through it. In mathematical terms, it's possible to write the first Joule's law as follows:

$$P = V \cdot I \tag{2.1}$$

where P is the dissipated power, V is the voltage across the circuit, I is the intensity of the current. In case of a resistor, using the Ohm's law, this relationship can be rewritten as:

$$P = \frac{V^2}{R} = I^2 \cdot R \tag{2.2}$$

The choice of the metals, of the film thicknesses and of the geometry determines the overall resistance value according to the relation:

$$R = \rho \cdot \frac{L}{h \cdot s} \tag{2.3}$$

where L is the length of the resistive path, s the width, h the section thickness and ρ the electrical resistivity of the used material.
The current flowing in a resistor dissipates energy in the form of heat which increases with the increase of the value of the current itself. The dispersed energy also depends on the geometry of the resistor as well as on its resistance R. The dependence on the resistivity is usually linearized with the thermal expansion:

$$R = R_0 \cdot [1 + \alpha(T - T_0)] \tag{2.4}$$

where R_0 is the value of the resistance at a given temperature T_0 and α is the coefficient of thermal resistance depending on the type of material. The formula can also be expressed in term of resistivity as given below:

$$\rho = \rho_0 \cdot [1 + \alpha(T - T_0)] \tag{2.5}$$

where ρ_0 is the metal resistivity at the temperature T_0.

The thermal behavior can also be expressed in terms of dissipated power as the sum of two terms given below:

$$\Delta P = H \cdot \frac{d\Delta T}{dt} + G\Delta T \tag{2.6}$$

where ΔP is the change in power dissipated within the system, H is the heat capacity and G is the conductance.

The choice of heating and cooling methods for microfluidic processes is of great importance for achieving high temperature ramping speeds, temperature precision and thermal distribution uniformity inside the chamber [106]. In order to implement a precise thermal control, the vast majority of studies exploits external approaches such as external metal blocks (Peltier elements), which are however bulky and high power consuming [64].

Other technologies embedding a micro heater in the system have been developed to reduce the lab-on-chip dimensions. A serpentine geometry was studied for example by Lao et al. [51]. They developed platinum heaters and sensors on a silicon-based micro machined fluidic chamber, integrating a digital temperature control. Different heaters geometries have been studied by Hsieh et al. [40]; [41] by comparing their temperature response. They studied two blocks of heaters, two blocks with additional side heaters, an array of heaters with additional side heaters and self-compensated array of heaters. Selva et al. [81]; [82] showed also that it is possible to optimize the heater shape in order to generate different temperature profiles by making a finite element study of the thermal response of the heater. By patterning the substrate with an optimized resistor, it is possible to generate a uniform temperature distribution on a selected area with great accuracy and short response time.

In the following sections we discuss the design of thin film metal heaters deposited on a glass substrate, featuring a heater area comparable to the active area of the thermal treatment and low power consumption. In particular, the thin film heater has been designed respecting the followings requirements:

- Area: $0.8\,\mathrm{cm} \times 0.85\,\mathrm{cm}$;

- Metals: Cr, Al, Cr, Ti/W;

- Maximum power supply: $5\,\mathrm{V}$, $500\,\mathrm{mA}$ (provided by a USB port);

- Substrate: glass.

As reported, the power dissipated in a heater due the Joule effect is a well known phenomenon but the prediction of the temperature field in the entire device is difficult to solve with analytical expression. For this reason a numerical software

simulator has been used to design the thin film heater: *COMSOL Multiphysics* software.

The following parts will concern the different studied geometries and the optimized one that we are still using for our purposes.

2.1.1.1 COMSOL Multiphysics

COMSOL Multiphysics is a finite element numerical simulator that couples the electrical and the thermal problems, through the Joule effect, when a potential difference is applied to the resistor. To simulate the device composed by a thin film heater deposited on a glass substrate, we needed to couple the electrostatic problem and the heat transfer problem. The first one was used to calculate the electric field (E) and the current density (J) in the structure when an electric potential (V) is applied to a conductive thin film. The second one was used to calculate the temperature field in the device when a heat flux (Q_{DC}) is applied to the structure. The coupling between the two problems has been ensured by the following equation:

$$Q_{DC} = J \cdot E \tag{2.7}$$

where Q_{DC} is the heat flux and it is the independent variable (input) of the thermal problem, J is the current density and E is the electric field. J and E are the dependent variables (output) of the electrostatic problem which has as input only the voltage applied to the heater. In the parameter of the simulator we considered also the temperature dependence of the resistivity. This can be expressed by equation(2.5), where $T_0 = 0°C$, ρ_0 is the resistivity at 0 °C, α_0 is the thermal coefficient of the material and T is the operating temperature expressed in Celsius degrees. This equation represents a further element that concatenates the modules used in the simulations because the electrostatic model depends on the heat transfer model.

Heaters with different geometries have been integrated in order to obtain the temperature range utilized in the biological process and to make the temperature distribution as uniform as possible within the microfluidic reaction chamber.

2.1.1.2 Previous geometries

[2] The project was developed taking into account the possibility to use the thermo-actuated valves (later described in Sect. 3.3.1) to confine the microfluidic chamber. Two side heaters are then designed to precisely actuate the valves and a larger central one is designed for the microfluidic chamber itself. It's very stringent to have high temperature uniformity for the latter required by the biological sample, while for the valves it is only necessary to reach the closing temperature and avoid a strong influence on the central part.

The selected materials and thicknesses, determining the value of the electrical resistance, are mainly defined by the power requirement, while the central resistor geometry is determined by the specification of uniform spatial temperature distribution over the thermal process area, as mentioned. At the same time, the heaters aligned

---

[2]This work has been reported in Petrucci, G., et al. "Thermal characterization of thin film heater for lab-on-chip application." AISEM Annual Conference, 2015 XVIII. IEEE, 2015 [71]

with the valves have been designed according to the valves dimension with a meander shape covering an area of $2 \times 2 \, \text{mm}^2$.

As mentioned above, thin film heaters are deposited on a glass substrate, featuring a heater area comparable to the active area of the thermal treatment, a temperature uniformity of $\pm 1\,°\text{C}$ suitable for example for the PCR amplification (for our purposes, it is the most crucial step) and a low power consumption. Different heater geometries have been designed using COMSOL Multiphysics and, after the designing process, the device showing the most uniform temperature distribution has been fabricated using thin film technologies. To validate the modeled results, an infrared thermo-camera measured the thermal distribution over the heater in steady state condition [71].

In particular the investigated heater geometries, deposited on a $50 \times 50 \, \text{mm}^2$ glass substrate, are reported together with their dimensions in Fig. 2.2.
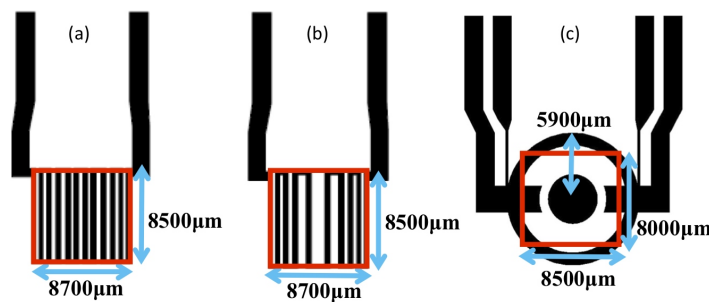
Figure 2.2. Studied geometries: meander (a), chirp (b) and circular (c) with their main dimensions. Red squares represent the active area, i.e. the area required for the thermal treatment.

Each heater includes a central part devoted to the heating (represented by the dense vertical lines in Fig. 2.2a and Fig. 2.2b and by the circular geometry in Fig. 2.2c) and two vertical side lines for the electrode contacts (represented in the figures by the more wide vertical black pads). Fig. 2.2c also presents two additional pads for the 4-wire measurements, to determine precisely the voltage applied across the heater. The central region of each geometry is the effective area of the device, useful to biological protocols, over which the control of the thermal profile is required. This active area is defined in the figure by the red squares. To develop a multiple function lab-on-chip, the dimensions of the active area are designed as close as possible to that of the central part of the heaters.

In order to compare the performances of the different geometries, the temperature distribution has been simulated by setting the electrical power dissipated by each heater to induce a temperature of about $60\,°\text{C}$ (required for example for an isothermal PCR) inside the active area. We plotted the temperature distribution along the *x-* and *y-axis* at three different coordinates for each axis. Results are summarized in Fig. 2.3.

In the first column a sketch of the active area with the cut lines taken at three different coordinates are reported, while the following columns show the temperature trends for the three geometries. In particular, the *meander geometry* has a ΔT_x along each x line of about $5\,°\text{C}$ and a ΔT_y, always along each y line, of about $7\,°\text{C}$. The maximum temperature difference is about $10\,°\text{C}$, showing that this geometry
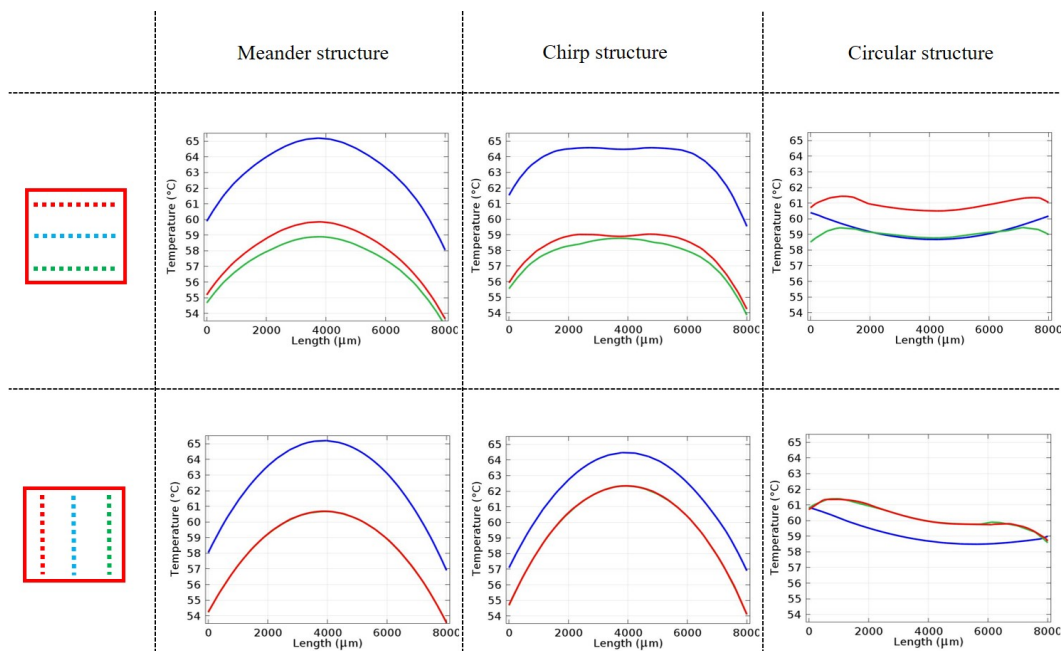
Figure 2.3. Comparison between temperature trends of the three geometries along x- and y-axis. Cut lines have been taken in the active area at three different coordinates: red lines refer to $3500\,\mu$m from the center in upper and left direction for x- and y- axis respectively, blue lines have been taken in the center, while green lines refer to $3500\,\mu$m from the center in lower and right direction for x- and y- axis respectively.

provides a not satisfactory temperature distribution. In particular, the temperature in the central part is higher than at the heater edges.

For this reason, the geometry has been changed increasing the distance between the central arms and decreasing that of the side arms and at the same time increasing and decreasing their respectively width. For this new geometry (called *chirp structure*) the temperature uniformity along x-axis has been improved ($\Delta T_{\mathrm{x}} = 3\,^{\circ}$C). We can observe a plateau in the central part of the active area, along which there is a constant temperature. However, the temperature difference along the y-axis is still quite high ($\Delta T_{\mathrm{y}} = 7.5\,^{\circ}$C). The maximum temperature difference is still of $10\,^{\circ}$C.

The best results have been obtained with the *circular geometry*. The last column of Fig. 2.3 shows that the temperature profiles determined by this geometry along both x and y-axis are quite constant, demonstrating a very uniform temperature distribution. Indeed the maximum temperature difference on the whole active area is $2.5\,^{\circ}$C. In this simulation, the voltage was set to 4,V with a current of $177\,$mA, reaching in the steady-state condition the temperature desired for example PCR application.

In order to further improve the uniformity of the temperature distribution, an innovative geometry not reported in the literature has been studied. It combines the results obtained with the meander geometry studied last year with the elongated shape of the chamber. The circular geometry has been replaced with a double concentric spiral.

2.1.1.3   New heater geometry: concentric spiral

Starting from the results achieved in previous published works [71] and described in the previous Section, the central heater has been designed as a double concentric spiral that geometrically matches the serpentine shape of the process chamber. As
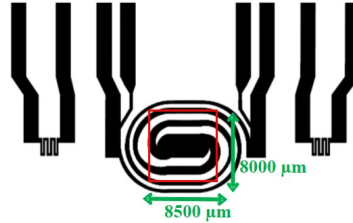
Figure 2.4. Concentric Spiral Heater geometry reporting the dimension of the active area useful for the thermal treatment.

for the other geometries, two side heaters are designed to precisely actuate the valves and a larger central one is designed for the microfluidic chamber itself. The latter width is around $400\,\mu$m in the external sides and $2500\,\mu$m in the central part. With a $100\,$nm/$600\,$nm/$100\,$nm stack of Cr/Al/Cr, it was possible to obtain resistances of $11\,\Omega$ for the chamber heater and of $3\,\Omega$ for the heaters positioned below the valves (we did not utilize in the simulation thicker layers because of practical limitations in the fabrication process). The microfluidic network has been designed ensuring its alignment with the heaters and the a-Si:H diodes. The temperature distribution has been evaluated by setting the electrical power dissipated by the central heater to induce a temperature of about $65\,$°C inside the active area ($\sim 68\,\text{mm}^2$). Simulations applying a voltage equal to $2.57\,$V to the heater show that the chamber temperature is completely comprised in a range of $1.5\,$°C of uniformity along both *x-* and *y-axis* on the glass side hosting the a-Si:H sensors, as reported in the Fig. 2.5 (a) and (b) respectively. The blue, red and green lines on the geometry shape represent the coordinates along which the temperature distribution has been monitored. The maximum temperature difference is of $1.5\,$°C, from $64.5\,$°C to $66\,$°C, for both x- and y-axis. The modeled temperature distribution reaches an average temperature of $65.4\,$°C with a standard deviation of ± 0.75°C underneath the serpentine shaped microfluidic network.
The simulated temperature distribution achieved on the glass side hosting the a-Si:H sensors is shown in Fig. 2.6 where on the left there is the overall glass, on the right the area useful for the thermal treatment.

2.1.2   a-Si:H sensors design

2.1.2.1   Hydrogenated Amorphous Silicon

Hydrogenated amorphous silicon (a-Si:H) has become an established material in semiconductor technology for large area electronics such as photovoltaic and active matrix display application [89]. Studies of amorphous silicon began in the 1960's but the great breakthrough came in 1969 with the growth of amorphous silicon from a silane (SiH_4) plasma [14]. This work was developed during the 1970's with
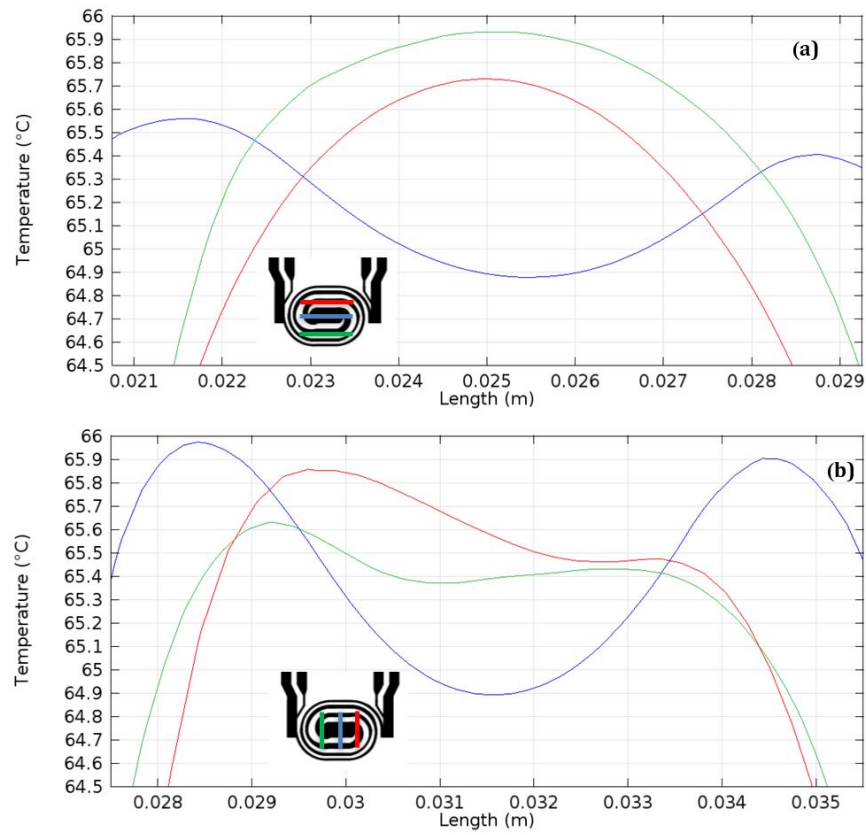
Figure 2.5. Modeled temperature distribution along the *x-axis* (a) and *y-axis* (b) at three different coordinates for each axis in the active area ($\sim 68\,\text{mm}^2$). The reported curves correspond to green, blue and red lines drawn on the heater (see inset).
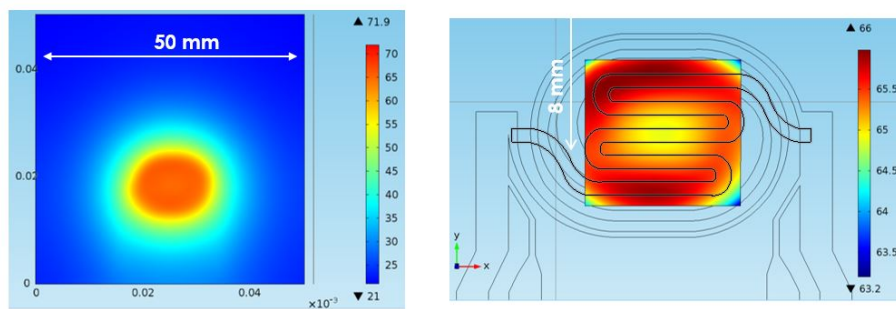
Figure 2.6. Modeled temperature distribution on the overall glass (left) and on the area useful for the thermal treatment (right).

the incorporation of the hydrogen into the material [34] and with the discovery of substitutional doping [86]. The hydrogen binds to dangling bond defects and removes the corresponding electronic states in the band gap, thus eliminating most of the trapping and recombination centers [91]. The addition of phosphine (PH_3) or diborane (B_2H_6) to the plasma during growth creates n-type and p-type doped hydrogenated amorphous silicon [91].

Taking advantages of these improvements the hydrogenated amorphous silicon exhibits all the required semiconducting properties of doping, photoconductivity and junction formation [89].

Usually the a-Si:H is deposited by Chemical Vapor Deposition (CVD) as thin film on a variety of inexpensive, i.e. glass, and flexible, i.e. polymers substrates. Deposition process requires relatively low temperature generally up to 300 °C and is also suitable for depositing alloy materials, such as the silicon nitride which provides the passivation layer needed for electronic devices [90].

Currently, hydrogenated amorphous silicon is used for large area applications such as flat panel displays, which use active matrix of Thin Films Transistors (TFT), and solar cells, which uses arrays of photodiodes [89].

2.1.2.2 a-Si:H sensors

Amorphous silicon sensors may easily be deposited through PECVD (Plasma Enhanced Chemical Vapor Deposition) at temperatures below 300 °C, being therefore compatible with substrates of different materials with different shapes and geometries. The crystalline silicon, on the other hand, cannot be grown on a substrate but it can only be deposited as a wafer, obtained by slicing a monocrystalline silicon bar. For this reason, the amorphous silicon is used in the production of the detection devices such as photosensors and temperature sensors.

The a-Si:H n-i-p sensors consists of a very thin n-doped and p-doped layers with a thicker undoped i-intrinsic layer in between. Unlike crystalline silicon, a n-p junction is ineffective as rectifying diode without the undoped layer because of the high defect density in doped a-Si:H [89]. Furthermore in a n-i-p junction, the doped layers provide only the rectifying behavior and do not contribute to the light sensitivity because the lifetime of the generated minority carrier is so small that most of them recombine before they can be collected at the contacts [91].

Diode as radiation sensor
The basic electrical characteristics of a n-i-p photodiode are those typical of a diode exponentially increasing forward bias current and a low reverse bias current. The large increase in reverse current due to the illumination is the basis for its use as light sensor.

The absorption of light in the sensor generates electron-hole pairs in the i-layer. The charges are separated under the action of the electric field and cause a current flowing in the external circuit. The electric field is resulting from the combination of internal built-in potential and applied reverse bias. The photocurrent I_{PH} can be expressed as the product of the electron charge, q, and the generation rate of photoelectrons Φ_e:

$$I_{PH} = q \cdot \Phi_e \tag{2.8}$$

Ideally a photodetector converts each incident photon into a photoelectron that contributes to the photocurrent. This may occur when the photon energy is greater than the bandgap energy of the photodetector material. However, owing to the reflection of the photodetector surface, surface recombination and the spatial dependence of the photon adsorption in the photodetector, not all incident photons produce a photoelectron. The ratio of the photoelectron generation rate Φ_e to the incident photon rate Φ_{PH} is called Quantum Effinciency, QE: it comprises a wavelength-dependent absorption that generates electron-hole pairs and a bias-dependent charge collection efficiency. The photocurrent I_{PH} can be expressed as:

$$I_{PH} = q \cdot \Phi_e = q \cdot QE(V, \lambda) \cdot \Phi_{PH} \tag{2.9}$$

Diode as temperature sensor

A common silicon diode may be used as temperature sensor considering its threshold voltage in forward bias that varies with the temperature. More precisely, the threshold voltage decreases with increasing of temperature with an almost perfectly linear trend.

The ideal behaviour of a diode is described by the Shockley ideal diode equation, often referred as diode law mathematically represented by:

$$I_D = I_0 \left(e^{\frac{V_D}{nV_T}} - 1 \right) \tag{2.10}$$

where I_D is the diode current, I_0 is the reverse bias saturation current, V_D is the voltage across the diode, V_T is the thermal voltage, T is the absolute temperature and n is the ideality factor, also known as the quality factor. The reverse saturation current I_0 is also temperature dependent and can be expressed as:

$$I_0 \cong KT^r e^{(-qV_g/kT)} \tag{2.11}$$

where V_g is the extrapolated energy gap at absolute zero temperature. Here, the terms K, r and V_g are independent of temperature T. The constant K depends on the geometric factors like width of p–n junction in diode, while r is a process dependent parameter and has a value ~ 3.5 for silicon.

For $I >> I_0$, Eq. 2.10 can be rewritten as:

$$I_D = I_0 e^{(qV/kT)} \tag{2.12}$$

In order to get a relation in terms of forward voltage V, Eqs. 2.11 and 2.12 can be combined to obtain the following expression:

$$V = V_g + \frac{kT}{q}(ln\, I_D - ln\, k - r \cdot ln\, T) \tag{2.13}$$

The above relation shows that at constant current, the forward voltage drop is almost a linear function of temperature, with negative slope. The generic V-T trend of a diode is shown in Fig. 2.7. For most practical purposes, this relation can be expressed as:

$$T = A + BV \tag{2.14}$$
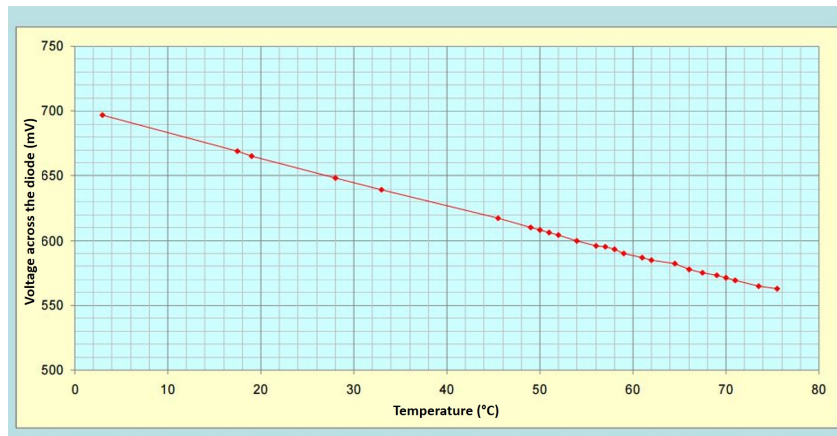
Figure 2.7. Characteristic diode V-T curve.

This forms the basis of the constant current method for sensing temperatures with the help of diodes. Constants A and B are determined experimentally by driving the diode at constant current and calibrating it for the target temperature range [57]. It is then possible to measure the temperature by measuring the voltage variation across the diode. The trick is to make it work with a constant current, I_D: because if the current in the diode varies, the threshold voltage also varies accordingly to its value, making impossible to measure the temperature. The current value is usually chosen small enough to avoid heating the diode.

2.1.2.3   The designed a-Si:H diodes

The sensors are metal/n-type/intrinsic/p-type metal stacked structures deposited on a glass substrate. A detailed scheme of the structure is reported in Fig.2.8.
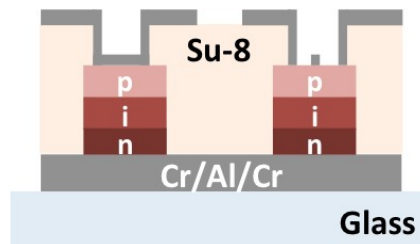
Figure 2.8. Structure of the a-Si:H temperature sensors (left) and photosensor (right). The only difference between the two devices is the geometry of the top contact: continuous metal for the temperature sensor and metal grid for the photosensor.

This device can be used both as temperature and radiation sensors [23], both reported in Fig. 2.8. Again: as temperature sensor the device is biased with a forward constant current and the voltage drop measured across the diode results linearly dependent on temperature [11]; as light sensor, the device is biased in short circuit condition or at small reverse voltage and its photocurrent is proportional to the intensity of the light absorbed in the active intrinsic region. Considering the optical coupling between the two glasses shown in Fig. 2.1b and the sensors position

shown in Fig. 2.9 and considering that the light to be detected is generated inside the microfluidic process chamber, the top electrode of the photosensor has to be transparent to light. This can be achieved by using a transparent conductive oxide (TCO) [21] or a metal grid (see the device on the right in Fig. 2.8). On the other hand the temperature sensor has to be blind to light and therefore the top contact is a stack of metal layers (see the device on the left in Fig. 2.8). The design of the spectral response of the device can be obtained through an optimization of the thicknesses and energy gaps of the a-Si:H layers [10]; [11] with the aim to maximize the signal-to-noise ratio. The active region is the intrinsic layer while the doped films sustain the built-in voltage without contributing to the photocurrent. The optimization process has been carried out by using a numerical device simulator, which couples the continuity and Poisson equations in the a-Si:H stacked structure, taking into account a Gaussian distribution of dangling bonds and exponential band tails in the energy gap. We found that an i-layer thickness of 400nm minimizes the dark current.

As shown in Fig.2.9, there are two temperature sensors under the valves to monitor their closure temperature and two temperature sensors in the center of the process chamber for a punctual monitoring of the temperature distribution within the heated area (blue squares). The photosensors (grey squares), which could be used for real time quantification of biomolecules measuring the light emitted during the thermal treatment are located in the middle of the process chamber to maximize the collected signal.
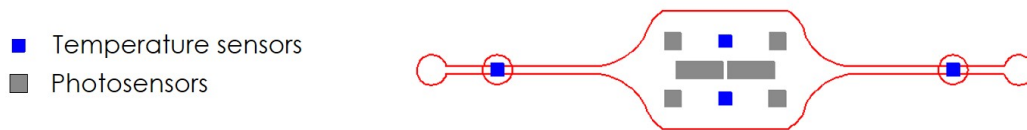
Figure 2.9. Sensor position inside the microfluidic chamber: the temperature sensors, reported in blue, are $800 \times 800\,\mu\text{m}^2$, while the photosensors, reported in grey, are $1100 \times 1100\,\mu\text{m}^2$ and $3150 \times 1100\,\mu\text{m}^2$.

The diodes position was designed according to the microfluidic design, while their electrical contacts have been patterned following the specifications of the card edge connector used for biasing and read out of the sensors. The exact dimensions of the diodes are also reported in Fig. 2.9 but they are here reported again for the sake of completeness: temperature sensors, reported in blue, are $800 \times 800\,\mu\text{m}^2$, while the photosensors, reported in grey, are $1100 \times 1100\,\mu\text{m}^2$ and $3150 \times 1100\,\mu\text{m}^2$.

The fabrication of the chip had seen the design of four photolithographic masks using a dedicated graphic software: AutoCad. Their design had to take account the contact system used to interface the chip on glass with the system: the necessity to have thermal cycles varying the voltage in fact requires to interface the LoC with a unit that can automatically control the process via software. We chose to use a standard PCI connector, the commonly found in every motherboard for personal computers. The heater and sensors contacts have been designed in order to adjust the structure in this connector pin system. In this way once realized the device on the glass, the alignment is automatic. Indeed it's sufficient to accommodate

the substrate adjacent the edge of the connector itself without need to operate a microscopic alignments.

Therefore the masks are been designed taking into account that, once the chip is fabricated, it must be plugged into a 20-pin PCI connector. Its specifications have been extrapolated from the datasheet. The significant values are:

- the pitch, intended as distance between the centers (or equivalently between homologous edges) of two adjacent pins, equal to 2.54 mm;

- the distance between the edge of the connector and the center of the first pin, equal to 2.36 mm.

As specified in the datasheet, a PCI connector can house thicknesses up to 1.57 ± 0.18 mm; the slides used in this work have a thickness of 1.2 mm. The connector is also a "dual beam" type connector and making possible to contact both faces of the substrate and allowing to realize the heater on one face and the sensors on the opposite face.

The four designed masks are respectively for the metal bottom contact, the mesa of the sensors, the insulation layer and the metal top contact and they are reported in Fig. 2.10.
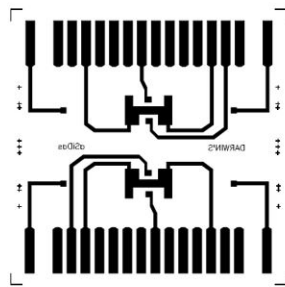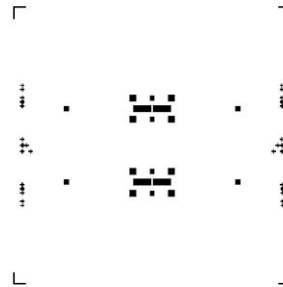
Bottom layer (mask#1)   Sensors structures (mask#2)
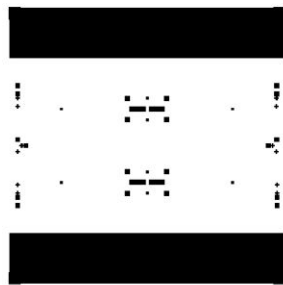
Passivation layer (mask#3)   Top layer (mask#4)
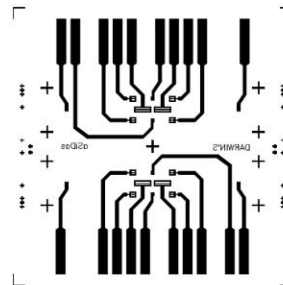
Figure 2.10. Sensors masks designed with AUTOCAD software.

The contacts placed in the bottom and top part are 1.6mm wide, after which the

track is narrowed to about 1mm up to contact with the sensor. To create an alignment base for subsequent layers, a marker set was also designed at the edges of the structure. These markers have the classic form of a symmetrical cross, as it's possible to see from the Fig. 2.11 together with their dimensions.
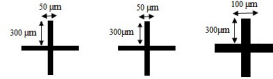
Figure 2.11. Alignment markers.

The aligned masks on the AuotCAD interface are shown in Fig. 2.12. The device is duplicated because of the possibility to have more opportunity for the device testing, since the complete heaters-sensors fabrication on one glass substrate is quite difficult. In blue the bottom contact of the sensors is reported, in white the mesa, in orange the SU-8 via holes and in green the top metal contact.
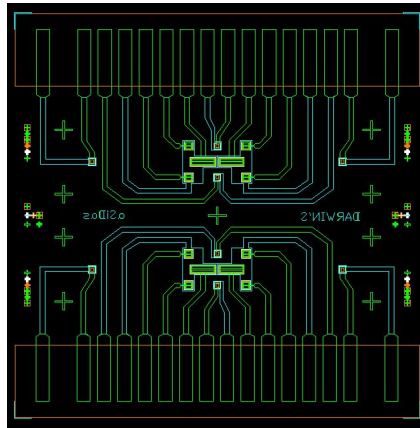
Figure 2.12. DARWIN'S AUTOCAD interface showing all the layers for the sensors fabrication.

2.2 Device fabrication and characterization

Heaters and sensors have been fabricated using thin film technologies. In particular for both heaters and sensors, we have initially fabricated the electronic devices on a separated glass substrate to optimize the deposition parameters of the all technological steps. Only at the end we have integrated heaters and sensors on a single glass substrate.

2.2.1 Thin Film Technologies

The fabrication of the DARWIN'S structures involved processing facilities available at the Department of Electronic Engineering. The fabrication requires a combination of three main processes: deposition, photolithography and etching.

2.2.1.1   Deposition

Thin films are deposited onto the substrate as individual atoms from a vapor phase. Several deposition methods can be used depending on the materials to deposit, the desired thickness and electronic properties as well as film morphology. Two classes of the deposition techniques can be identified: Chemical Vapor Deposition (CVD) and Physical Vapor Deposition (PVD).

In the CVD the source material is provided as a gas or liquid with sufficient vapor pressure that enables transport at moderate temperature. The activation and the transport can be assisted by a plasma (Plasma Enhanced CVD, PECVD) or heat (Hot Wire CVD, HWCVD), at low pressure (Low Pressure CVD, LPCVD) or atmospheric pressure (Atmospheric Pressure VCD, APCVD).

In the PVD the source material is provided as solid which is vaporized and transported to the substrate by heat or by an energetic beam of electrons, photons or positive ions such as in the sputtering and evaporation.

In this work PECVD, sputtering and evaporation techniques were used to deposit the thin films needed in the DARWIN'S fabrication.

PECVD

Plasma Enhanced Chemical Vapor Deposition (PECVD) can be used to deposit silicon based films such as intrinsic or doped hydrogenated amorphous silicon (a-Si:H) and silicon nitride (SiN_x).

In PECVD process gas chemical precursors are injected in a high vacuum chamber at a specific flux rate. A Radio Frequency (RF) plasma is ignited and the gases are decomposed into active ions. The use of plasma enables the deposition at low temperature (below $450\,°C$), which is necessary for the retention of hydrogen in the growth of a good quality a-Si:H films [89]. The main parameters affecting the deposition and the properties of PECVD films are the flow and composition of the gases, the pressure inside the chamber, the power of the Radio Frequency, the temperature of the substrate and the geometry of the reactor [84].

Sputtering

Sputtering is a physical vapor deposition (PVD) process whereby atoms are ejected from a solid target material due to bombardment of the target by energetic ions. A plasma of inert gas, such as argon, is created within the deposition chamber by a RF field. The positive ions are accelerated towards a cooled source target material which is eroded by the arriving ions via energy transfer and is ejected in the form of neutral atoms. These sputtered particles can ballistically fly from the target in straight lines and impact energetically on the substrates, such as glass, which will be coated by a thin film of the source material [84]. For efficient momentum transfer, the atomic weight of the sputtering gas should be close to the atomic weight of the target, so for sputtering light elements neon is preferable, while for heavy elements krypton or xenon are used. For general purposes, gases with mean atomic weight, such as argon, should be used. Reactive gases can also be used to sputter compounds. The compound can be formed on the target surface, in-flight or on the substrate depending on the process parameters. The main parameters to control the

properties of the sputtered material are the pressure of the plasma, the flow rate, the substrate temperature, the bias voltage and the power [38].

In this work Titanium/Tungsten (TiW) alloy, Aluminum (Al) and Indium Tin Oxide (ITO) have been sputtered.

Evaporation

Physical Vapor Deposition (PVD) is a process by which a thin film of material is deposited on a substrate according to the following sequence of steps: 1) the material to be deposited is converted into vapor by physical means; 2) the vapor is transported across a region of low pressure from its source to the substrate; and 3) the vapor undergoes condensation on the substrate to form the thin film.

In PVD by evaporation, the conversion into vapor phase is achieved by applying heat to the source material, causing it to undergo evaporation. This is done in a high-vacuum environment, so that the vaporized atoms or molecules will be transported to the substrate with minimal collision interference from other gas atoms or molecules.

There are several ways by which heating is achieved in PVD by evaporation. The simplest (and one that has many disadvantages) is to employ resistive heating, wherein a wire (or boat) of low vapor pressure metal such as tungsten is used to support strips of the material to be evaporated. The wire is then resistively heated, so that the metal to be deposited melts first and evaporates.

In electron beam evaporation, a high kinetic energy beam of electrons is directed at the material for evaporation. Upon impact, the high kinetic energy is converted into thermal energy, heating up and evaporating the target material.

Evaporation can also be achieved by heating the source material with RF energy. This technique employs an RF induction heating coil that surrounds a crucible containing the source. This method of evaporation is known as inductive heating evaporation.

The advantages offered by evaporation for PVD are: 1) high film deposition rates; 2) less substrate surface damage from impinging atoms as the film is being formed, unlike sputtering that induces more damage because it involves high-energy particles; 3) excellent purity of the film because of the high vacuum condition used by evaporation. During the DARWIN'S fabrication, the evaporation of Chromium (Cr) and Aluminum (Al) has been involved.

2.2.1.2 Photolithography

The photolithography is the definition of microstructures onto thin films. This technique involves the use of three sequential main steps. The first is the coating of the substrate with a photo-sensitive polymer or photoresist (PR). The second step is the exposure of the PR with a defined mask. The last is the development of the exposed PR with a removal.

Photoresists are composed by a polymer, a sensitizer and a casting solver. Upon irradiation with a specific wavelengths light, the polymer changes its structure, either rendering a soluble or insoluble material. When the PR polymer chains become weaker with irradiation the PR is said to be positive. In the other case, it is said

negative.

One PR used in the DARWIN'S fabrication is **AZ1518**, a positive PR from MicroChemicals. The coating of the substrate is performed spinning the PR at 500 rpm for 10 s and at 3000 rpm for 30 s in order to obtain the desired thickness of about 2 μm. The evaporation of the solvent is achieved by a soft-baking step on hot plate at 100 °C for 1 minute. The sample is exposed with a UV radiation impinging upon a mask. The mask is the glass substrate with printed metal pattern which blocks the radiation in the metal areas. In this way the pattern defined in the mask is copied on PR.

The exposed photoresist is hard baked on the hot plate at 115 °C for 2 minutes in order to stop the uncompleted PR reactions. The development of the PR is performed dippig the sample in a solution of appropriate developer (AZ100 developer). Finally the substrate is washed with water and dried with nitrogen. With the described procedure areas protected with PR have been created.

Another PR used in the DARWIN'S fabrication is the **SU-8** (3000 series), a negative PR from MicroChem. To obtain maximum process reliability, substrates should be cleaned and dried prior. The first step is the dehydration for 5 minutes at 200 °C. Then the coating of the substrate is performed spinning the PR at 500 rpm for 10 s and at 3000 rpm for 30 s in order to obtain the desired thickness (5 μm for example). The evaporation of the solvent is achieved by a two step soft-baking on hot plate at 65 °C for 1 minute and 95 °C for 2 minutes. The sample is exposed with a UV radiation impinging upon a mask. The mask is a glass substrate with printed metal pattern which blocks the radiation in the metal areas. In this way the pattern defined in the mask is copied on PR.

The exposed photoresist is post exposure baked on the hot plate at 65 °C for 1 minute and at 95 °C for 2 minutes. The development of the PR is performed dippig the sample in a solution of appropriate developer (SU-8 developer). Then the substrate is washed with water and dried with nitrogen. Finally it's baked for 30 minutes at 200 °C in order to stop the uncompleted PR reactions. With the described procedures areas free from PR have been created, since this kind of PR is mainly used for via holes definition in the insulation layer or for the passivation step.

2.2.1.3 Etching

The pattern defined by lithography is transferred to the underneath film by etching of the areas not protected by photoresist. Two different methods can be used: *dry etching* and *wet etching*.

Dry Eching

The Dry etching is performed in the gas or vapor phase, physically by ion bombardment and/or chemically by reactions through reactive species at the surface. There are several dry etching systems that vary in their selectivity, etch mechanism, for example physical or chemical, and profile, for example anisotropic or isotropic [38]. The selectivity towards different materials is achieved by using different composition of gas mixture. These gases can be fluorinated, chlorinated compounds in combination with oxygen and argon. [38].

In the DARWIN'S fabrication the Reactive Ion Etching (R.I.E.) has been used. RIE combines both physical and chemical etching processes and shows a good selectivity and anisotropy. RIE was used to etch the amorphous silicon and the ITO. The physical etching of the RIE is provided by Argon bombardment. The ions damage the unreactive substrate. The chemical etching is provided by the chlorinated and fluorinated species such as CF_4 and SF_6. The fluorine atoms react with the silicon surface and form a volatile product, SiF_4, that is removed from the substrate [38].

Wet Eching

The wet etching processes uses liquid-phase etchants. The sample is immersed in a bath of etchant, which must be shaken to achieve good process control. Since the wet etching involves a chemical reaction, different specific etchants can be used to selectively etch the layers. Wet etchants are usually isotropic, which leads to large bias when etching thick films.
In the SoG fabrication wet etching has been used to remove metal layers such as Chromium, Aluminum, ITO and Titanium/Tungsten alloy with the following etchants:

a) Chromium (etching rate of about 5 Å/s)

- 30 g $Ce(NH_4)_2(NO_3)_6$ (ammonium and cerium nitrate)
- 9 ml CH_3COOH (glacial acetic acid)
- 200 ml deionized water

b) Aluminum (etching rate of about 10 Å/s)

- 80 ml H_3PO_4 (85% phosphoric acid)
- 5 ml HNO_3 (nitric acid)
- 10 ml deionized water

c) ITO (etching rate of about 50 Å/min)

- HCl (cloridric acid) and deionized water in proportion 2:3 at 100 °C

d) Titanium/Tungsten (etching rate of about 25 Å/s)

- NH_3 (ammonia) and H_2O_2 (hydrogen peroxide) in proportion 1:3

The etching rate have been obtained empirically but they have a very high uncertainty and in any case they vary from etching to etching depending on the saturation of the solutions and therefore on how these have already been used. However it is good practice to operate visual inspection of the sample, rinsing and drying it every 2-3 minutes.

2.2.2 Heaters fabrication and characterization

The fabrication of the double concentric spiral heater as well as of the previous geometries has been implemented using the lift-off technique, to prevent that chemical etching solution could damage other structures on the glass, with the following detailed processes:

- spin coating of photoresist AZ1518;

- mask#5 interposition and exposure (see Fig. 2.13a);

- development of photoresist in AZ100 remover;

- thermal vacuum evaporation of a three metal stack Cr/Al/Cr (500Å/6000Å/ 1000Å) in a Balzers 510 evaporation system. The bottom chromium layer features a very good adhesion on glass but its thickness should be kept to a minimum in order to avoid thermomechanical mismatch. Therefore a thicker aluminum layer is deposited to provide a reliable and low-resistance metallization. The upper chromium layer is to prevent the aluminum oxidation in direct contact with air or, in view of the integration of amorphous silicon sensors on the top of this metal sandwich, it would act as a diffusion barrier between the aluminum and this amorphous silicon layer;

- lift-off of the PR with acetone.

The fabricated heaters are reported in Fig. 2.13b. We see two identical structures, mirrored with respect to the green dashed lines.

Figure 2.13. (a) Heater mask (mask #5); (b) Fabricated heaters

To validate the results obtained through simulations (see Sec. 2.1.1.3), the three heaters, have been experimentally deposited by vacuum evaporation with the same thicknesses utilized in the simulations and patterned by photolithographic process to achieve their alignment with the valves and the process chamber. We found a 5% variation between the resistance values of the simulations and the ones measured in the fabricated device. The heater performances in steady state condition have been characterized by measuring the temperature distribution on the glass side hosting the a-Si:H sensors using an infrared thermo-camera (FLIR A325). A very good agreement between simulations and experimental results has been achieved. Indeed, applying a voltage equal to 2.9 V to the metal pads, the spatial temperature distribution reaches an average temperature of 64.9 °C (quite good for an isothermal PCR) with a standard deviation of ±1 °C (Fig. 2.14. See for comparison Figs. 2.5 and 2.6 and text at pag. 16).
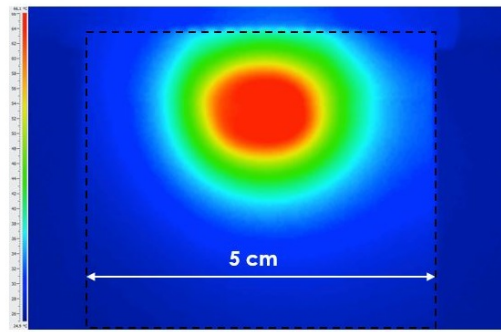
Figure 2.14. Experimental temperature distribution achieved on the $5 \times 5 \, \text{cm}^2$ glass substrate using a FLIR A325 thermo-camera.

2.2.3 a-Si:H sensors fabrication and characterization

The sensors are metal/n-type/intrinsic/p-type stacked structures deposited on a glass substrate by PECVD. The deposition time of the intrinsic layer has been set taking into account the simulation results and the film growth rate. The p-type layer is a silicon carbide layer because of the carbon presence due to the methane in the deposition mixture. This leads to an increase of the energy gap and therefore to a lower light absorption. Its thickness is a trade-off between the need to sustain the electric field inside the intrinsic layer and to minimize the light absorption. It is worth noting that during the PECVD process the deposition temperature of the a-Si:H layer decreases, avoiding the boron out-diffusion that instead can occur in p-i-n structure.

A detailed drawing of the structure is reported in Fig. 2.8. The a-Si:H sensors fabrication has been performed with the following technological steps:

1. deposition of a stack Cr/Al/Cr layer ($300 \, \text{Å}/1500 \, \text{Å}/300 \, \text{Å}$) acting as bottom electrode and its patterning by photolithography with mask #1 (Fig. 2.10);

2. deposition of the n-i-p a-Si:H layers by PECVD in a three-chamber ultra-high vacuum system with the deposition parameters reported in Table 2.1:

Table 2.1. PECVD parameters used in the deposition of a-SiC:H layers. The gases are SiH_4 pure silane, PH_3 silane deluted (5%), B_2H_6 helium deluted (5%), CH_4 pure methane; P_D is the process pressure; P_{RF} is the radio-frequency power density; T_D is the substrate temperature.

Layer Type	Material	SiH_4 ($sccm$)	PH_3 ($sccm$)	B_2H_6 ($sccm$)	CH_4 ($sccm$)	P_D ($Torr$)	P_{RF} (mW/cm^2)	T_D ($°C$)	Deposition Time
n	a-Si:H	40	10	-	-	0.3	25	200	3'
i	a-Si:H	40	-	-	-	0.68	25	180	40' (35')
p	a-SiC:H	40	-	3	60	0.7	25	160	50"
δn	a-Si:H	40	10	-	-	0.3	25	200	3"

3. deposition of a Cr film ($500 \, \text{Å}$) in a Balzers 510 evaporation system;

4. photolithographic patterning of the sensor structure through mask #2 (Fig. 2.10) and the following steps:

    a. wet etching of the Cr layer. This step leads to the formation of a CrSi film that enhances the collection of the photogenerated carriers;

    b. reactive ion etching of the a-Si:H layers. The dry etching parameters are reported in Table 2.2.

Table 2.2. a-Si:H etching parameters.

Power set	100 W
Forward power	100 W
Reflected power	0 W
BIAS	250 V
Initial Pressure	33 mTorr
Process Pressure	120 mTorr
O_2 flux	10 sccm
CF_4 flux	100 sccm
C load	705
C tune	689
Time	20'

5. deposition of an insulation layer (SU8-3005) and its patterning for the via hole definition through mask #3 (Fig. 2.10);

6. deposition by magnetron sputtering of a TiW film (2000 Å) and its patterning for electrical connection definition through mask #4 (Fig. 2.10);

7. deposition of a passivation layer (SU8-3005) to protect the a-Si:H diodes leaving uncovered the electrical connection.

The masks utilized for the sensor fabrication are all reported in Fig. 2.10 and the fabricated device is shown on Fig. 2.15.
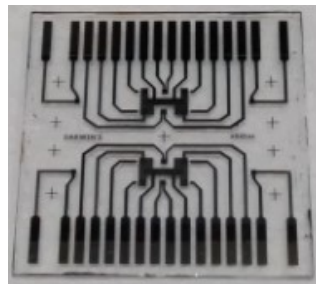
Figure 2.15. Fabricated chip hosting only the temperature sensors and the photosensors.

As for the heaters, we have initially fabricated the a-Si:H diodes on a separated glass substrate to optimize the deposition parameters of the all technological steps.

After these steps, the a-Si:H sensors were characterized measuring their current-voltage curves in dark and light condition and photosensors quantum efficiency response. The current-voltage characteristics have been measured by using a Source Measure Unit Keithley 236, that applies a voltage to the diode and reads the corresponding current. As an example current density in dark and light condition for a photosensor of $800 \times 800\,\mu\text{m}^2$ is reported in Fig. 2.16.
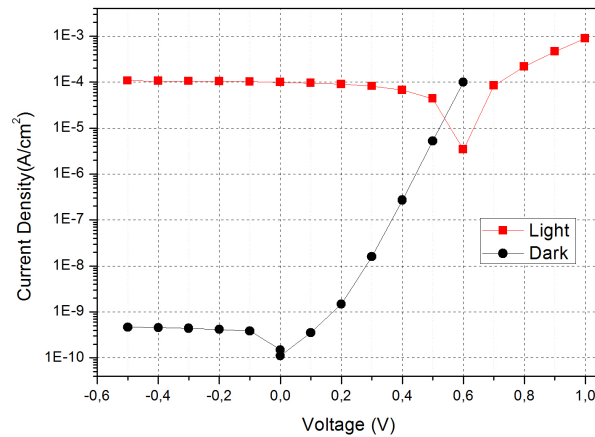
Figure 2.16. a-Si:H photosensor current density measured in dark and light conditions.

The measurement has been done by using the Keithley in both dark and light condition turning on the microscope light provided by the probe station. The photons impinging on the sensors in light condition produces a current increase of 5 order of magnitude with respect to the dark condition, demonstrating a high photosensors sensitivity to the light.

In order to quantify the response to light, the quantum efficiency curves have been measured in a double-arm optical set-up, which includes an halogen lamp as radiation source, a Jobin-Yvon Spex monochromator, a beam splitter, a calibrated silicon diode as reference and optics for focusing the light coming out from the monochromator. Results of the measurements are reported in Fig. 2.17, which shows the quantum efficiency values averaged over three photodiodes measured in short circuit conditions. Taking into account that the responsivity, R, is related to the quantum efficiency, QE, through the relation:

$$R(\lambda) = \frac{\lambda(\mu m)}{1.238} \cdot QE(\lambda) \tag{2.15}$$

it's possible to derive that R is above $100\,\text{mA/W}$ in the 400-650 nm range, which includes mostly of the fluorophore emission spectra utilized in biochemical applications. Even though crystalline silicon photodiodes present at this wavelength range a higher responsivity, a very high signal-to-noise ratio can be achieved in a-Si:H devices thanks to the very low dark current. On the other hand, taking into account that the
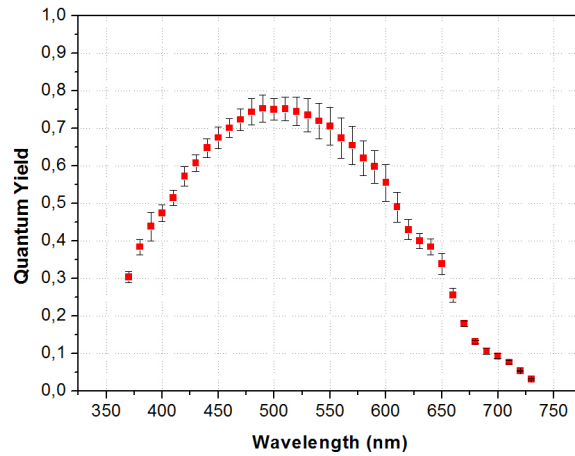
Figure 2.17. Quantum efficiency curve of the a-Si:H photosensors. Symbols refer to the values averaged, error bars represent the standard deviations.

measurement bandwidth is $0.6\,\mathrm{Hz}$, we derive that the dark current noise at small reverse voltage is below $50\,\mathrm{fA/cm^2}$.

We have also found that the dark current density at room temperature is usually around $10^{-10}\,\mathrm{A/cm^2}$ at reverse bias voltage below $250\,\mathrm{mV}$, independently of the diode area. This reverse current increases exponentially with temperature as reported in Fig. 2.18, where we observe an increase of about two orders of magnitude going from room temperature ($25\,^\circ\mathrm{C}$) to $80\,^\circ\mathrm{C}$, when the diode is biased at $-200\,\mathrm{mV}$. The
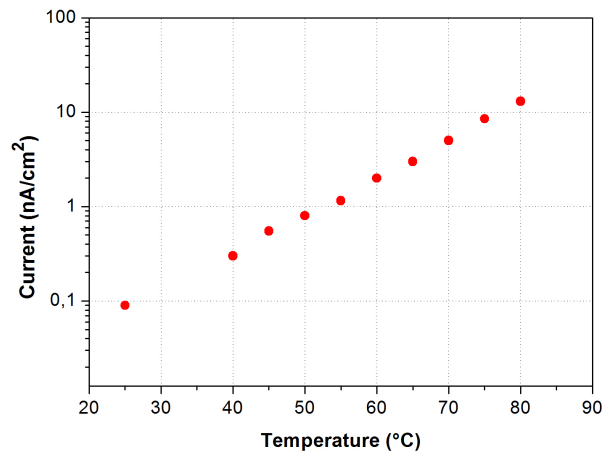
Figure 2.18. Current measured in dark conditions at different temperatures, when the a-Si:H photosensor is biased at $-200\,\mathrm{mV}$

temperature sensors were characterized using a thermocamera FLIR A325 and a custom made electronics. The a-Si:H diode is biased at a constant current and the voltage drop across is proportional to its temperature. The electronic circuit controls

the diode temperature through a Proportional-Integral-Derivative (PID) algorithm developed by another PhD student. Briefly, the PID control is implemented through the following steps:

1. biasing the diode at constant current in forward condition;

2. driving the heater with an initial voltage;

3. measuring the voltage across the diodes in order to infer the diode temperature through the calibration curve;

4. comparing the actual temperature with the set-point temperature;

5. control of the heater driving voltage;

6. cycling through steps 3-5 until the temperature set point has been reached.

The diode has been preliminarily calibrated combining the reported electronic system and an infrared thermo-camera (FLIR A325). In particular, we have monitored the temperature of the diode under test through the FLIR while the electronic board kept constant the temperature of the diode (i.e. its voltage drop) actuating the PID control. Results of this calibration procedure, when the diode is biased at 200 nA, are reported in Fig. 2.19. Taking into account this calibration curve, we see that the curve slope, which represents the diode thermal sensitivity, is around $3.2\,\mathrm{mV/^\circ C}$, which is higher than the thermal sensitivity of crystalline diodes. We have found that, for each temperature, the standard deviation of the voltage measured across the diode is very low $(\pm 0.1\,\mathrm{mV})$.
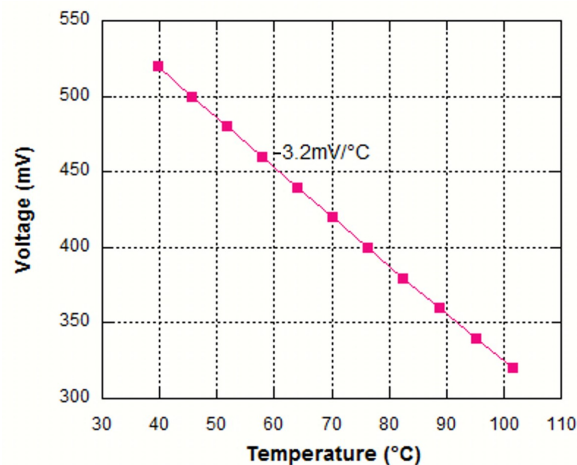
Figure 2.19. Thermal characterization of the temperature sensors obtained recording the voltage and temperature on the diode biased at 200 nA with the electronic system and the infrared thermo-camera. The standard deviation of the voltage measured across the diode is $\pm 0.1\,\mathrm{mV}$ and therefore is not visible in the figure.

2.2.4 DARWIN'S integration

The integration of the heaters and the a-Si:H diodes on the same glass substrate have to take into account the compatibility of the different technological steps. In particular, the implementation of photolithography and etching on each glass sides considered the following steps:

a. selection of a limited pool of suitable materials;

b. definition of the time sequence of the technological steps (for example which side has to be processed first);

c. selection of the coating layers to avoid damage to the previously fabricated structures;

d. compliance with the requirements on the temperature deposition of the materials and on the etching techniques to be utilized.

It is also necessary to avoid crosstalk effects so that the operation of one module does not interfere with the correct behavior of the other functional modules.
The characterization of the first DARWIN'S device highlighted a crosstalk between the heaters and the a-Si:H sensors. In particular, we found that the biasing of the heaters affects the current of the thin film sensors, because the leakage current resulting from the voltage applied to the heaters interferes with the current flowing through the sensors biased in short circuit condition (Fig.2.20a).
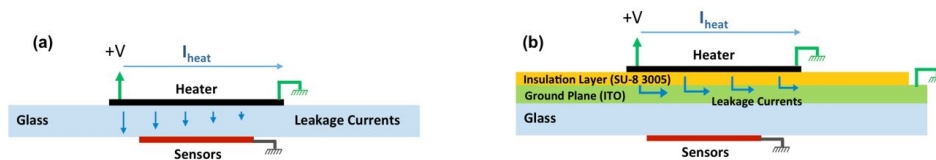
Figure 2.20. SoG scheme without (a) and with (b) the ground plane in ITO (green) and the insulation layer in SU-8 (yellow).

This leakage current hides the photocurrent and therefore it has to be eliminated. A ground plane has been then inserted between the thin film heaters and the glass to ensure an electrical path to ground of this current. In this way the leakage current flows to ground not interfering on the correct operation of the photodiode, as also shown in the equivalent electric circuit reported in Fig.2.21. Therefore, a layer of conductive material has been realized and covered with an insulation plane of SU-8 3005 before the heater fabrication (Fig.2.20b). The ground plane has been fabricated with a transparent material, Indium Thin Oxide (ITO) to ensure a good alignment between the heaters and the sensor.
Furthermore we have found a more reliable process if the diodes are fabricated before the heaters. This is mainly related to the high number of photolithographic steps required for the sensor fabrication with respect to the heater. Indeed if the heater is fabricated as first step, we observed that even though it is covered with a protective layer, it experiments physical damages during the sensor fabrication probably due

(a) Without ground plane   (b) With ground plane
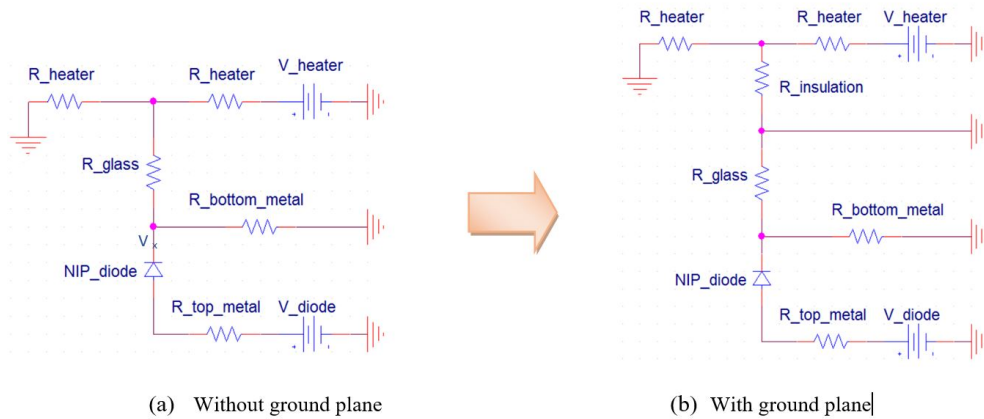
Figure 2.21. Electric equivalent circuit without (a) and with (b) the ground plane.

to the mismatch between the thermal expansion coefficients of the Cr/Al/Cr stack and the SU-8 layer.

Taking into account all the above considerations, the whole System-on-Glass has been fabricated through the following technological steps:

1. cleaning of the glass substrate;

2. deposition of an ITO film (2000Å) acting as ground plane on one glass side;

3. deposition on the same side of TiW layer (2000Å) acting as a protecting layer of the ground plane during the sensor fabrication;

4. a-Si:H diodes fabrication on the other glass side with the technological steps described in detail in Sec. 2.2.3;

5. removal by wet etching of the TiW layer deposited in step 3;

6. deposition of a SU-8 3005 acting as insulation layer between the ground plane and the heaters;

7. thin film heaters fabrication on the SU-8 layer (see details in par. 2.2.3);

8. SU-8 3005 final passivation of the heaters to protect the structure.

In order to verify the reproducibility of the chosen technological steps, several identical systems have been fabricated on $5 \times 5 \, \text{cm}^2$ glass substrates. The two glass sides of one fabricated SoG are shown in Fig. 2.22. Each glass side contains two identical structures, mirrored with respect to the green dashed line. The red dashed ellipse defines the central heater of the lower part in corrispondence of the microfuidic reaction chamber. At the end of the fabrication process, the performances of both heaters and a-Si:H sensors have been tested. From experimental measurements performed through the thermo-camera, we observed that the temperature distribution due to the heater is not affected by the presence of the metal lines of sensor electrodes and therefore it is the same of that measured in absence of the a-Si:H sensors.
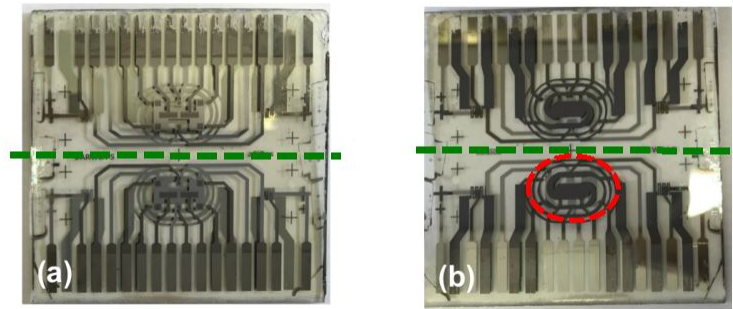
Figure 2.22. Fabricated device: sensor view (a) and heater view (b). Each glass side contains two identical structures, mirrored with respect to the green dashed line. The red dashed ellipse defines the central heater of the lower part.

Furthermore, the sequence of technological steps from 5 to 8 (see list above) does not change significantly the dark current, the thermal sensitivity and the responsivity of the a-Si:H sensors.

In conclusion, in this work for the first time a multifunctional platform integrated on a single glass substrate was developed: it includes different thin film technologies to perform on-chip thermal treatments and on-chip detection of biomolecules.

Chapter 3

Microfluidics

3.1 Theoretical Microfluidics

As widely explained in the Introduction, microfluidic systems can manipulate small amounts of fluids (from 10^{-8} to 10^{-18} liters), using channels with dimensions ranging from few micrometers to hundreds of micrometers. Ultimately fully automated and miniaturized devices can be obtained by integrating microfluidics with detection system. A microfluidic device has a series of essential and generic components: system to introduce reagents and samples, methods for moving fluids and strategy for detection and quantification of signals from the samples. A typical microfluidic system consists of a channel network connected to external actuators as a syringe pumps, peristaltic or air pressure pumps. Device simplicity, portability and integrability can be improved using the phenomenon of capillarity that allows fluids to fill spontaneously the microchannel.

In micro-scale, as in macro-scale, the fluid dynamics can be mathematically described by the *Navier Stokes equation*. The difference is that in macro-scale the inertial force is dominant while in the micro-scale surface forces and viscous forces are dominant. As it will be exemplified hereafter, the decrease of the dimensions to the micron scale results in particular phenomena related to the considerable increase of the surface-to-volume ratio when compared to the dimension of bulk device [52]. Navier-Stokes equations are non linear partial differential equations obtained from the conservation law of mass (3.1) and momentum (3.2):

$$\frac{\partial \rho}{\partial t} + \nabla \cdot (\rho \vec{v}) = 0 \tag{3.1}$$

$$\frac{\partial (\vec{v})}{\partial t} + \vec{v} \cdot \nabla (\vec{v}) = -\nabla p + \eta \nabla^2 \vec{v} + \vec{F} \tag{3.2}$$

where ρ is the density of the fluid, η the viscosity, $\vec{v}$ velocity vector of the flow, p is the static pressure, $\vec{F}$ is the external body force. For fluids of constant density, the eq. 3.1 becomes: $\nabla \vec{v} = 0$.
Another important parameter is the dimensionless Reynolds number, Re, it is defined as:

$$Re = \frac{\rho \nu l}{\mu} \tag{3.3}$$

where ρ is the density of the fluid, μ is the dynamic viscosity of the fluid, ν is the velocity and L is a characteristic linear dimension (as travelled length of the fluid). This number defines the ratio between inertial and viscous forces and it is an indicator of fluid regime, which can be either turbulent ($Re > 2000$) or laminar ($Re < 2000$). Microfluidics are characterized by having almost exclusively laminar flows regimes due to reduced Reynolds numbers (usually lower than 0.1).

When a constant pressure p is applied in a straight channel we obtain a constant flow rate Q. This can be expressed in the Hagen-Poiseuille law:

$$\Delta p = R_F Q \tag{3.4}$$

where R_F is a factor known as the flow resistance. This law is completely analogous to Ohm's law $\Delta V = R \cdot I$ relating the electrical current I through a wire with the electrical resistance R and electrical potential ΔV along the wire. This law is very important to set the flow rate in the microchannel changing the pressure applied and the flow resistance of the system.

In most of LoC systems, microchannels having a rectangular cross-section are employed, even if for example to implement pneumatic and/or thermo-actuated valves, it is necessary to have a round cross-section of the channel, as we can see in Fig. 3.1.
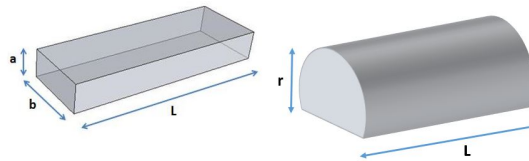
Figure 3.1. Rectangular channel: a-depht, b-width and L-length;. Round channel: L-length and r ray

For the rectangular shape one can find the R_F through a Fourier sum representing of the Navier-Stokes:

$$Q \approx \frac{a^3 b \Delta p}{\eta 12 L} \cdot \left(1 - 0.63\frac{a}{b}\right) \tag{3.5}$$

So:

$$R_F = \eta \left[\frac{1}{12}\left(1 + \frac{5a}{5b}\right)\frac{abR_H^2}{L}\right]^{-1} \tag{3.6}$$

Satisfying the condition $a < b$, where a is the height, b the width and L the length of the channel, R_H, known as hydraulic radius of the microchannel, is equal to:

$$R_H = \frac{2Area}{wettedPerimeter} = \frac{ab}{a + b} \tag{3.7}$$

This number expresses the ratio between the area section of the duct and half of its wetted perimeter. Hydraulic radius is used to determine if the flow is laminar or turbulent, since the velocity in the Reynolds equation is based on the cross section

area of duct.

Changing the flow resistance it's possible to set different flow rates.

Particle diffusion is another important parameter that influences the design of a microfluidic device. The diffusion refers to the redistribution of molecules or particles in response to concentration gradients. Different microfluidic applications were developed to precisely control particle diffusion and concentration gradients both spatially and temporally.

As the Fick's first law shows, the flux of molecules J is related to the concentration C through the diffusion coefficient D (also known as diffusivity):

$$J = -D\nabla C \tag{3.8}$$

In microfluidic the convenient unit for D is $\mu m^2/s$. The smaller particles redistribute themselves more rapidly by diffusion than larger ones. In microfluidics, diffusive flow becomes much important when comparing with macroscale fluidics.

The dimensionless Péclet number (Pe) expresses the ratio between convection and diffusion:

$$Pe = \frac{vL}{D} \tag{3.9}$$

where L is a characteristic length, v the velocity of the fluid and D the diffusion coefficient.

Another one of the most important functions in a microdevice is the handling of fluids. There are active pumping systems as syringe pumps, electro-osmotic pumping, electrowetting, and passive pumping strategies that can use chemical gradients, osmotic pressure or capillary forces.

In microfluidic device, the surface effects are dominant due to the large surface to bulk ratio. One of such effetcts in 50-100 μm wide microchannels is the capillarity effect. The capillarity can be used to handling fluids in microchannel without the use of external power. The flow rate can be fixed through equations, changing the shape, the size or the wettability of the channel, or a combination of these parameters [105]. A clear disadvantages is that the flow rate is fixed for a given set of conditions, being impossible to make interactive flow rate changes.

In this work, active pumping system were used to guide the different fluids across the microfluidic device for the SELEX applications.

3.2   Microfluidic Fabrication

Typical components of microfluidic devices can be divided in negative and positive features. Examples of negative features are: wells, orifices, and channel themselves, because they are defined by regions of vacant space; while membranes, beams and pillars are examples of positive features because they are defined by regions of solid matter (Fig. 3.2). Original microfluidic devices were fabricated using the same techniques as microelectromechanical systems (MEMS), using photolithography and etching in a cleanroom [52].

The materials used for microfluidic devices microfabrication include polymers, silicon and glass. In early developments the microfluidics paths were made using silicon and glass. Currently in research, a majority of microfluidic flow paths are made in
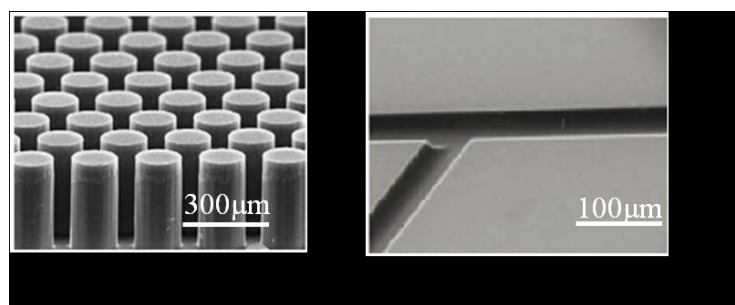
Figure 3.2. SEM micrographs a) Example of positive feature pillars, b) example of negative feature: channel

polydimethylsiloxane (PDMS). Before the growth of interest in polymer materials for fabrication of microdevices, silicon had the greatest attention because silicon-based MEMS technology and their fabrication process were already a well-established technology. However the use of silicon has disadvantages: it is opaque to ultraviolet and visible light, it is impermeable to gases (this can be a problem when working with cells) and cleanroom fabrication is expensive and time consuming. It is more practical to make flow paths, valves and pumps in a compliant polymer, in fact today, usually the microfluidic channel are etched in silicon and sealed with a PDMS sheet in conformal contact. In this work the device is made in PDMS as will be explained later in detail.
PDMS is the most widely used polymer material for microfluidic fabrication [1]. It is inexpensive, nontoxic, biocompatible, optically transparent and permeable to the gas and also it is chemically stable under a wide range of environments. Generally two of the most used commercial PDMS products in microfluidic are Sylgard 184 from Dow Corning (the one used in this work) and the RTV 615 from Momentive Performance Materials. Another important advantage of the PDMS is the easy fabrication by a diverse set of replication methods using SU-8 molds by means of soft-lithography techniques. The SU-8 thick negative photoresist is sensitive to UV light and is widely used in microchannel mold fabrication. As previously explained, in positive photoresist the areas exposed to light become susceptible to chemical attack and are usually removed using its appropriate developer, while in negative photoresist the exposed areas result in a stable structure and therefore the remaining ones are dissolved by appropriate developer.

The specific biological application of our system can be implemented by coupling the SoG with an appropriated microfluidic network fabricated on another glass substrate. The basic structure of the microfluidic network includes a process chamber and micro valves. Their geometrical features have to be designed according to the requirements of the analyte to be investigated and to the type of analysis to be performed. In particular, the volume of the process chamber has been set to a minimum value of $3.5\,\mu$l. So our system is suitable for amplification of DNA coming not only from a specific cell (and in this case the volume could be much smaller) but also from biological fluids, which may contain pathogens such as virus or bacteria. Indeed, in this case the probability to find the target molecule determines a minimum

amount of blood fluid to be taken and analyzed.

The thermoactuated valves and the microchannel have been designed according to previous works ([96]; [102]). In particular, the channel width and height in correspondence of the valves have been set to $500\,\mu$m and $50\mu m$ respectively, while the valve diameter has been fixed to $2\,$mm. These dimensions guarantee the complete closure when the valve temperature reaches about 90°C. The distance of 6mm between the valve and the chamber also ensures that the heat diffusion from the valve does not affect the temperature distribution inside the chamber. Indeed, by using COMSOL Multiphysics, we have found that, with the valve closed, the effect of heat diffusion becomes negligible at about 5mm from the valve. The chosen geometry for the process chamber is a serpentine shape. It has been designed and fabricated to reduce the bubble formation during the chamber filling.

The microfluidic network has been fabricated in PDMS. As explained, the common procedure for making PDMS channels involves the fabrication of a photoresist mold on a silicon wafer. In particular two different molds, one for the valve and one for the channel and micro chamber, have been designed and fabricated by using soft lithography techniques. In this work, the mold for the microchannel and the process chamber has been realized using the photoresist AZ 40 XT that determines a height around $40\,\mu$m with a round cross-section. Indeed, this photoresist, under reflow condition, becomes soft and changes its shape, giving rise to a rounded channel.

The manufacturing processes of our microfluidic system are the following:

1. Fabrication of the mold for the channel

2. Fabrication of the mold for the valve

3. Fabrication of the PDMS channel

4. Fabrication of the PDMS valves

5. Bonding of the PDMS channel with the PDMS valve

6. Bonding of PDMS system on a cleaned glass

All the technological details of the single process steps for both SoG and microfluidics fabrication are reported in the following subparagraphs.

3.2.1 Materials and method

The PDMS utilized in this work is the Sylgard 184 from Dow Corning (USA). It is a two-components elastomer constituted by a base and a curing agent. By combining the two ingredients in specific ratios and curing them at specified conditions, PDMS of different properties can be obtained. Its typical fabrication process needs the fabrication of a mold usually over silicon substrates, the mixing of the mixture of the PDMS linear polymer and of the crosslinker, its pouring over the mold and the curing at a specified temperature for the complete polymerization. Subsequently, the microfluidic device is peeled from the mold and bonded onto the glass substrate using the transfer bonding technique with uncured PDMS as adhesive. In particular, since in this work the combination of two PDMS layers (flow layer and control layer)

is necessary, we need to bond first these two layers and subsequently the PDMS stack on the cleaned glass. Detailed procedures are reported below:

- **Fabrication of the mold for the channel**
  The positive photoresist AZ40XT was spun on a silicon wafer at 1500rpm for 20s to achieve a thickness of $50 \mu m$. The photoresist was soft-baked at $127 \, °C$ for 7 min and then was exposed under $800 \, mJ/cm^2$ UV light. The exposed photoresist was baked (Post Exposure Bake) at $105 \, °C$ for 1 min 40 s. The sample was put into the developer solution (726 MIF, Microchem) at room temperature for 4 min. Finally, the mold was heated at $130 \, °C$ for 5 min for the reflow process to achieve a round shaped cross-section channel mold.

- **Fabrication of the mold for the valve**
  The negative photoresist SU-8 3050 (Microchem) was spun on a glass substrate at 500 rpm for 5 s (acceleration 100 rpm/s) and at 3000 rpm for 30 s (acceleration 300 rpm/s). The photoresist was soft-baked at $65 \, °C$ for 2 min and at $95 \, °C$ for 6 min on a hot plate and then exposed under a $250 \, mJ/cm^2$ UV light. The photoresist was post-baked at $65 \, °C$ for 2 min and at $95 \, °C$ for 6 min. The sample was put into the developer solution (SU-8 developer, Microchem) and baked on a hot plate at $150 \, °C$ for 30 min to enhance the mechanical properties of the cross-linked photoresist.

- **Fabrication of the PDMS channel**
  The PDMS Sylgard 184 (Dow Corning) was prepared mixing the silicone and the curing agent in the ratio 10:1 and placing the mixture in gentle vacuum at 600 mbar to remove the air bubbles. The PDMS was poured directly onto the channel mold in order to obtain a thick layer of PDMS of about 3 mm thickness. The PDMS was partially cured in oven at $60 \, °C$ for 45 min. The inlet and outlet connections were made by inserting stainless steel pins (0.013" ID × 0.025" OD × 0.5" long) purchased by New Ingland Small Tube Corporation (Litchfield, NH, USA) in the inlet/outlet hole previously formed. Reaction mixture and buffer solutions were flowed in/out of the microfluidic channels by connecting tygon tubing (0.02" ID × 0.060" OD) purchased by Generalcontrol S.p.A. (Milan, Italy) to the pins inserted in the device from one side and a 2.5 ml plastic syringe to the other side of the tube, by inserting the needle in the tubing hole.

- **Fabrication of the PDMS valve**
  The PDMS Sylgard 184 (Dow Corning) was prepared mixing the silicone and the curing agent in the ratio 20:1 and placing the mixture in gentle vacuum at 600 mbar to remove the air bubbles. The PDMS was spun on the previously prepared SU-8 3050 valve mold at 500 rpm for 5 s (acceleration 100 rpm/s) and at 800 rpm for 30 s (acceleration of 300 rpm/s) in order to obtain a $100 \, \mu m$ PDMS thin film. The PDMS was partially cured in oven at $85 \, °C$ for 8 min.

- **Bonding of the PDMS channel with the PDMS valve**
  The partially cured PDMS channel was peeled from the mold and put onto the partially cured valve layer taking care of the alignment between the channel and the valve. Finally, the whole structure was put in the oven at $60 \, °C$ for

2 h 30 min, putting some needles in the inlet and outlet to allow the air to flow away.

- **Bonding of PDMS system on a cleaned glass** The fabrication of the system has been completed joining together the PDMS microfluidic system and a cleaned glass. The microfluidic device has been peeled from the PDMS valve mold and bonded to a glass substrate. Bonding has been achieved spinning a thin layer of PDMS acting as a glue (15 s at 500 rpm and acc. 100 rpm/s, 30 s at 3000 rpm and acc. 500 rpm/s, 4 min at 6000 rpm and 1200 rpm/s). The PDMS system has been peeled from the PDMS valve mold and put on this thin layer for few seconds. Then it has been peeled again and put on the cleaned glass. Finally, the whole structure was put in the oven at 70 °C for 1 h 30 min.

3.3 Microfluidic design

3.3.1 Microfluidic Valves

One of the essential and most interesting aspects of using microfluidics is the ability to actively and dynamically control fluid flow. This can be achieved by using valves that can open and close channels, thus allowing or impeding fluid flow. Many types of valves are available [69] including magnetic, electric, thermal, pneumatic, osmotic and even based on Braille displays. In the following sections thermally actuated valves and pneumatic valves integrated in the system are described.

3.3.1.1 Thermo-actuated Valves[1]

The microfluidic part regarding the thermo-actuated valves has been first investigated on a single glass subtrate independently of the complete device structure, taking into account the PDMS layer thickness, the valves diameter and their position to avoid the influence on the central heater.
The structure includes a microfluidic channel, a thermally actuated valve and a thin film heater. The microfluidic channel with the integrated microvalve is placed on the upper side of the glass substrate, while the thin film metal heater, aligned with the valve, is fabricated on the opposite glass side (see Fig. 3.3). It is important to note that the geometry below the valve is the simple one because the requirements on the uniformity of the temperature distribution are not critical. The valve is "normally open". Indeed, when no voltage is applied to the heater, the pressure inside the air chamber (microvalve) equals the atmospheric value, the valve membrane is in its rest position and the microfluidic channel is open (Fig. 3.3a). When a voltage is applied to the heater, the temperature inside the air chamber increases and the generated pressure pushes up the valve membrane, which closes the channel (Fig. 3.3b).
The valve has a cylindrical geometry with height and diameter equal to $50 \mu m$ and $2 mm$ respectively. The diameter value permits to align by naked eye the microfluidic channel to the valve. The height of the microfluidic channel is $50 \mu m$ as well.

---

[1]This paragraph is based on the article *"Design and fabrication of microfluidics system integrated with temperature actuated microvalve"* Zahra, A., et al., Sensors and Actuators A: Physical (2015)[102]
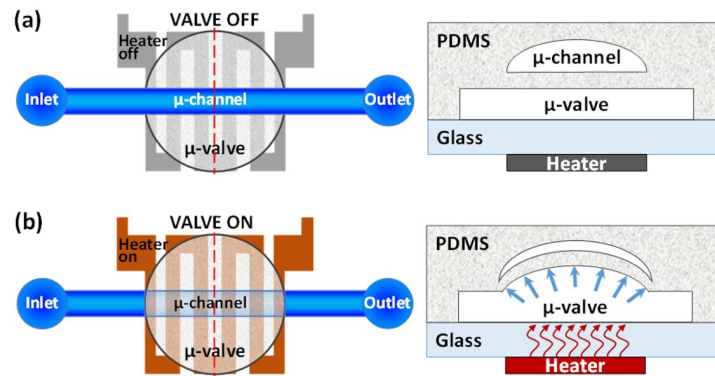
Figure 3.3. Top (left) and cross-section (right) view of the device. (a) Without bias voltage applied to the heater the valve is off and the channel is open. (b) A bias voltage applied to the heater turns the valve on and closes the channel.

The height of the membrane deformation as a function of the valve temperature at different channel widths is reported in Fig.3.4.
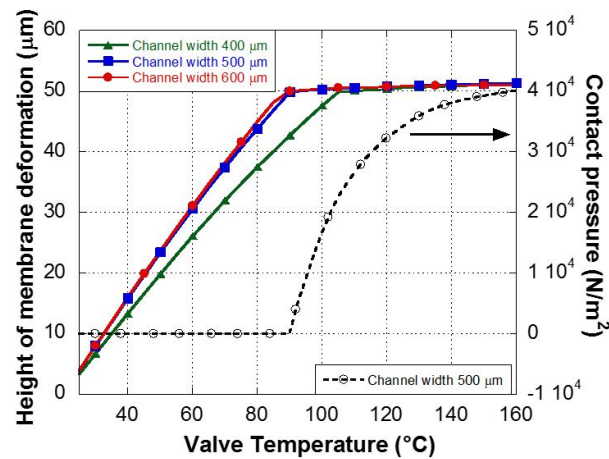
Figure 3.4. Height of the membrane deformation as a function of the valve temperature at different channel widths.

The figure shows that, with $50\,\mu m$ fixed height of the channel, the temperature required for the closure increases with decreasing the channel width. In particular, channel widths larger than $500\,\mu m$ require a closure temperature around $90\,°C$, while to close a $400\,\mu m$-channel width a temperature greater than $150\,°C$ is required. Taking into account these results, we have chosen $500\,\mu m$ as the optimized channel width, since this value ensures the lowest temperature to close the channel (and therefore a reduced power consumption) and a more compact system.

The optimum distance of valves from reaction chamber has been investigated using COMSOL Multiphysics. The parametric simulation of temperature of valves along arc length on $5 \times 5\,cm^2$ glass substrate has been performed, when the valves are at around $90\,°C$, near the closing temperature of channel. The distance of valve along

channel from reaction chamber should be at least 6 mm from both sides of chamber, near the inlet and outlet of channel. Indeed at this distance the temperature is around 38 °C, low enough to do not affect the biological procedure occurring in the process chamber.

As the temperature increases above the minimum temperature value that brings the membrane in contact with the top of the channel, the force of closure of the valve increases. This is shown in the dashed curve of Fig.3.4 that reports the modeled contact pressure between the valve and the top part of a microfluidic channel (right axis) as a function of valve actuation temperature. In this simulation the channel width has been set to 500 µm keeping the channel height equal to 50 µm. At first the contact pressure is zero but near 90 °C it increases sharply, demonstrating that this temperature brings into contact the membrane and the top of the microchannel.

However considering a rectangular microfluidic channel, the membrane closes the microchannel in the central part, but leaves the corners open with a percentage of the closed channel section equal to 62%. At higher temperature, the increase of the closure force reduces the leakage, but however the percentage of the closed channel area keeps below 80% even at 160 °C. In order to develop round-shaped channels, Quake and coworkers [96] baked at 200 °C for 30 min a Shipley SJR 5740 photoresist, which under reflow condition, becomes soft and changes its shape, while P. M. Fordyce et al [33] used the *AZ*50*XT* photoresist. We chose to use this photoresist requiring short soft bake times, no delay for rehydration, very small exposure doses due to its chemical amplification, and showing a high development rate.

The actuation of the valve is done by a thin film heater, which has been designed according to the valve dimension (diameter of 2 mm) with the photolithographic mask shown in Fig. 3.5.
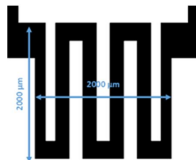
Figure 3.5. Geometry of the thin film heater used for the valve. The measured value of its resistance is 30 Ω.

The heater is a stack of Cr/Al/Cr (300 Å/1500 Å/300 Å) metal layers. Heater fabrication has been performed with the technological steps described in Sec. 2.2.2. The fabrication of the system has been completed joining together the PDMS microfluidic system and the thin film heater. The microfluidic device has been peeled from the glass substrate and bonded to the glass substrate hosting the thin film heater. Finally, channel inlet and outlet holes were made by using a puncher.

The correct operation of the thermally actuated microvalve has been verified by performing several experiments on closure and opening of the microchannel. A blue liquid has been injected with a syringe in the microchannel and the valve condition has been monitored with a microscope. The voltage applied to the heater was set to 4 V. The experimental results showed the correct operation of the valve after several ON/OFF cycles. In order to obtain the opening and closure times of the valve, we extracted for each frame of a video, taken with the microscope, the intensity of

the red component (R) in the valve region of the RGB image. Fig. 3.6 reports the
data normalized to the closure condition, which corresponds to 1, as open circle.
The dashed curves are obtained fitting the experimental data with an exponential
growth for the closing step and an exponential decay for the opening step. In the
figure are also reported three pictures of the frames used to obtain the graph. The
time constants extracted from the fitting curves are *10.6 s* and *1.4 s* for closing and
opening step, respectively. The corresponding switching times calculated as the time
interval between 10% and 90% of the closing ratio dynamic are about 20 s and 5 s,
respectively. It is important to note that the time constant of the closing step is
mainly related to the thermal power supplied by the heater, while the valve behavior
in the opening step is determined only by the system time constant. These times
are suitable for some lab-on-chip applications, as the PCR technique to which this
valve can be devoted.
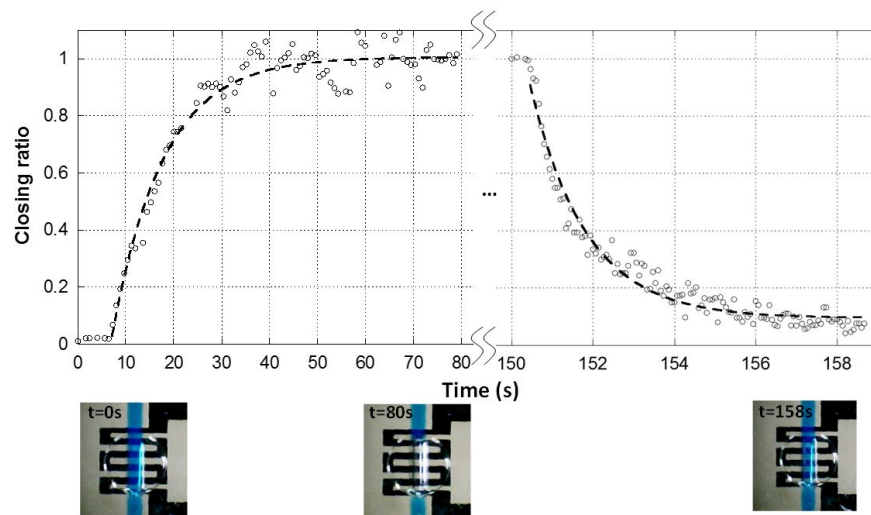
Figure 3.6. Characterization of the valve condition during closing and opening steps (upper
part). Symbols refer to the measured red component of the RGB image taken with a
microscope, while dashed lines refer to exponential fittings. Data are normalized to the
maximum red intensity. The lower part of the figure reports three frames of the video at
t=0 (valve open), t=80 s (valve closed) and t=158 s (valve open)

3.3.1.2   Pneumatic valves

Pneumatic microvalves, introduced by Stephen Quake's group in 2000, generally
utilize the deflection of a PDMS membrane to interrupt flow and has become one of
the most common valve architectures. The reason for their popularity is undoubtedly
that they can be easily integrated [92] with standard soft lithography processes
with which most laboratories are familiar. The control channel that actuates the
membrane is most frequently actuated via an external gas pressure source, but it
can also be filled with a fluid to avoid air permeating into the microchannel through
the membrane. Changes in the pneumatic pressure cause the valve membrane to
deflect and seal against the seat. Normally-open membrane microvalves are designed
to impede fluid flow only when the valve is activated. Upon application of positive

pressure to a control line, a flexible membrane is deflected in order to stop flow through the valve [5].

A very simple yet very effective type of pneumatic valve was also designed by Unger and colleagues [96] and it relied on the mechanical properties of PDMS. In this setup, two channels – a fluid and pneumatic channel – are stacked and cross at 90°, separated by a PDMS membrane some tens of μm thick. The valve is activated by inserting compressed air into the pneumatic channel, which will deform the PDMS membrane and make it bulge into the fluid channel, blocking flow.

The structure of these valves is based on a multi-layer fabrication as for the thermo-actuated valves. The working principle is almost the same, as shown in Fig.3.7. The membrane deformation in the penumatic valve is caused by the liquid pressure (Fig.3.7b) instead by air expansion (Fig.3.7a) in the thermo-actuated system. The microfluidic channel with the integrated microvalve is placed on the upper side of the glass substrate where the amorphous silicon sensors are fabricated. The valve is "normally open". Indeed, when no pressure is applied to the pneumatic channel, the pressure inside the microvalve equals the atmospheric value, the valve membrane is in its rest position and the microfluidic channel is open. When a pressure is forced through the microvalve channel, this generated pressure pushes up the valve membrane which closes the channel.

Figure 3.7. Working principle of (a) thermo-actuated valves and (b) pneumatic valves.

The membrane valve layer was optimized since the 50 µm layer took too long to open the channel and release the membrane. Different thicknesses were tested finding the optimal at ~ 150 µm obtained by spinning PDMS at 300 rpm.

The pneumatic channels are designed in a such a way to don't have an outlet, due to the PDMS permeability to gases. They are only filled with DI water by filling the capillary tubing and applying about 200 kPa of pressure. By using water, it's possible to effectively actuate the valves without running the risk of generating air bubbles in the medium by diffusion of gas through the PDMS membrane [8].

The activation of the valves is controlled by three-ways valves themselves connected to a pressure regulator and a pressured-air line.

3.3.2   Previous chamber design

Compared to a previous project described in the doctoral thesis of Andleeb Zahra, the microfluidic reaction chamber is increased in size because of the biological requirements on sample volume. Indeed, thanks to the collaboration with chemists and biologists, the need to have a greater reaction volume has shown up. For this reason it has been increased from almost 2 µl to about 4 µl. The shape of the central heater has also been changed from chirp geometry we switched to double concentric spiral heater as described in Sec. 2.1.1.3 in order to get a uniform temperature distribution. New simulations were performed to determine the temperature uniformity (as described in the Sec. 2.1.1.3) and the optical distance

between the valves and the process chamber. According to the simulation results reported in Fig. 3.8, this distance was set at 7.6 mm to reduce the temperature interference and also ensure the temperature uniformity inside the chamber.
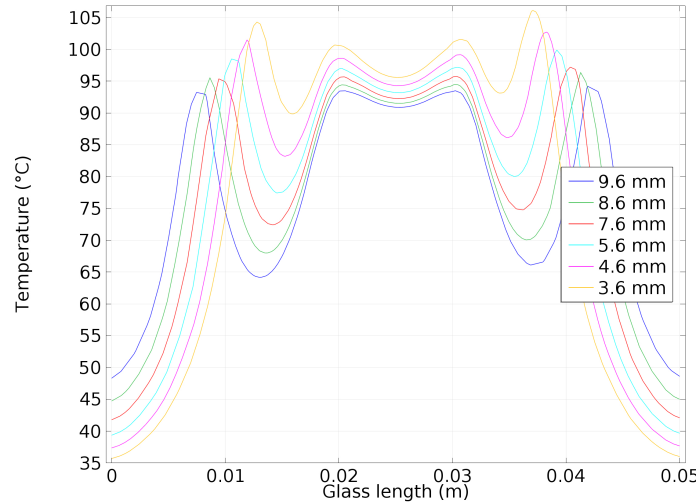
Figure 3.8. Simulation results: both central heater and valves heaters are ON. The curves are simulated for several valve-process chamber distance.

As regards the height and the width of the channel, they remained unchanged: $500 \mu m$ in width and $50 \mu m$ in height.

The designing of microfluidic system has been done in AutoCAD according to modeled values. Dimensions of channel, chamber and valve diameter are reported in Fig. 3.9. The area of PCR chamber is $(8 \times 8.5) \, \text{mm}^2 + 2(0.5 \times 12) \, \text{mm}^2 = 68 \, \text{mm}^2 + 12 \, \text{mm}^2 = 80 \, \text{mm}^2$. When multiplying by the height of $0.05 \, \text{mm}^2$ we obtain $4 \, \text{mm}^3 = 4 \, \mu\text{l}$. This volume is for example sufficient to produce a cycle of micro PCR.
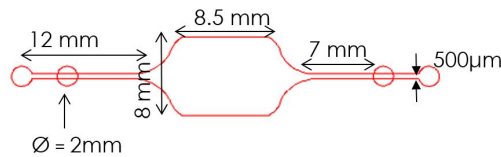
Figure 3.9. Microfluidic network integrating reaction chamber and valves. All dimensions are also reported.

Some problems occurred during the experiments, due to the formation of air bubbles during the chamber filling, as shown in the Fig. 3.10. As heating started, the air began to expand generating a very big pressure and causing the overall liquid loss. Another problems was represented by the collapse of the valve control layer. Structures with low aspect ratio height/width (less than 1:10) are prone to collapse, as will be well explained later. In order to overcome these problems, serpentine geometries (more similar to a channel shape) have been designed, taking into account the volume fixed by the biological conditions and the position of the channel on the photosensors.

Figure 3.10. Fabricated microfluidic network aligned with the DARWIN'S device: air bubbles expansion during the PCR heating.

3.3.3 Serpentine shaped microfluidic chamber

Several solutions for the chamber shape were designed.

1. a chamber maintaining the old geometry but containing micropillars (pillar diameter $\approx 200 \mu m$), to convey the fluid through capillary forces;

2. two serpentine shaped microfluidic chambers (see Fig. 3.11). The smaller one has three channels corresponding exactly to the three rows of sensors, while the other one has two more channels to increase the volume.
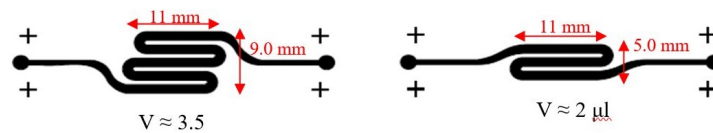
Figure 3.11. New reaction chamber design.

COMSOL simulations were also carried out to verify the filling of the different geometries. According to these simulation data, the serpentine shapes were fabricated (Fig. 3.12) to test the filling both with god results. We decided to use the bigger one for the possibility to have a bigger volume for the reaction chamber.

Figure 3.12. Fabricated PDMS serpentine chamber still bonded on the valves mold.

3.3.4 Results of the research work as visiting scholar at INESC-MN research center

This part has been developed during my stay in the laboratory of the INESC-MN (Instituto de Engenharia de Sistemas e Computadores para os Microsiste- mas e as

Nanotecnologias) research center in Lisbon.

In this period I have addressed the issues occurred during the first tests of the device with the new serpentine chamber during the on chip PCR implementation. The major issues were related to liquid leakage and liquid evaporation. As will be described in par. 4.1, the performed PCR is composed by 30/40 thermal cycles and by an initial DNA denaturation step at 95, °C for about 20 minutes. We noticed that the reaction chamber appeared mostly empty, after almost 1 h 30 min /2 h of experiment. Following studies and literature research showed that the reasons for this emptying could essentially be two:

- an improperly sealing of the pneumatic valves, due to the excessive pressure generated during the PCR;

- the evaporation of the solution and the permeabilty of PDMS that jointly caused the sample loss.

In particular, the evaporation of sample solution during thermal cycles is especially significant during the PCR denaturation step, when the system temperature approaches 100 °C. This would result in reagents loss and concentration changes that are particularly critical for volumes within or below the microliter range. In all-PDMS chips, water volume reductions of about 60% in 120 min at 20 °C and of 100% in less than 4 min at 95 °C were measured [73]. To date, sample evaporation still remains an important limitation to the applicability of many microfluidic devices using very small volumes. Different proposed strategies include the use of valves and other elements for increasing the gas pressure around the sample [73].

3.3.4.1 Valve sealing

The first step was to investigate the valve sealing, namely their ability to withhold the pressure generated in the microfluidic chamber. Referring to the PCR experiment, the increasing pressure is caused by degassing and air expansion at elevated temperature. If the valve fails, the PCR sample will be pushed out of the PCR chamber, resulting in failed PCR reaction. The amount of pressure required to prevent degassing has been estimated by Chou et al [13] to be about 3.1 psi. The evaluation was performed using solubility data for air in water and Henry's law. The presence of an air gap between the valves and the PCR chamber will cause additional internal pressure build up. Heating of this air gap will generate an additional 3.7 psi pressure at 94 °C, therefore the valve must be able to withhold at least 6.8 psi (=46.88 kPa) total pressure to ensure the successful confinement of the PCR sample during thermal cycling [66].

In order to test the maximum pressure held by the valves, a small channel made in PDMS and aligned with the valve and the heater, has been designed (right part in Fig. 3.13).

The experiment has been done using a compressed air, a power supply and a microscope (see setup in Fig. 3.13). After filling the channel with red colored water and turning ON the heater at 100 °C, several pressures have been applied. In these conditions the valve behavior has been observed under the microscope and the results are shown in Fig. 3.14.
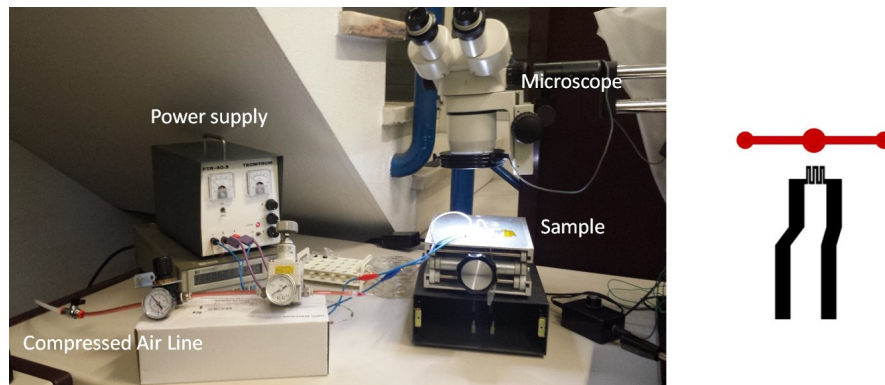
Figure 3.13. Setup for valve sealing test (left) and designed microfluidic channel and thin film heater (right).
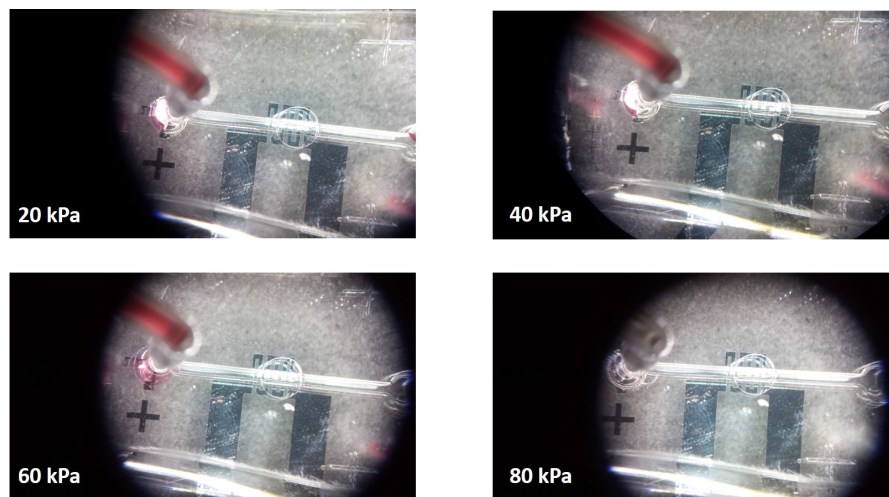
Figure 3.14. Experiment results for valves sealing at different pressure: 20 kPa, 40 kPa, 60 kPa and 80 kPa. The valves are able to withhold a pressure between 60-80 kPa.

By applying 20 kPa, 40 kPa and 60 kPa, the valve looks still closed because the tygon tube on the left side is still filled with blue liquid. On the contrary, by applying 80 kPa the valve is not able to withhold the internal pressure, let the red liquid of the tube passing through the channel and reaching the reservoir at the other end. In all the pictures, the channel is empty not for the lack of sealing but for the liquid evaporation. This experiment was repeated several times to show its repeatability. The valves are then able to withhold a pressure between 60-80 kPa, depending on the correct fabrication process and on the correct channel/valve alignment.

3.3.4.2 Adding glycerol

Another issue is the water evaporation through PDMS. This evaporation becomes critical since a significant material loss occurred from the devices containing a thinner PDMS membrane. In case of PCR, sometimes to prevent evaporation of the PCR reagents at high temperatures, the sample is enclosed in droplets of mineral oil, but in our case PCR is only one step of the SELEX process and it's mandatory to avoid sample contamination.

After several literature search, I decided to add another liquid to the solution in order to increase its boiling point. Recommended by the INESC research group, the choice fell on the glycerol, widely used for many purposes. All its properties are shown in [4]. In particular the boiling points of glycerol/water solution in different percentages are shown in Fig. 3.15.

Table 10. Boiling Points of Glycerol-Water Solutions (Calculated from Dühring Lines)												
Pressure (Mm)	Boiling point of water (°C)	(Boiling Points °C)										
		Water (%) 90 Glycerol (%) 10	80 20	70 30	60 40	50 50	40 60	30 70	20 80	10 90	4.36 95.64
760.00	100	100.7	101.6	102.9	104.5	106.7	109.6	114.0	121.5	139.8	175.8
525.80	90	90.6	91.5	92.8	94.2	96.3	99.3	103.5	110.3	127.8	161.1
355.10	80	80.5	81.4	82.6	84.0	86.0	88.8	92.8	99.3	116.0	146.5
233.53	70	70.4	71.2	72.4	73.7	75.6	78.5	82.2	88.3	104.0	132.1
149.19	60	60.3	61.0	62.2	63.5	65.5	68.1	71.5	77.3	92.0	117.6
92.30	50	50.2	50.9	52.1	53.4	55.2	57.6	61.0	66.2	80.1	103.1

Figure 3.15. Boiling points of glycerol/water solutions [4]

These values were calculated following Duhrings' rule that states:

$$\frac{T_1}{t_1} - \frac{T_2}{t_2} = K \tag{3.10}$$

where T_1 is the boiling point of a given substance at pressure P_1; T_2 is its boiling point at pressure P_2 and t_1 and t_2 are boiling points of a second similar liquid at the same pressures. K is a constant.

Our PDMS serpentine chamber has been tested adding glycerol to the solution in different percentages. I heated the chamber at 65 °C for 1 hour. The results are
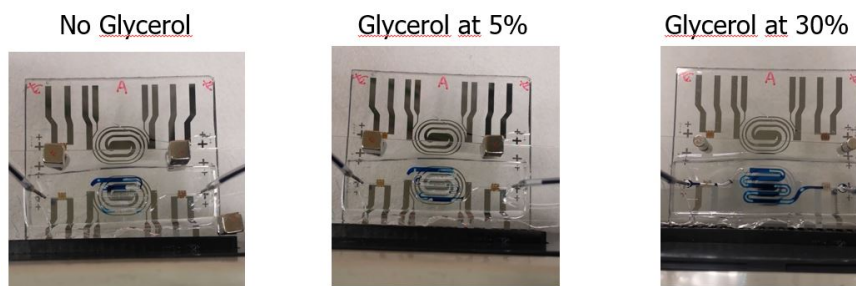
Figure 3.16. Pictures showing the experiment results with different glycerol concentration at 65 °C for 1 h.

shown in Fig. 3.16.

Obviously the higher is the glycerol percentage, the lower is the amount of evaporating liquid. However at 95 °C, the glycerol concentration needed to avoid evaporation is too high (at least more than 60%) and it can probably influence the DNA solution.

3.3.4.3 PCR chamber design

One of the major problems in the microfluidic fabrication was the sizing of the double-layer PDMS structure (see Fig. 3.17). The PDMS structure is constituted by the control layer for the valves and the thicker flow layer for the channel. The control layer is 100 μm all around and 50 μm in the valve zones in order to achieve a right deformability with a given power to the heater.
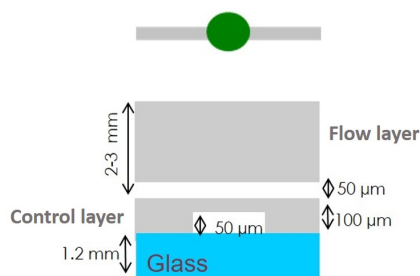
Figure 3.17. Microvalve top view and cross section.

This membrane is very thin and, during the peeling from the mold for the final PDMS-glass bonding, it deforms and blocks both the lozenge shaped chamber and the serpentine shaped one (see Fig. 3.18).

Figure 3.18. Serpentine shaped microfluidic channel (left), non-correct filling occurred during the fabrication (right).

We attributed this behavior to the low height/width aspect ratio of the channel, which is in this case set to 1:20 since the eight of the serpentine is $50\,\mu$m and the width is $1000\,\mu$m. The problem can be avoided using a ratio equal to 1:10 or using other types of valves.

- MAGNETIC VALVES
  The magnetic valve consists of a magnet immersed in the PDMS microfluidic block in correspondence to channel. The valve is actuated by bringing an external magnet in contact with the glass hosting the microfluidic channel with incorporated magnet. In this way the magnetic forces cause the membrane deformation and the consequent channel obstruction. A clear advantage of this valve design is that no secondary materials or microfabrication techniques are required to fabricate and activate the valve.
  Our microfluidic serpentine channel with incorporated magnetic valves is reported in Fig. 3.19.
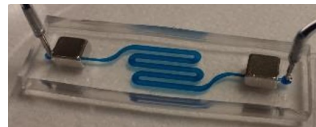
Figure 3.19. Fabricated microfluidic channel with incorporated magnetic valves.

The chamber filling is perfect and the control layer membrane is not collapsed. Nevertheless, the magnet is too large and the channel is too small. In fact, the glass characterized for the experiments is $1.2\,$mm thick. Considering that the DARWIN'S hosts the electronic devices while another glass hosts the microfluidics, the resulting magnet must have a larger force or the channel must be larger (Fig. 3.20). Neither of these things can be achieved, so this idea was discarded.
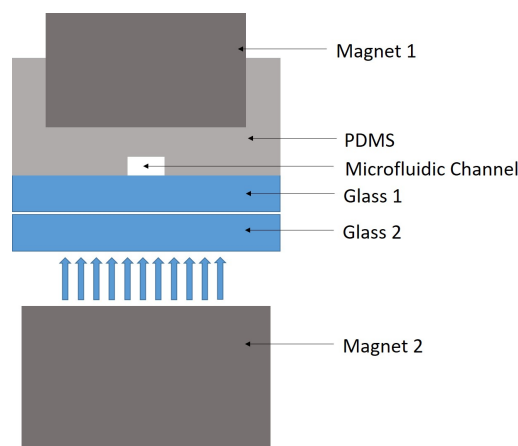
Figure 3.20. Schematic view of magnetic valve working principle. Magnet1 is immersed in the PDMS microfluidic network hosted on Glass1. Another glass (Glass2) hosts the electronic devices (It can be the DARWIN'S for example). To activate the valve another magnet (Magnet2) is brought in contact with Glass2. The magnetic forces can cause the channel obstruction.

- PNEUMATIC VALVES
  As described in par. 3.3.1.2, this kind of valve utilizes the deflection of a PDMS membrane to stop the flow by means of compressed air line.
  To avoid the problem of membrane collapse and do not have any thickness problems, in this work we implemented this type of valves on the serpentine chamber, as shown in Fig. 3.21. In particular in Fig. 3.21a the microfluidic chamber is shown in red and the two pneumatic valves are reported in green crossing it at 90°. The result of a quite good filling with the valves in closed configuration is shown in Fig. 3.21b. The channel is a bit misaligned to properly show the pneumatic valves in closed configuration.

(a) **(b)**
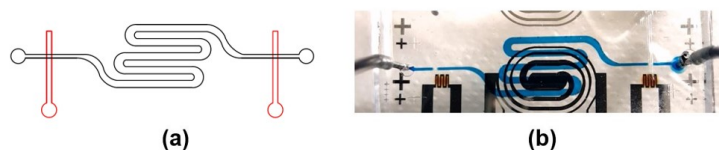
Figure 3.21. Pneumatic valves design (a); Fabricated PDMS chip with integrated pneumatic valves (b).

  I used this configuration to test the most critical step: the heating at 95 °C for DNA denaturation for 20 minutes. Fig. 3.22 shows the results: from left side, the sample before the experiment and then at 5, 10 and 15 minutes after the central heating at 95 °C. The valves work very well, they are able to withhold pressure generated in the chamber during the heating and perhaps it is possible to denaturate for 5 minutes at 95 °C, since after 10 and 15 minutes, the control membrane started to blow up like a baloon.
  The only disadvantage is that a pneumatic system requires installation of compressed air equipment and consequently the setup is more complicated.

5 min later

10 min later 15 min later
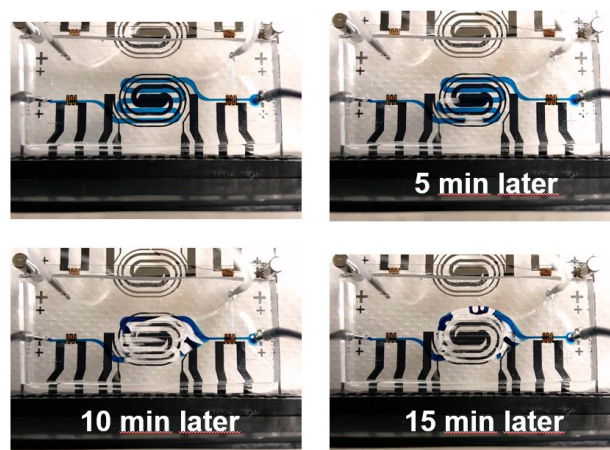
Figure 3.22. Experiment results with pneumatic valve heating at 95 °C for 15 minutes.

- THERMAL VALVES: NEW DESIGN FOR SERPENTINE CHAMBER
  Based on these previous results, I tried to enhance the work done during

the doctoral project on the thermal valves and, inspired by the experience of the Lisbon group, I designed a structure with different photoresist so as to have different thicknesses and respect the form factor 1:10 in all parts of the microfluidic channel. Therefore in correspondence of the valve the channel is $50\,\mu$m high and $500\,\mu$m wide and the mold is made in AZ40XT exactly as before; instead in correspondence of the serpentine the channel is $100\,\mu$m high and $1000\,\mu$m wide and the mold is made in SU-8 3050. In this way the sample volume is also increased: $6.5\,\mu$l compared to previous $4\,\mu$l. More details are shown in Fig. 3.23.
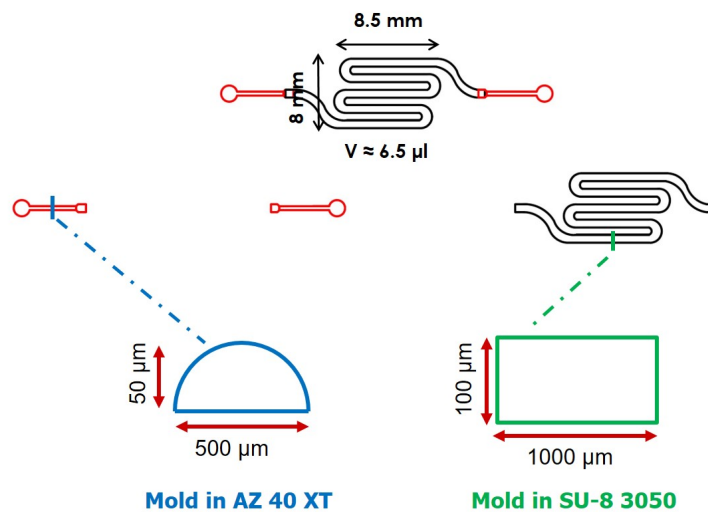
Figure 3.23. New design for the serpentine shaped chamber: (upper part) in black the $SU8-100\,\mu$m squared channel, in red the round channel in AZ40XT; (lower part) cross sections of the channels.

The fabrication procedure takes place through the classic soft lithography processes, making first the part in SU-8 $100\,\mu$m and then the one in AZ40XT. Indeed the solvents used with the SU-8 would damage the AZ40XT features. The complete fabrication procedure is reported below.

For the SU-8 $100\,\mu$m features, the silicon substrate was first baked at $150\,°$C for 5 min and then the negative photoresist SU-8 3050 (Microchem) was spun on a glass substrate at 500 rpm for 10 s (acceleration 100 rpm/s) and at 1000 rpm for 30 s (acceleration 300 rpm/s). The photoresist was soft-baked with 2 step at $65\,°$C for 10 min and at $95\,°$C for 30 min on a hot plate and then exposed under a $250\,$mJ/cm^2 UV light. The photoresist was post-baked at $65\,°$C for 1 min and at $95\,°$C for 10 min. The sample was put into the developer solution (SU-8 developer, Microchem) and baked on a hot plate at $150\,°$C for 15 min to enhance the mechanical properties of the cross-linked photoresist.

The procedure for the AZ40XT is almost the same of the one described in par. 3.2.1. The positive photoresist AZ40XT was dispensed on the top of the Si substrate to cover almost the entire substrate and it was let to settle for 4 min before the spin coating. Then it was spun on a silicon wafer at 500 rpm for 10 sec (acc. 100 rpm/s) and 1700 rpm for 21 s (acc. 1000 rpm/s) to achieve a thickness

of $50\,\mu$m. The photoresist was soft-baked with a temperature ramp from the room temperature to $127\,°$C and then baked for $7\,$min. It was exposed under $800\,$mJ/cm^2 UV light. The exposed photoresist was baked (Post Exposure Bake) at $105\,°$C for $2\,$min. The sample was put into the developer solution (726 MIF, Microchem) at room temperature for $5\,$min (Visual inspection: the time can go from 5 to 10 minutes). Finally, the mold was heated at $135\,°$C for $5\,$min for the reflow process to achieve a round shaped cross-section channel mold.

In Fig. 3.24 a picture of the mold with a zoom on the overlapping areas and the channel in PDMS filled with blue liquid is shown.
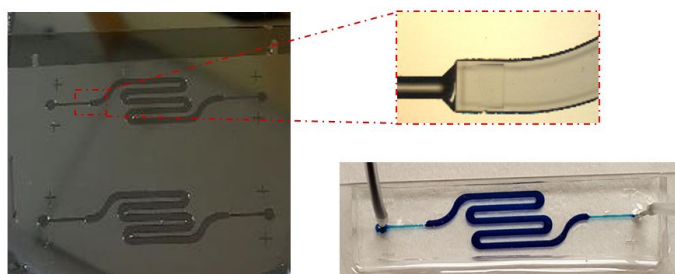
Figure 3.24. New serpentine shaped chamber mold with a zoom on the overlapping area and channel in PDMS filled with blue liquid

Depending on the ongoing projects, this microfluidics has been tested for two different purposes: an isotherm PCR (LAMP) at $65\,°$C and a standard PCR.

LAMP is an isothermal nucleic acid amplification technique. In contrast to the standard PCR in which the reaction is carried out with a series of alternating temperature cycles, isothermal amplification is carried out at a constant temperature and does not require a thermal cycler. In LAMP, the target sequence is amplified at a constant temperature of $60-65\,°$C using either two or three sets of primers and a polymerase with high strand displacement activity in addition to a replication activity.

This first test was run with water colored by a blue food color. The result is shown in Fig. 3.25: the valves were able to withhold the pressure and the sample was still there without evaporating even after 20 minutes. More detailed LAMP results will be described in Sec. 4.2.

The standard PCR is a bit more critical, especially for the denaturing step at $95\,°$C, when most of the liquid evaporation occurred. In the Fig. 3.26, pictures of a 15 cycles PCR are reported. The sample starts to evaporate from the beginning of the experiment, when only the valves are closed (because of the high closure temperature of the valves themselves). After 15 cycles, the situation is the one shown in the middle, while the final situation with heater and the valves off is reported in the bottom of the figure. Basically the valves work well, since the sample is still present in good quantity even after about two hours of experiment.
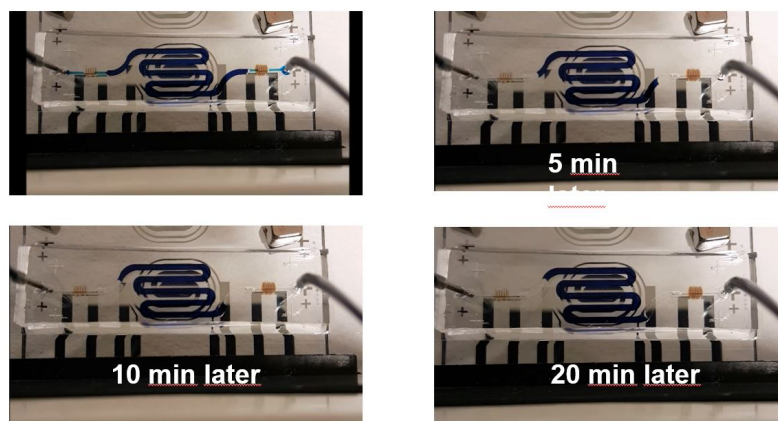
Figure 3.25. Results of the isothermal PCR experiment implemented at 65 °C for 20 min.
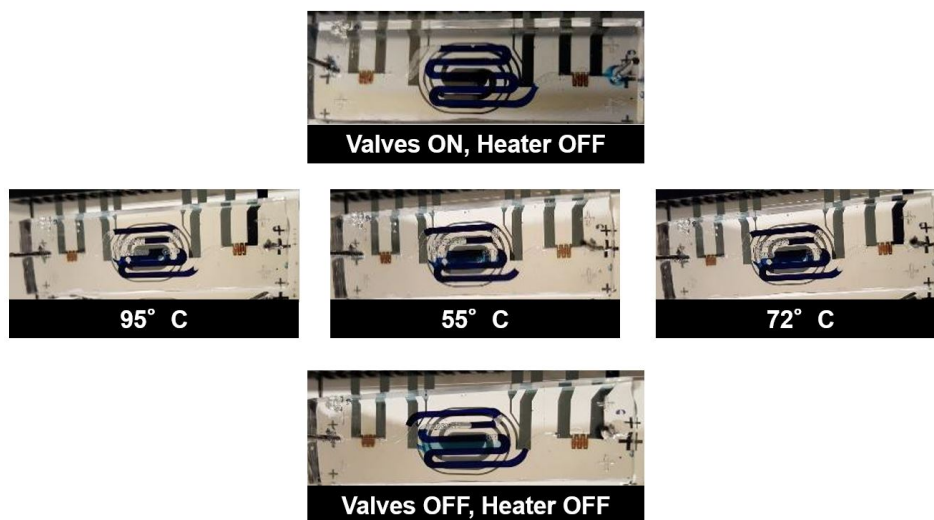
Figure 3.26. Results of the standrard PCR experiment: top part, initial situation with valve heater ON and central heater OFF; middle part, situation at the three different temperatures after 15 cycles; bottom part, situation at the end of the experiment with both heaters OFF.

So it was possible to test the PCR, optimizing the denaturation temperature according to the selected DNA. The results will be presented in Sec. 4.1

3.3.4.4 INESC-MN projects

During my stay in Lisbon, I also worked on a project developed in partnership with the research group of INESC-MN. It regards a versatile and relatively inexpensive method to perform chromatographic screening studies with reagent consumption in the μl range and rapid output of results using an integrated microfluidics device.
The chromatographic separations is often used for the purification of monoclonal anitbodies (mAbs). This technique is quite robust but requires time-consuming optimization on a case-by-case basis.
The developed chromatographic assay was combined with a signal acquisition module by coupling $200 \times 200 \, \mu m$ a-Si:H photodiodes with an integrated fluorescence filter. Binding kinetics for the adsorption/desorption of a fluorescent conjugate mAb-Alexa 430 to a multimodal chromatography ligand were measured in real time at resin level under different pH conditions.
Different microfluidics were tested for the final platform, in particular we chose to design first the thermal valves, well known by the Sapienza's group, and then the pneumatic valves.

- **Thermal valve on chromatography device**
  To integrate the thermal valves on chromatography device, first COMSOL simulations were carried out according to the size of channels, of the valves and of the control layer membrane. In fact it was necessary to optimize the thicknesses and dimensions in order to avoid an excessive heating of the glass substrate and then of the biological sample, closing at the same time the channel with the valve activation. In Fig. 3.27 the simulation results (percentage of free channel area -100% totally open, 0% totally closed- as a function of temperature) achieved by varying different parameters are reported.

  In the upper part the analyzed structure is shown. In blue the glass hosting the grey PDMS structure comprising: valve $50 \, \mu m$ high and with variable diameter (d_Valve), channel $200 \, \mu m$ wide and $20 \, \mu m$ high and control layer membrane (h_sheet) that will deform to close the overlying channel. On the bottom left part the simulation result obtained by fixing h_sheet to $30 \, \mu m$ and varying the diameter of the valve is reported: with a diameter of $0.5 \, mm$ the temperature to which the channel is totally closed is about $120 \, °C$, with diameter of $1 \, mm$ $T = 90 - 100°C$, while with diameters of 1.5-$2 \, mm$ the temperature drops to about $85 - 90 \, °C$. The bottom right part shows the result obtained by setting the diameter at $2 \, mm$ and varying h_sheet shows: with a height of $20 \, \mu m$ the temperature to which the channel is totally closed is about $65 - 70 \, °C$, with $30 \, \mu m$ we obtain $85 - 90 \, °C$, up to $50 \, \mu m$ in which the closing temperature is $185 - 190 \, °C$. The choice is obviously: $2 \, mm$ valve diameter and a height of the control layer of $80 \, \mu m$ ($50 \, \mu m$ height of the valve plus $30 \, \mu m$ for the above membrane height. We didn't use $20 \, \mu m$ due to the technological limitations). In Fig. 3.28a the AUTOCAD design of the complete device is shown: in dark
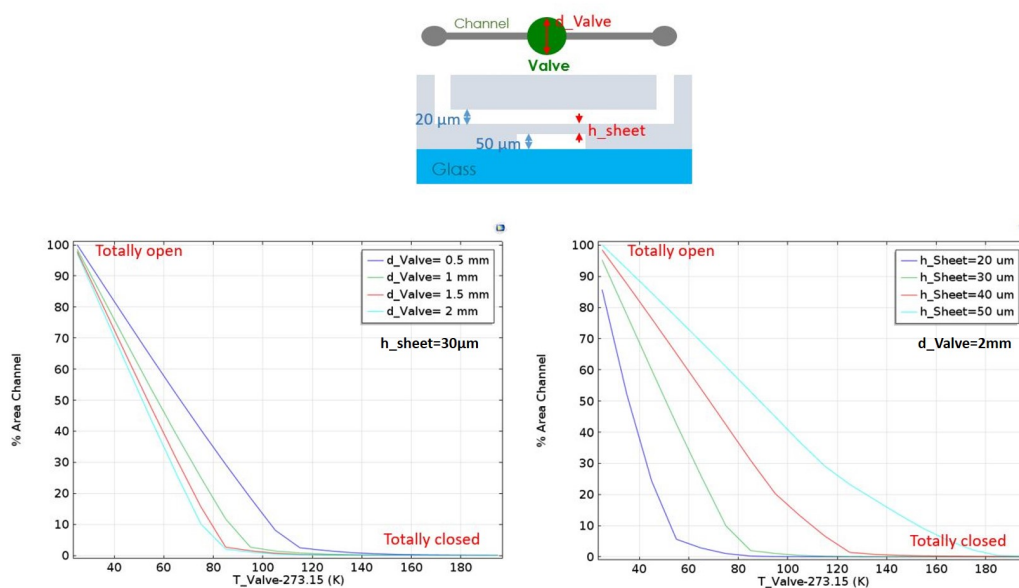
Figure 3.27. Comsol simulation results on the thermal valve for the chromatography device: top part, top view and cross section of the system (glass hosting the grey PDMS structure); bottom part, simulation result fixing h_sheet to $30\,\mu$m and varying the diameter (left), simulation result setting the diameter at $2\,$mm and varying h_sheet (right).

grey the heaters on the background, in green the round AZ40XT microfluidic channels, in yellow the valves and in red the middle part of the channel where antibodies will be collected. As repeatedly occurred, the device is double to optimize the space on the glass substrates.

The device has been fabricated and tested filling external reservoirs with colored liquids and then pulling by a syringe pump (Fig. 3.28b). Unfortunately, since the valves do not respond instantaneously, as shown in Sec. 3.3.1.1, syringe pumps cannot be used since they continue to pull air causing the bubbles formation, dangerous for the antibodies. It was also inconvenient because of the pressure build-up allowing the liquid passing through the whole channel without control when the valves were opened.

This solution was then quickly abandoned.

- **Pneumatic valves on chromatography device** [2]
  The structure design is shown on the left side of Fig. 3.29, quite similar to the thermal valve. The only difference is that there is no heater and the valves are not circular but like a "l-shape" channel in which liquid is pushed by a compressed air line. On the right part of the figure a picture of the fabricated PDMS chip device is shown together with a zoomed detail on the overlapping

---

[2]This work has been presented as a Poster "Development of a microfluidic device with integrated valves and photodiodes for rapid optimization of chromatographic separations of monoclonal antibodies" at the MicroTAS Conference, 9-13 October 2016, Dublin-Ireland and at ISPPP16 Conference, 6-9 November 2016, Salzburg- Austria, always as a Poster "On-chip chromatography for rapid screeningof multimodal ligand-target interactions"
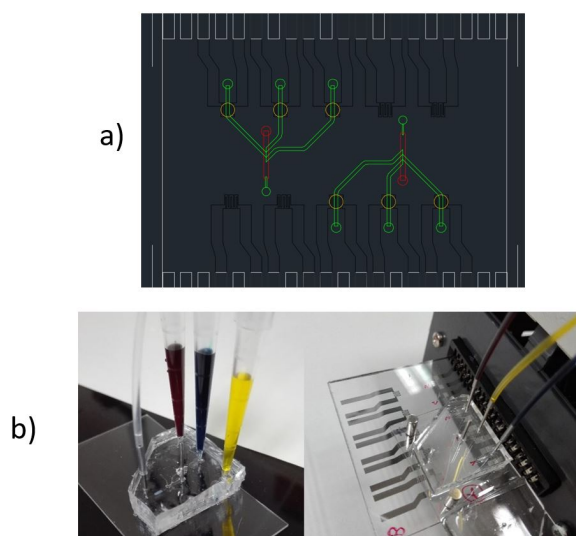
Figure 3.28. a) AutoCAD interface for the thermal valve on chromatographic device; b) Fabricated PDMS chip with the colored liquid reservoirs on the left and the complete aligned chip with the heaters and the external connection.

area. The first tests were very simple with colored liquid to verify the correct operation of the valves. The setup was very similar to the one previously described: compressed air line, pressure regulators, three-way valves, syringe pump to pull liquid. The complete system worked very well and the valves were able to close the channel instantaneously with a pressure lower than $50\,\text{kPa}$.
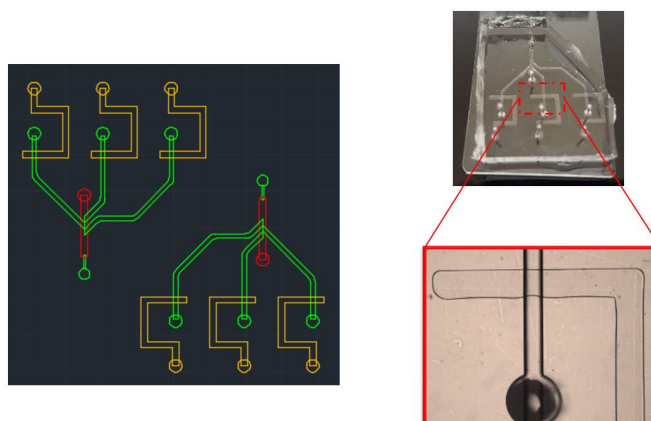
Figure 3.29. Pneumatic valve on chromatographic device (left); fabricated PDMS device and a microscope zoom on the overlapping region (right).

In particular, the microfluidic device (Fig. 3.30A) was fabricated using standard PDMS soft lithography. The fabrication process was performed in three main steps: (i) fabrication of an aluminum mask by direct write lithography from a computer-aided design and wet chemical Al etching; (ii) fabrication of

a mold containing SU-8 and AZ40XT features; (iii) fabrication of PDMS structures and sealing. The chromatography agarose beads were packed inside the micro-column ($V_{resin} \sim 35\,\text{nl}$) by pulling the liquid from the outlet using a syringe-pump. All other solutions were sequentially flowed towards the micro-column by actuating the pneumatic valves via electronic switches, while continuously applying a negative pressure at the outlet. Adsorption and elution cycles using the pneumatic valves were continuously monitored using an inverted fluorescence microscope. The $200 \times 200\,\mu\text{m}$ a-Si:H photodiodes were fabricated using photolithography and radio frequency PECVD. For fluorescence measurements, the excitation light (blue-violet laser, $\lambda = 405\,\text{nm}$) was filtered by an integrated a-SiC:H layer ($1.6\,\mu\text{m}$) also deposited by rf PECVD, whereas the emission light entered the photodiode through an ITO transparent top contact (Fig. 3.30B). The photoresponse of the a-Si:H p-i-n was measured at $0\,\text{V}$ bias.
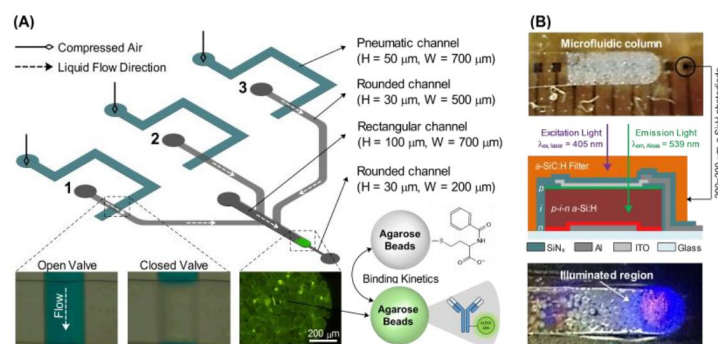
Figure 3.30. (A) Schematics of the microfluidic column with three inlet channels for sequential liquid insertion controlled by integrated pneumatic valves. (B) Alignment of the photodiode array with the microfluidic structure and cross-sectional view of the a-Si:H p-i-n photodiode used in fluorescence detection.

The chromatography ligand (Capto MMC) was studied for the capture and elution of a fluorescent conjugate mAb-Alexa 430 under different buffer pH conditions by actuating the pneumatic valves for integrated chromatographic cycles. Adsorption assays (Fig. 3.31A) were performed by flowing mAb-A430 solutions at pH 5.5 and 6.5 after equilibration of the column. In the elution assays (Fig. 3.31A), binding of the mAb occurred at a fixed pH, while the elution buffer was varied from 7.5 to 9.5. At the end of each optimization cycle, the column was regenerated with a solution of 1M NaOH. The results showed that, for both the antibody adsorption and elution, it was possible to differentiate mAb-ligand interaction kinetics in a few minutes and with reproducible results after each cycle. The integration of a-Si:H photodiodes with the microfluidic column allowed us to continuously monitor the fluorescence of the packed beads by measuring the current generated by the photosensor. Different binding kinetics were successfully measured and the results were consistent with fluorescence microscopy measurements (Fig. 3.31B).

This is a really versatile and relatively inexpensive method to perform chromatographic screening studies, with reagent consumption in the μl range and rapid
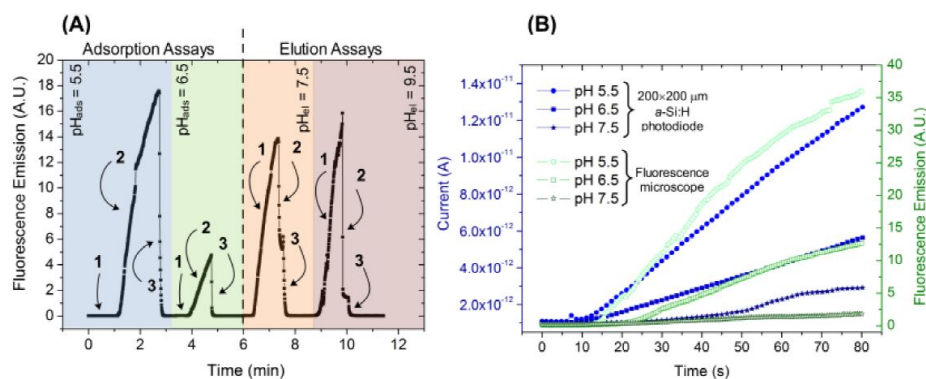
Figure 3.31. (A) Kinetics of the mAb-ligand interaction. Adsorption assays: 1-equilibration, 2-mAb-A430 solution, 3-regeneration; Elution assays: 1-mAb-A430 solution, 2-elution, 3-regeneration. (B) Fluorescence emission for the mAb-A430 binding measured using photodiodes (left axis) and microscope (right axis).

output of results (< 2 min/condition tested, against 20-30 min in a conventional chromatographic run), using an integrated microfluidics device. This platform can be extended to any type of chromatography beads and target molecule, after an appropriate labeling procedure.

Chapter 4

Device testing

In order to show that the DARWIN'S System-on-Glass can implement multiple functions, it was designed and applied to perform different experiment. In this chapter all results achieved with my research group during my PhD will be discussed. Furthermore, thanks to my Tutor, I took part in several projects of which I refer only the most pertinent to my real PhD project. In particular the first presented results are concerning the three SELEX modules (PCR, dsDNA separation, aptamers selection) carried out independently of each other. The design of the final integration will be shown in Chapter 5.

4.1 Application in PCR[1]

In this section the DARWIN'S application for the implementation of DNA amplification through the PCR with thermal cycling among three different temperatures on a single site will be presented. The DARWIN'S glass has been connected to an electronic system that drives the heaters and controls the temperature and light sensors. It has been optically and thermally coupled with another glass hosting a microfluidic network made of polydimethylsiloxane that includes thermally actuated microvalves and a PCR process chamber. PCR cycles were performed as follows: $95°C \times 20$min, then 30 cycles of ($95°C \times 30s$, $55°C \times 30s$, $72°C \times 30s$). The successful DNA amplification has been verified off-chip by using a standard fluorometer (an ABI 7500 Fast- Applied Biosystems) and compared with that achieved with a standard PCR equipment.
More details on DARWIN'S design and fabrication are reported in Chapter 2.

4.1.1 PCR experiment

PCR technique provides amplification of specific nucleic acid sequences and finds applications in genome sequencing, molecular diagnosis of disease, environmental testing, food technology, agriculture, and forensic science. As explained, the PCR mechanism is based on the sample thermal treatment, which are usually implemented with an external metal block and few examples of heaters integrated on LoC have

---

[1]This paragraph is based on the paper *"Multifunctional System-on-Glass for Lab-on-Chip applications"* Petrucci, G., et al., Biosensors and Bioelectronics (2016) [70]

been presented [28]. Even though isothermal amplification microsystems have been presented and applied for many applications [3], they can be however used for any target needing special designed primers, which cannot be always applied. The widely used PCR on-chip have been reported in literature [103]- [104] and research is still very active in this field due to the several advantages compared to the standard one. In this work, we accomplish with the standard three-temperature cycling technique: each PCR cycle consists of the melting of the double-stranded DNA (about 95 °C), annealing of the specific primers to their target gene (usually between 50 and 65 °C) and extension of primers with thermo stable polymerase enzymes such as Taq polymerase (near 72 °C). Therefore, we need to precisely control the temperature so as to obtain the desirable temperature kinetics for DNA amplification.

The experimental setup for the implementation of the PCR is shown in Fig. 4.1. It includes:

- the SoG electronically connected to an electronic board;

- a personal computer, connected to the electronic system through a USB port;

- a disposable microfluidic network where the DNA amplification is performed;

- a fan that controls the cooling rate.
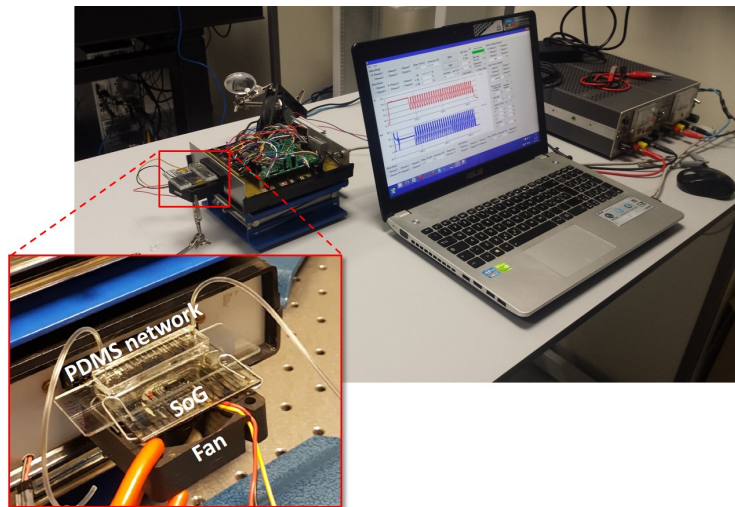
Figure 4.1. Scheme of the experimental setup utilized for the DNA amplification.

We performed the PCR steps on one single chamber by changing the temperature on the active area with an electronic control and a cooling system. The glass hosting the microfluidic network has been placed over the SoG aligning by eye the microvalves and the process chamber with the heaters (Fig. 4.1).
The integrated glass was then connected to the electronic board that drives the heaters, biases the diodes and reads the voltage across the diode (developed by another PhD student, Nicola Lovecchio). Taking into account that the diode voltage varies linearly with the temperature when the diode is biased at constant current, the

temperature control has been performed through an auto-tuned Proportional-Integrative-Derivative (PID) algorithm running on the PC. The control takes as input the diode voltage drop and applies the voltage to the thin film heater in order to achieve the set-point temperature specified by the user in the fastest time and with the minimum sovra-elongation and ripple. Cooling of the SoG has been achieved by using a fan driven by the same electronic board that controls the SoG operations. In particular, the fan is turned on at the end of the denaturation step (occurring at 95 °C) and is turned off when the PCR chamber temperature reaches 55 °C. At this point the PID algorithm controls again the SoG temperature driving the heater with the appropriate voltage. We achieved heating rate of 2 °C/s, cooling rate of 1 °C/s and ripple equal to ± 0.5 °C.

PCR experiment has been implemented using a c-DNA obtained through retrotranscription of RNA extracted from mouse myoblasts and amplifying the mRNA from the Hprt gene. A 15 μl sample containing 5ng of c-DNA, 5 μM oligonucleotides, DNA polymerase and SYBR green were mixed in a vial. Subsequently 6.5 μl of this sample were inserted in the microchannels by using a Hamilton syringe. After filling the serpentine-like microchannels, the PCR has been implemented through the following steps:

1. driving of the two lateral heaters to close the thermoactuated valves. The temperature needed for this operation is around 100 °C [102];

2. driving the heater below the process chamber with the PID algorithm to achieve the PCR cycle: 30 s at 95 °C, 30 s 55 °C and 30 s at 72 °C (for dsDNA denaturation, oligonucleotides annealing and DNA synthesis respectively).

Step 2 has been repeated 30 times. At the end of the PCR process, the central heater and the lateral heaters were turned off. Subsequently, the sample was collected from the PCR channel by rinsing at 20 μl/min for 5 min. The collected sample was lyophilized and re-dissolved in 6.5 μl of phosphate buffer and transferred in a PCR microwell plate. The microplate was inserted in a standard PCR operation system in order to detect the fluorescence signal deriving from the amplified DNA (AB2720 thermal cycler- Applied Biosystems). This procedure is necessary to verify whether the PCR cycles worked correctly into the device. The analysis showed that amplification occurred. The blue bar in Fig. 4.2 represents the average fluorescence intensity of the SYBR green intercalated in the dsDNA amplified on chip calculated over the three independent experiments. The standard deviation has been found to be ± 10% of the average value. The SYBR green can emit luminescence exclusively if intercalated in the dsDNA due to its interaction with the base pairs, thus the higher is the concentration of the dsDNA in the sample, the higher will be the fluorescent signal. The result achieved with our chip was compared with that obtained amplifying the DNA by using a thermal cycler and by applying the same temperature cycles. The intensity of the average fluorescent signal (calculated over three independent experiments) deriving from the SYBR intercalated in the amplified dsDNA is reported in Fig. 4.2 (red bar). The standard deviation has been found to be ±5% of the average value. The fluorescent intensity of the signal coming from the PCR on-chip resulted to be comparable with that achieved by the standard PCR operation system.
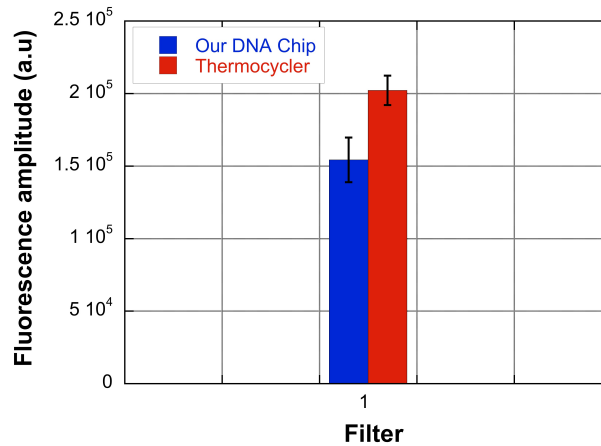
Figure 4.2. Fluorescent signal resulting from the spectrofluorometer after the successful DNA on chip amplification (blue bar). The red bar refers to the results achieved with a standard PCR system. The error bars (vertical black lines) represent the standard deviation measured on three experiments.

Even though more experiments are needed to achieve a complete characterization of the performances of our PCR system, as for example the determination of the PCR efficiency, this result demonstrates that the SoG is well suited for thermal treatment necessary in diverse biochemical processes.

Current efforts are being directed on the testing of the on chip detection using the a-Si:H photosensors already present into the LoC system.

4.1.2 Optimization of ds-DNA melting step and new PCR experiment

In order to perform PCR in the microfluidic chip, preliminary experiments have been conducted to observe the effect of the temperature variation on the microfluidic chip filled with a buffer solution. Varying the temperature between 55 °C to 95 °C we noticed bubbles formation above 80 °C causing partial evaporation of the sample and leading to irreproducible values of the amplification efficiency for samples under the same amplification conditions.

In order to avoid the bubble formation, we investigated whether the melting temperature could be decreased below 80 °C. The PCR process was conducted using a standard commercial thermocycler and varying the temperature of melting between $76 - 90$ °C. PCR was done in an Applied Biosystems 2720 Thermal Cycler. HOT FIREPol DNA Polymerase- Solis BioDyne and the supplied buffer were used with the following cycling program (15 min 94 °C; 15 cycles: 20" X °C, 1 min 62 °C, 30" 72 °C; (X= 94 °C, 90 °C, 85 °C, 80 °C, 76 °C) hold 4 °C). A PCR reaction mix (20 nM ssDNA template, 1 μM of each primer, 0.2 mM dNTPs, 1.5 mM MgCl$_2$) was prepared in Reaction Buffer and an aliquot was stored as CTRL mix. To the remaining sample a Hot Start Taq enzyme (HOT FIREPol DNA Polymerase Solis BioDyne) was added to a final concentration 0.05 U/μl. Samples of 20 mL were amplified and analyzed by agarose gel electrophoresis.

The gel electrophoresis conducted for each sample showed that the amplicon was formed for each selected temperature (Fig. 4.3). PCR product formation was monitored by agarose gel electrophoresis (4% agarose gel in TAE running buffer, ethidium bromide staining, 130 V, run time 20'). Sample of $5\mu l$ per lane were used. We see that even at lower temperature ($76\,°C$) the line corresponding to the amplified DNA is very well distinguishable.
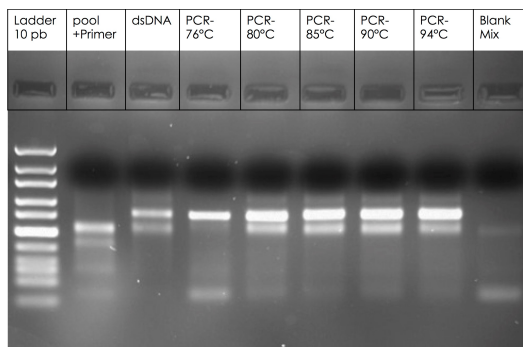
Figure 4.3. Gel electrophoresis of dsDNA after the PCR amplification by applying different denaturation temperatures. dsDNA is the product of a PCR reaction conducted under the optimized conditions for this template and primers, used as reference/standard product.

Taking into account these results, the PCR on chip was conducted using the following procedure: 20 s at $76\,°C$, 60 s at $62\,°C$ and 30 s at $72\,°C$. In order to activate the Taq polymerase, the solution containing oligonucleotides, ssDNA and DNA polymerase was off-chip heated at $94\,°C$ for 15 min. Subsequently, $30\,\mu l$ of that solution were flowed into the channel using a Hamilton syringe. The PCR was conducted varying from 5-15 the number of thermo-cycles. PCR of 15 cycles was also performed using a solution without Taq polymerase (Blank).

The efficiency of amplification was verified off-chip: the channel was rinsed with phosphate buffer and the sample collected was lyophilized. Subsequently, 1mL of a phosphate buffer solution containing $[Ru(phen)_2(dppz)]^{2+}$ 0.1 mM was added to each sample. $[Ru(phen)_2(dppz)]^{2+}$ is a light switch complex [47], has no luminescence in aqueous solution as the triplet metal to ligand charge transfer excited state is quenched by hydrogen binding between water and the phenazine nitrogen of the ligand. When it binds to dsDNA, the interaction between the ligand and the base pair of duplex nucleic acid protects the phenazine nitrogen from water, leading to an intense emission.

The PCR amplified samples were analyzed by fluorescence spectroscopy. As expected the analysis showed an increase of the fluorescent signal proportional to the number of the performed cycles (Fig. 4.4). The blank signal showed the same luminescence intensity of the solution containing only $[Ru(phen)_2(dppz)]^{2+}$.

The samples were also analyzed by gel electrophoresis, to verify that the right strand of ssDNA was amplified (Fig. 4.5).

The gel-electrophoresis proves the amplification of the ssDNA to the desired dsDNA, moreover no amplification was observed for the blank sample, thus confirming the results obtained by fluorescence spectroscopy.
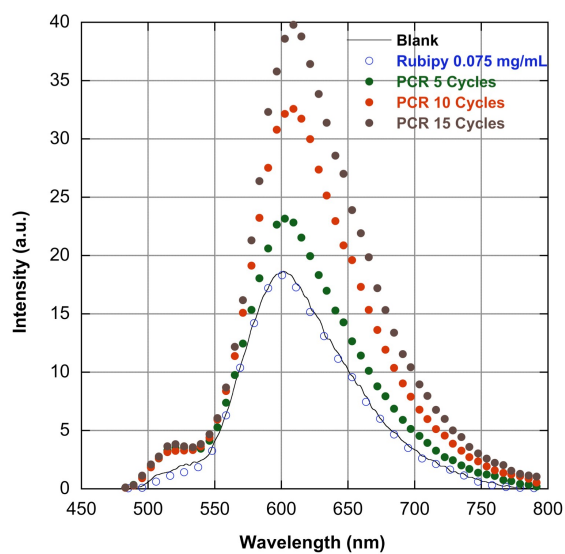
Figure 4.4. Luminescence emission spectra of the PCR amplified product varying the number of cycles.
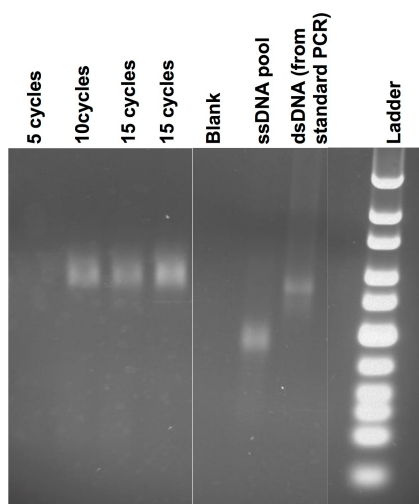
Figure 4.5. Multiplex PCR results of PCR, in the PDMS microfluidic chip and by standard thermocycler.

4.2   Isothermal PCR [2]

The present paragraph describes another DARWIN'S application for viral DNA amplification and real-time quantitative detection under constant temperature (65 °C). To this aim, a loop-mediated isothermal amplification (LAMP) technique was optimized to specifically amplify parvovirus B19 DNA and coupled with Bioluminescent Assay in Real Time (BART) technology to provide real-time quantitative detection of target DNA. To enable on-chip LAMP-BART, the DARWIN'S integrates all the elements necessary for temperature control and on-chip detection of the evolving bioluminescent signal. During the experiment, all the reagents are contained in a disposable 10 μl polydimethilsiloxane (PDMS) chamber, designed to ensure optimal thermal and optical coupling. All the elements are well shown the device top view reported in Fig. 4.6. A dedicated electronics is employed to control the chip temperature along the whole experiment and read-out the photosensor currents.
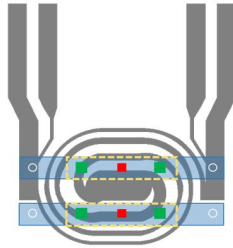
Figure 4.6.   Top view of the two microfluidic channels (blue rectangles), showing the alignment with the a-Si:H photosensors (green squares) and temperature sensors (red squares). The gray lines represent the profile of thin film heater, the white circles are the holes for the inlet and the outlet of each channel, the dashed yellow rectangles represent the useful area of the microfluidic channel analyzed with the photosensors.

Presently, isothermal nucleic acid amplification techniques (iNAAT) are receiving growing attention, as they are particularly suited for their point-of-care implementation. Indeed, they only require application of a constant temperature (typically comprised between 40 and 65 °C) along the whole amplification process, thus greatly simplifying the on-chip thermal control task and reducing operating energy consumption. In particular, loop-mediated isothermal amplification (LAMP) is emerging as a very promising technique, offering high specificity, sensitivity, rapidity and simple detection of amplification products [67]-[76].
In this work, a LAMP technique for the detection of parvovirus B19 (B19V) DNA has been developed and the experimental factors affecting its specificity and sensitivity have been evaluated. B19V was taken as a model pathogen virus, as it is a ubiquitous virus, responsible of a variety of clinical manifestations and found in different biological specimens. it is responsible for a variety of pathological manifestations in humans. In particular, B19V infection in pregnancy can cause severe fetal anemia

---

[2]This paragraph is based on the manuscript in preparation *"On-chip LAMP-BART reaction for viral DNA real-time bioluminescence detection"* in collaboration with Alma Mater Studiorum-University of Bologna.

and nonimmune hydrops fetalis, which may lead to fetal death or to severe and irreversible neurological sequelae in survivors.

The LAMP for B19V DNA, at first optimized in a closed tube format exploiting conventional equipment, was subsequently implemented in an integrated chip device. In particular, temperature resulted to be crucial for specificity of the reaction, thus confirming that on-chip integrated real-time temperature control is a key aspect to ensure reliability of results.

To obtain quantitative information and detectability suitable for diagnostic applications, highly sensitive real-time detection must be applied during LAMP. Therefore, we coupled B19V DNA LAMP with the Bioluminescent Assay in Real Time (BART), which relies on the enzymatic conversion of inorganic pyrophosphate, produced stoichiometrically during nucleic acid synthesis, into ATP (by ATP sulfurylase in the presence of adenosine-5'-O-phosphosulphate), which is then detected employing a thermostable firefly luciferase yielding a bioluminescence (BL) emission. This technique provides simple, robust and low-cost real-time monitoring of LAMP amplification in a closed-tube format, thus greatly reducing cross-contamination risks and allowing real-time quantitative detection of the target nucleic acid. It is well known that chemiluminescence (CL)- and BL-based detection principles are particularly suitable for lab-on-chip applications, as they provide high detectability and positive features for miniaturized formats. Most of the real-time nucleic acid amplification assays rely on fluorescence measurements. However, the on-chip implementation of fluorescence detection greatly complicates the chip architecture, as excitation sources and filters need to be introduced and specific geometries of the reaction cell need to be adopted to avoid interference from excitation light. In addition, high background signals can be obtained when biological samples are analyzed on chip, due to the presence of naturally fluorescent biomolecules. On the contrary, CL and BL are very specific, low-background reactions and they require very simple instrumentation for their measurement.

To enable on-chip detection of the BL signal, the DARWIN'S chip resulted fit for the purpose, since it integrates a-Si:H photosensors, fabricated with the same technological processes utilized to define the a-Si:H temperature sensors (Sec. 2.2.3). Conde's group [68] demonstrated that a-Si:H photosensors are appropriate in detecting luminescent signals coming from labeled molecules, while Mirasoli et al. [65] established that the analytical performances of a-Si:H photosensors in detecting biomolecules through CL and BL-based measurements are comparable to those of crystalline silicon cooled charge-coupled device (CCD)-based state-of-the-art laboratory imaging instrumentation. Additionally, the low deposition temperature (below 300 °C) enables the possibility to use glass, the traditional support for biochemical analysis, as substrate for the a-Si:H photosensors.

4.2.1   Device design

4.2.1.1   DARWIN'S thermal design and characterization at $65°C$

The thin film heater has been designed to ensure a uniform temperature distribution over the entire area where the LAMP-BART reaction and DNA amplification occur.

The double concentric spiral heater (par. 2.1.1.3), which detailed geometry is reported in Fig. 4.6 together with the sensors and the microfluific channel, was found to very well satisfy design specifications. The temperature distribution was modeled by using COMSOL Multiphysics software, as previously occurred. Material selection and layers thicknesses have also been designed aiming to achieve a low resistance that could be driven with a USB supply (at maximum 5 V and 500 mA). To achieve a resistance of 11 Ω, the heater is a three metal stack layer of Cr/Al/Cr with thicknesses equal to 100 nm/600 nm/100 nm, respectively. Fig. 4.7a reports (in color scale) the modeled temperature distribution achieved on the glass side hosting the a-Si:H/a-SiC:H sensors, when a voltage equal to 2.57 V is applied to the heater. Fig. 4.7b represents a zoom of Fig. 4.7a, showing the glass areas (10 mm × 2.5 mm) located between the photosensors. In these areas the average temperature is 65.4 °C,
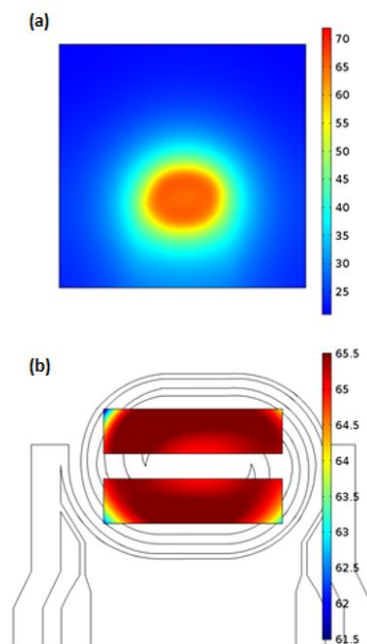
Figure 4.7. Modeled temperature distribution, achieved on the glass side hosting the a-Si:H/a-SiC:H sensors, when a voltage equal to 2.57 V is applied to the heater (a); zoom of Fig. 4.7a, showing the glass areas (10 mm × 2.5 mm) located between the photosensors (b).

the minimum temperature is 62.0 °C and the maximum temperature is 65.9 °C. Comparing these values with the color scale reported in Fig. 4.7b, it is evident that the minimum temperature of the investigated area occurs only in a very small portion (the blue regions at the corners) that does not significantly affect the average temperature and therefore its effect on the device operation is negligible.

The heater performances have been characterized by measuring the temperature distribution on the side glass hosting the a-Si:H/a-SiC:H sensors using a FLIR A325 thermo camera. Fig. 4.8 reports the thermal characteristics when a voltage equal to 2.9 V is applied to the metal pads. A quite good agreement between simulations and experimental results is achieved. Indeed, the average temperature (64.9 °C) and

the maximum deviations from this value ($\pm 1\,°C$), over the area located between the photosensors (white rectangles in the above figure), are very close to those modeled and reported in Fig. 4.7b.
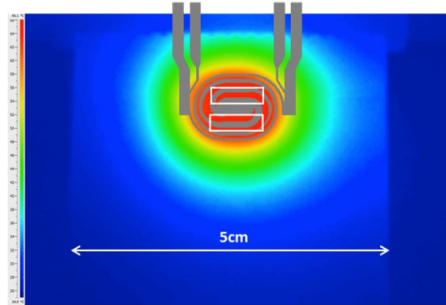
Figure 4.8. Temperature distribution experimentally measured when a voltage equal to 2.9 V is applied to the metal pads.

4.2.1.2 Microfluidic network

PDMS Sylgard 184 pre-polymer and curing agents were combined to fabricate the microfluidic network. Its typical fabrication process envisages the fabrication of a mold, the pouring of the PDMS linear polymer and the curing at a specified temperature for the complete polymerization. The developed network, shown in Fig. 4.6, includes two linear channels (blue rectangles). The dimensions of each channel ($18.1\,\text{mm} \times 2.5\,\text{mm} \times 0.195\,\text{mm}$) have been set in order to obtain the right volume for the BART implementation (about $10\mu l$). The positioning of the microfluidic network over the glass substrate guarantees a proper alignment with the photosensors (green squares) and the temperature sensors (red squares).

In our process, first, a mold was obtained by bonding a stack of three layers of $65\,\mu$m-thick kapton tape over a silicon substrate. Length and width of the tape reproduce exactly the channel dimensions reported above. A mixture of silicone pre-polymer and curing agent in the ratio of 10:1 was prepared and poured over the mold. The final thickness of the PDMS layer was about 3 mm. The PDMS was cured in oven at $60\,°C$ for 2 hours and 30 min. Finally, channel inlet and outlet holes were made by using a puncher (0.021 in. ID × 0.028 in. OD × 1.5 in. long purchased from Syneo LLC, Angleton, TX, USA). The PDMS structure was then bonded to a cleaned glass substrate.

The bonding procedure includes the following steps:

- spin coating of a thin layer of PDMS at high velocity (6000 rpm) over a glass substrate. This layer will act as a glue according to [77];

- peeling of the microfluidic network from the silicon wafer and its placing on the PDMS thin layer for few seconds;

- peeling of the microfluidic channels from the glass substrate and placing on the cleaned glass;

- baking of the whole structure in an oven at $90\,°C$ for $20\,\text{min}$.

4.2.2 BART-LAMP experiment with standard method

The off-chip LAMP-BART reaction was carried out on an assembled instrument comprising a conventional heating block for microtiter plates (Eppendorf, Germany) and an imaging system made of a MZ-2PRO CCD camera (MagZero, Pordenone, Italy) equipped with a thermoelectrically cooled monochrome Sony ICX285 CCD image sensor, coupled with a Computar (2/3 in. 8 mm, f1.4) objective (CBC AMERICA Corp., Commack, NY), and connected to a light-tight dark box to avoid interference from ambient light. The reaction was prepared in a black 384-well plate in a final volume of $20\,\mu l$, covered with mineral oil to prevent evaporation.

The optimized LAMP-BART reaction was performed at $65°C$. Real time monitoring of BL signals was accomplished throughout the amplification; light emission was recorded simultaneously for all the samples on the 384-well plate, integrated over 30-s intervals, for a 40-min total time. Images were elaborated employing the WinLight32 software version 2.91 (Berthold Technologies GmbH&Co. KG, Bad Wildbad, Germany). For each image the area corresponding to each well was selected and the BL signal integrated; the blank was measured in the area corresponding to an empty well and subtracted from each well signal. For quantification of B19V DNA, a concept of time to peak (t_{max}), which is similar to the threshold cycle (C_t) in real-time PCR tests, was applied. The t_{max} was defined as the time to maximum light output recorded during the reaction, and it is directly correlated with target DNA copy number.

To check the effects of temperature on the BART-LAMP reaction, a sample containing 103 copies of B19V DNA was amplified at $57\,°C$, $60\,°C$, $63\,°C$, $65\,°C$, $68\,°C$ and $70\,°C$ employing a closed PCR-tube configuration. End-point analysis of products on agarose gel was carried out confirming that $65\,°C$ is the optimal temperature for correct B19V amplification, as previously obtained in LAMP experiments. Once again, the strict control of the temperature is crucial to avoid false positive results occurring at temperature lower than $63\,°C$ and false negative results at temperature higher than $65\,°C$ (Fig. 4.9). Different amounts of B19V DNA were amplified in a black 384-well plate at $65\,°C$. Light emission was recorded during the amplification by BL imaging employing a thermoelectrically-cooled back-illuminated ultrasensitive CCD camera. Data light output were plotted versus the incubation time and analyzed (Fig. 4.10a).

LAMP-BART kinetic curve of a positive sample consists in a distinctive "flash" (characterized by its t_{max}, time to peak value) that is produced in real time when DNA amplification goes into exponential phase. The time taken to reach this peak of light emission is inversely proportional to the amount of target analyte. Hence, LAMP-BART technology allows for a closed tube real time quantitative evaluation of DNA in the sample and a calibration curve is generated plotting the tmax, versus target DNA amount (Fig. 4.10b). A good linear correlation between the starting B19V DNA and tmax, was retained, with a limit of detection of 10 copies/reaction. Compared to LAMP system, the reaction time of LAMP-BART was shorter and within $20\,\text{min}$ all B19V DNA targets proved to be correctly amplified (Fig. 4.10).
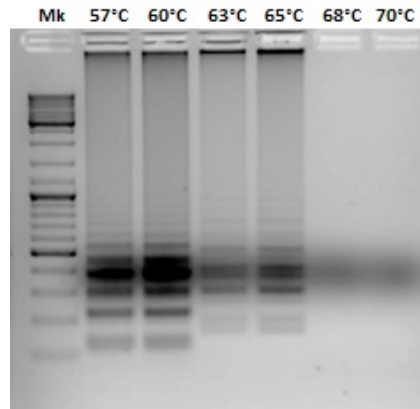
Figure 4.9. Electrophoresis analysis of BART-LAMP obtained at the indicated temperatures with a sample containing 10^3 copies of B19V DNA. Strong bands in all lanes corresponds to luciferin. Mk, 100 bps DNA marker.
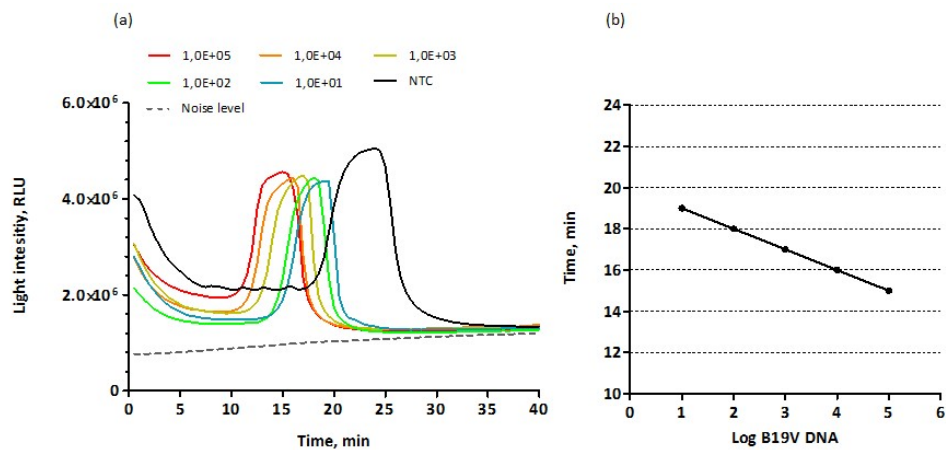
Figure 4.10. LAMP-BART light intensities recorded over 40 min of incubation at 65 °C for 10-fold dilutions of B19V DNA ranging from 10^1 to 10^5 copies/reaction and the no template control (NTC) (a); semilogarithmic plot of the time-to-peak versus B19V DNA amounts (b).

4.2.3   BART-LAMP experiment on the DARWIN'S chip

Having demonstrated the applicability of the BART-LAMP reaction to the real-time detection of B19V DNA on a 384-well format, the technique was implemented on the DARWIN'S chip in which all the elements for accurate temperature control and real-time BL detection are integrated in a single support, employing compatible processes. The LAMP-BART reaction, prepared as previously described, was assembled and mixed off-chip before the real time analysis in the integrated DARWIN'S chip equipped with the PDMS microfluidic module. The microchannel was filled up with $10\,\mu$l of LAMP-BART mixture, taking care to avoid the presence of air bubbles in the reaction chamber, and tightly sealed with adhesive film to prevent evaporation from sample inlet/outlet. The overflowing mix was carefully removed employing an absorbent paper sheet. The amplification was carried out by heating up the micro-chamber at 65 °C.

The feasibility of the microdevice was demonstrated with samples containing 10^5 or 10^7 B19V viral genomes; each experiment was repeated 3 times to ensure the robustness and reproducibility of the developed DARWIN'S chip.

The DARWIN'S chip was placed into an opaque box to prevent interference from ambient light. Photon emission was measured with a-Si:H photodiodes which absorb the impinging light and convert it in electron and hole pairs. The photo-generated carriers are collected at the sensors electrodes thanks to the electric field existing in the intrinsic region of the a-Si:H photodiode. The photocurrent is then acquired by a low-noise read-out system. The readout electronics relays on a charge sensitive preamplifier (DDC118 from Texas Instruments) that integrates the sensor current giving as output a proportional voltage. The whole electronic board is controlled by a microcontroller (PIC4550 from Microchip) that also provides the USB connection to a PC for setting of the measurement parameters (acquisition time, integration time), data storage and result visualization. At each measurement, a preliminary measurement of the sensor dark current has been performed to take into account the background signal.

A cross section of the complete structure is depicted in Fig. 4.11. The ITO and SU-8 layers below the glass substrate represent the ground plane structure that avoids interferences of the heater driving currents with the photosensor signals. A picture of the experimental set-up is also shown in Fig. 4.11.

As a proof of concept a sample containing 10^5 viral genomes was amplified and the photocurrent was recorded in real time. At the beginning of the measurement, the two-channel microfluidic network has been aligned with the a-Si:H sensors as shown in Fig. 4.11, one channel has been filled with the solution containing all the chemicals for the BART reaction and the other channel with water in order to take into account the background signal (blank or control). The inlet and outlets have been then sealed with adhesive foil. Subsequently, through the GUI of the software the diode temperature has been set to $65°C$ and the PID algorithm has been launched. The biasing current of the temperature sensors has been set to 200nA. Simultaneously, the photosensor currents have been acquired through the low-noise read-out system.

The resulting currents are shown in Fig. 4.12. The blue curve refers to a sensor
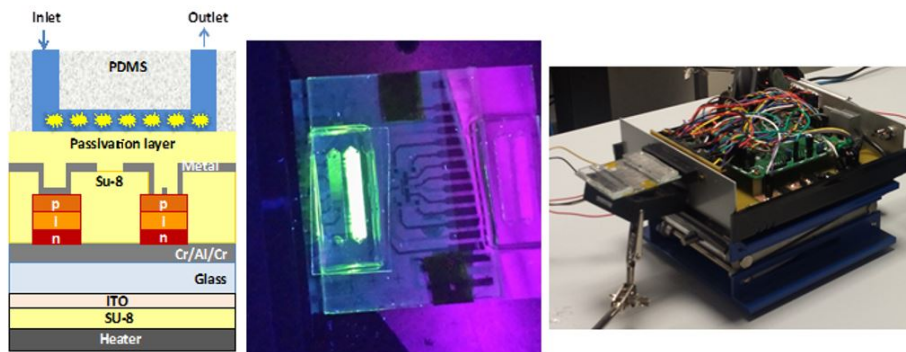
Figure 4.11. Left) Cross section of the whole device. Middle) Picture of the DARWIN'S device with the microfluidic network on it. Right) Experimental set-up used for the real-time BL detection. It includes the glass substrate hosting the heater, the a-Si:H temperature sensors and photosensors, the read-out electronics and the PDMS microfluidic network.

aligned with the channel filled with the BART reaction, the red curve refers to a sensor aligned with the control channel and the green curve is the net signal.
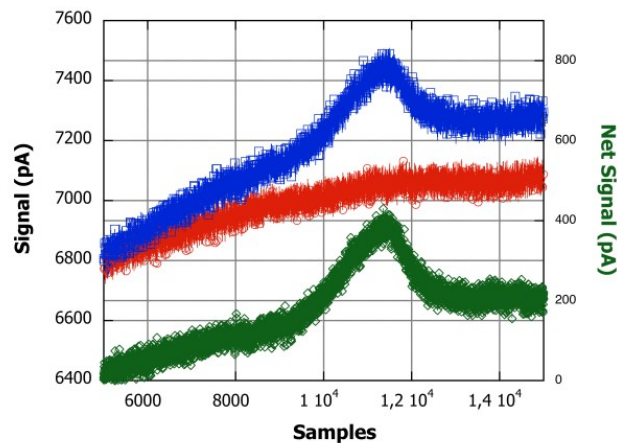
Figure 4.12. Photosensor current as a function of number of sample, acquired with the dedicated read-out electronics. The red curve is the blank signal (sensor current due to temperature only), the blue curve refers to the total signal (sum of the currents due to temperature and to the BL emission), the green curve is the net signal, only due to the BL reaction.

The increase of the blank signal is due to the dependence of the sensor dark current on temperature. The photocurrent behaviour with a Gaussian-like shape observed for the green curve confirms the results achieved in the 384-well LAMP-BART experiment and the typical signal kinetics displayed for LAMP-BART assays.
This experiment thus demonstrates for the first time the ability to display on a single integrated chip all the functions required for perform a real time LAMP reaction with on-chip optical detection. The dependence of the peak occurrence time on the initial amount of target DNA previously reported has been observed also in the

measurements performed with our integrated lab-on-chip system. Fig. 4.13 reports the net signals of two photosensors monitoring the BART reaction in a sample containing 10^7 copies.
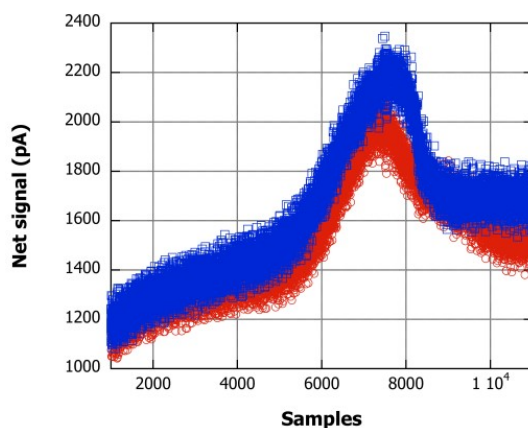
Figure 4.13. Photocurrent signals of two photosensors monitoring the BART process in a sample containing 10^7 B19V DNA copies.

We can observe that the intensity peak occurs for the two photosensors at the same time, confirming the reproducibility of the whole process. In addition, the number of samples at which the peak occurs for the 10^7 initial viral genomes results to be significantly lower than the one corresponding to a 10^5 initial viral genomes, thus preliminary confirming the ability of the system to provide quantitative information. The specificity of the reactions monitored in the two above reported experiments was confirmed with agarose gel electrophoresis and southern blot analysis.

The on-chip assay was carried out in a $10\,\mu$l chamber, which is a quite large volume for a miniaturized DNA amplification device. While small reaction volumes facilitate the achieving and maintenance of the temperature uniformity throughout the LAMP reaction, they worsen the assay sensitivity (i.e., the LOD of the assay). Indeed, low reaction volumes imply the analysis of a small volume of sample, which may contain no target DNA when deriving from a low-concentration specimen due to the stochastic variation of the sample copy number with Poisson distribution. The high specificity of the LAMP-BART reaction conducted on-chip demonstrates that the DARWIN'S system ensures good temperature homogeneity, as well as maintenance of the optimal nominal temperature value ($65\,°$C) over a relatively large surface area and on a relatively large volume of solution.

By proper design of the thin film heater and continuous thermal control through the integration of on-chip temperature sensors, DARWIN'S accomplishes the challenging tasks of ensuring optimal thermal homogeneity and, upon proper calibration, of achieving the specific temperature value that ensures the best assay specificity and sensitivity, as defined in preliminary assay optimization experiments.

4.3   On chip dsDNA separation

The separation module consists of a glass substrate hosting a thin film metal heater and a PHEMA-Streptavidin glass substrate hosting a serpentine-shaped microfluidic network (dsDNA-Chip) made in PDMS.

The thin film heater has the stacked structure and the same dimensions of the central heater of the SoG. It supplies the thermal energy needed to detach the two helices of the ds-DNA and to achieve therefore the ssDNA. Like the central heater of the SoG system, it has a resistance of $11\,\Omega$ and ensures a uniform temperature distribution (within $\pm\,1\,°C$) in the area below the serpentine-shaped PDMS network. The electronic circuit driving the heater and controlling the temperature is based in this case on the variation of the heater resistance with temperature controlled through the analog circuit reported by Scorzoni et al. in work [79]. The maximum heating rate of the circuit is practically limited by the maximum power density on the glass. We experimentally found that 600mA represents a safe current limit.

The microfluidic network, made again in Sylgard 184, has the same dimensions and shape of the flow layer of the microfluidic PCR module but does not include the control layer. The fabrication starts from the pouring of a mixture of PDMS and curing agent in the ratio 10:1 on the same mold used for the flow layer of the PCR module and proceeds with a complete curing at $100\,°C$ for $40\,min$. Subsequently, the inlet and outlet were made.

4.3.1   dsDNA separation experiment

In order to obtain a pool ssDNA for the aptamer selection towards the selected target, the amplified dsDNA must be separated. This step is usually performed using streptavidin-coated resin through which the dsDNA, having one of the strands labeled with biotin, is brought into contact. After several washing steps and the elution of the non-biotinylated strand the ssDNA is achieved [60].

In this work, the separation of the amplified dsDNA is obtained using a microfluidic chip (dsDNA-Chip) functionalized with streptavidin by growing PHEMA polymer brushes on the glass side of the channel. The dsDNA-Chip has the same structure of PCR chip, i.e. serpentine chamber having $6.5\,\mu l$ volume without the thermoactuated valves, which are not necessary since the dsDNA separation process is occurring in continuous flow. The dsDNA-Chip is positioned on the top of the integrated device, aligning the main heater with the serpentine chamber.

The product of the PCR amplification is a dsDNA having a biotinylated reverse primer, thus we tailored that once the dsDNA is immobilized to streptavidin layer, the increase of temperature up to $95\,°C$ for a few seconds would recover the non-biotinylated ssDNA representing the desired sequence to be incubated with the target molecule for the selection of the aptamer.

In order to obtain the dsDNA-Chip, a glass substrate was functionalized with PHEMA polymer brushes, further modified to immobilized streptavidin through a peptide bond (Fig. 4.14).

The layer of PHEMA brushes was chemically modified for the formation of a peptide bond with a protein, such as streptavidin, as shown in [16], [15], [17]. Briefly, the hydroxyl groups of PHEMA brush layer are reacted with succinic anhydride
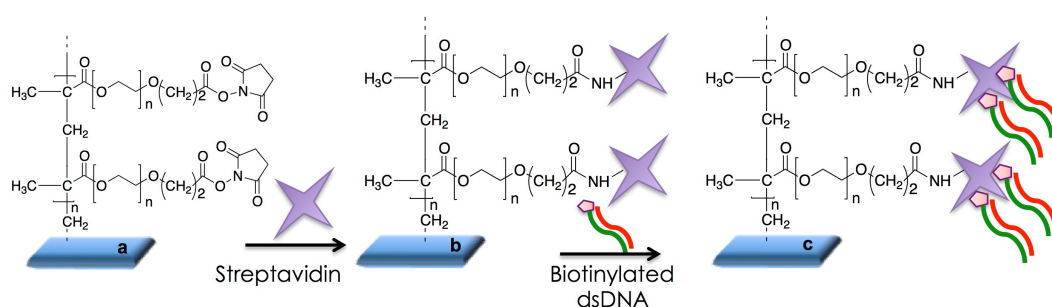
Figure 4.14. PHEMA-SA polymer layer functionalized with a) NHS (PHEMA-NHS), b) PHEMA-NHS after reaction with streptavidin (PHEMA-Streptavidin) and c) PHEMA-Streptavidin after reaction with the biotinylated dsDNA.

(SA), to obtain carboxylic functional moieties PHEMA-SA. Afterwards, the PDMS microfluidic channel is bound on the PHEMA-SA glass functionalized substrate. A solution of n-hydroxysuccinimide (NHS) was flowed into the channel to achieve NHS esters functional groups (PHEMA-NHS), after rinsing, a solution of BSA is flowed into the channel and incubated for 3 min and rinsed with both phosphate buffer and MilliQ water for 5 min at the flow rate of $5\,\mu$l/min and dried with a stream of nitrogen. This step is necessary to avoid non-specific interactions of any molecule with the PDMS layer of the channel. After rinsing with water, a solution of streptavidin was inserted into the channel and incubated over-night at $4\,°$C to form the PHEMA-Streptavidin brush layer. The channel was rinsed with MilliQ for 15 min at the flow rate of $5\,\mu$l/min and dried with a stream of nitrogen. The non-reacted NHS-ester moieties were blocked filling the channel with a solution of Blocking buffer, kept inside for 30 min. The channel was rinsed with MilliQ water for 5 min at the flow rate of $5\,\mu$l/min and dried with a stream of nitrogen. The amount of immobilized streptavidin was evaluated using the bicinchoninic acid assay (BCA assay) and is $(2.3 \pm 0.46) \cdot 10^{-2}\,\mu$g/mm^2.

The dsDNA-Chip functionalized with PHEMA-streptavidin was ready for the separation of the dsDNA. Thus, the PCR product was inserted into the dsDNA-Chip, by means a Hamilton syringe, and incubated for 10 min. The channel was rinsed with phosphate buffer at the flow rate of $15\,\mu$l/min for 5 min for three times to eliminate the unbounded dsDNA. The rinsing buffer was collected after each rinsing step in a vial and named "flow through vials" (FTv). Afterwards, a MilliQ water solution was flowed into the channel and a temperature of $95\,°$C was set on the main heater of the SoG device to separate the dsDNA.

The control system is based on the variation of the thin film resistance with temperature. We were able to reach a heater temperature of $105\,°$C in about 15 s, with an average heating rate of $7\,°$C/s and a regime temperature ripple of the order of $\pm\,0.5\,°$C. Indeed COMSOL simulations of the complete, layered structure demonstrated that a heater temperature of $105\,°$C on the backside of the glass sandwich lead to a front temperature of about $95\,°$C. A cooling system was not necessary in this case and was not implemented. The final temperature reached by the heater slightly depends on the room temperature, since the overall 2-wire heater resistance depends on an effective temperature coefficient of resistance, which

encloses the room temperature. However, the temperature control in this module can be implemented in this simple way because the regime heater temperature is not so critical as for the PCR module. Indeed, it is enough to increase the temperature above the melting point of the ds-DNA to achieve the separation. After heating the channel at 95 °C for 30 s, the microchannel was rinsed using MilliQ water at the flow rate of 15 μl/min for 2 min and the heater was turned-off. Finally, the channel was rinsed at the flow rate of 5 μl/min per 6 min and 15 μl/min for 2 min. This procedure was repeated for three times and all the samples were collected in three different vials named "sample vials" (Sv). At the temperature of 95 °C the dsDNA denatures thus separating the complementary sequences. The biotinylated strand remains bound to the PHEMA-streptavidin layer while the other strand is removed by the flow of water applied into the channel. In order to verify this hypothesis, all the FTv and Sv samples were lyophilized, and subsequently the powder was re-dissolved in MilliQ water and analyzed by UV-vis spectroscopy following the absorption at 260 nm.

Fig. 4.15 shows that, as expected, the amount of dsDNA in the FTv samples decreases from the FTv1 to FTv3 after the third rinsing step and that some DNA is still present in FTv3. This result suggests that probably some of the dsDNA remains bound onto the PHEMA-streptavidin layer or non-specifically adsorbed onto the surface of the PDMS channel.
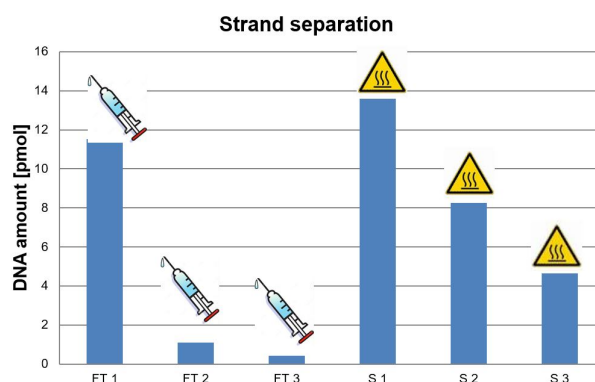
Figure 4.15. Analysis by UV-Vis spectroscopy of FTv and Sv samples.

The analysis of the Sv samples revealed the presence of DNA in each vial, even though the amount of DNA in Sv3 resulted diminished compared to Sv1. In order to verify whether the DNA collected was dsDNA or ssDNA, the two spots of sample were analyzed also by gel-electrophoresis (Fig. 4.16). The analysis revealed that ssDNA was retried by applying the described procedure. This experiment demonstrates the capability of the PHEMA-Streptavidin functionalized chip to separate the dsDNA obtained by PCR.

The advantage of the use of the dsDNA-Chip, relies into the small volumes needed for the separation procedure and on the shorter time required for performing the whole step, after 30 min a dsDNA part is achieved. In standard lab procedure, the streptavidin-coted resin must be separated from its storage solution by filtration or magnetic field and then equilibrated with a suitable buffer. The dsDNA concentrated
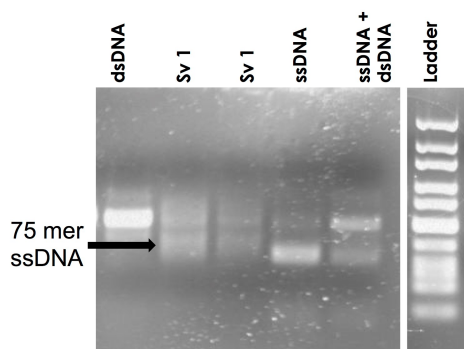
Figure 4.16. Gel-electrophoresis of the Sv1 sample.

solution $> 10\,\mu$M must be applied and, after the chosen incubation time, removed by filtration or other methods. The resin must be then rinsed with buffer at least twice and then the elution of the ssDNA can be accomplished by heating or other denaturing strategies. This multi step discontinuous process takes at least 1 h and large volumes of solutions.

4.4 On-chip aptamers selection

This site has not been developed yet. We are still designing and planning the experiments. However thanks to the collaboration with chemists and biologists, some milestones were fixed. The PDMS microfluidics chamber will have a serpentine shape, similar to that one used for PCR and for the separation site. There is the necessity of a heater to heat up to 95 °C and break the aptamer/target bonds, similar to the one used for the other two sites. For the rest, the chemical part remains to be tested. Recalling the need to have the three different types of selection (positive, negative and competitive), the planning of the experiments is as follows:

1. functionalize the glass with only target (phosphoTyr) and flush a sample with only aptamer, to evaluate the selected aptamer bond toward its target;

2. not functionalize the glass but simply bond the PMDS on it and flush a sample with only aptamer, to evaluate the selected aptamer bond to "non-functionalized" channel;

3. functionalize the glass with only target (phosphoTyr) and flush a sample with the random pool (without the aptamer), to evaluate the binding between the target and all generic oligonucleotides;

4. functionalize the glass with only target (phosphoTyr) and flush a sample with random pool and aptamer, to evaluate the selected aptamer bond toward his target in the presence of potentially "interfering" oligonucleotides;

5. repeat the steps 1-4 substituting the target molecule with a similar one (NitroTyr or Tyr) in order to evaluate the specificity of the procedure;

6. not functionalize the glass but simply bond the PMDS on it and flush a sample with random pool and aptamer, to evaluate the selected aptamer bond to the "non-functionalized" channel in presence of potentially "interfering" oligonucleotides;

7. functionalize the glass with only target (phosphoTyr) and flush buffer solution to evaluate the functionalized material detachment from the channel due to the heat treatment effect;

8. functionalize the glass with a molecule similar to the target (Nitro-Tyr or Tyr) and flush buffer solution to evaluate the functionalized material detachment from the channel due to the heat treatment effect;

9. not functionalize the glass but simply bond the PMDS on it and flush buffer solution to evaluate the functionalized material detachment from the channel due to the heat treatment effect.

4.5 Related Projects

During my PhD I also worked on other projects thanks to collaborations that my Tutor had with other research groups. Here I report a few major works in which I participated and which led to publications on international journals.

4.5.1 Thin film heaters on glass substrate for Lab-on-Chip applications[3]

This work presents a comprehensive procedure for the design and implementation of thin film heaters manufactured on glass substrates. The thermal and electrical behavior of the heaters have first been simulated and proper design solutions have been adopted for increasing the thermal resistance of the heaters, thus decreasing their power consumption. Trenches were adopted in order to thermally isolate the heater from the glass substrate. The presence of four different layouts of trenches on the back and the front side of the glass slide with different geometries was extensively simulated. The simulated geometries were manufactured and an automatic sawing machine was exploited to dig $240\,\mu$m wide trenches in the glass substrate. The trenches were typically stopped at about $80\,\mu$m from the opposite surface. Techniques commonly adopted for measuring the temperature coefficient of resistance, the thermal resistance and thermal capacitance in the case of Si-based microheaters have conveniently been modified to take into account the fundamentally different thermal parameters of a heater manufactured on glass. An experimental improvement of the thermal resistance up to 217% on a heat sink and 30% in air has been obtained when a large part of the thermal mass under the microheater was removed. The thermal capacitance was also considerably decreased, thus improving the dynamic thermal behavior.

---

[3]This paragraph is based on the paper *"Design and experimental characterization of thin film heaters on glass substrate for Lab-on-Chip applications"* Scorzoni, A., et al, Sensors and Actuators A: Physical (2015) [78]

My contribution to this project has been the design and fabrication of the thin film heaters.

4.5.1.1 Design and simulations

Thermoelectric simulations are widely adopted to predict the thermal behavior of micro-electro-mechanical systems. We used Comsol Multiphysics to compare the thermal characteristics (thermal resistance R_{th}, time constant τ, and thermal capacitance C_{th}) of different structures where trenches in the glass substrate have been engraved. We solved the electrostatic problem coupled with the heat transfer problem also considering the temperature dependence of the thin film resistivity. Orthographic projections and top views of the investigated structures are reported in Fig. 4.17.
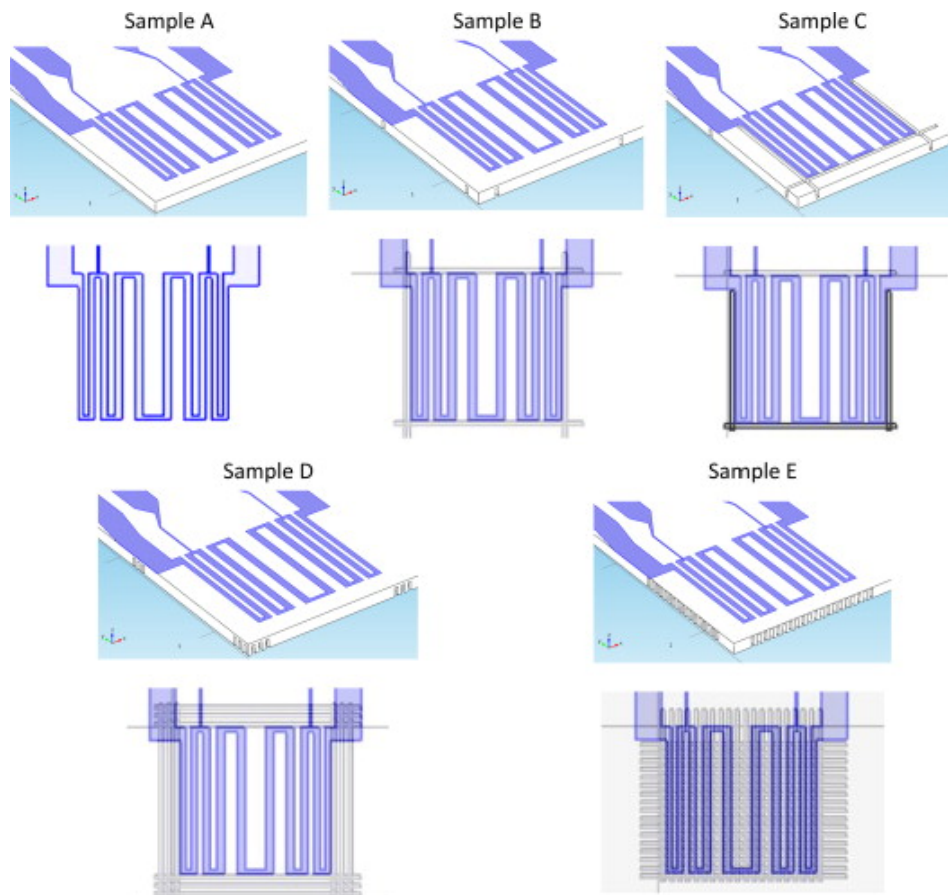
Figure 4.17. Orthographic projection and top view of the simulated structures of thin film heater on glass. Sample A is the reference, sample B has four linear trenches on the glass back side, sample C features three linear trenches on the glass front side and one on the back side, sample D has three concentric rectangular trenches cut on the back side, for a total of twelve linear trenches, while the trenches of sample E shape a chessboard geometry underneath the heater. The chirped serpentine guarantees good temperature uniformity on the whole surface of the microheater, while the pad geometry has been chosen in order to contribute with a low series resistance.

Sample A represents the reference. It is made of a $5\,\text{cm} \times 2.5\,\text{cm} \times 1\,\text{mm}$ glass substrate on top of which a thin film heater was shaped as a chirped serpentine which guarantees a good temperature uniformity on the whole surface of the microheater, in particular between the two voltage taps of its four-terminal geometry. The film is a 300 nm-thick Cr/1500 nm-thick Al/300 nm-thick Cr stacked structure (see next Section for experimental details). In order to optimize the thermal behavior of the whole structure, differently shaped mechanical trenches have been envisaged in the glass bulk around the heater.

For sample B, a rectangular trench is considered on the opposite side with respect to the heater (back side). It is implemented all around the heater at $80\,\mu\text{m}$ distance from the heater edge and it is $240\,\mu\text{m}$ wide and $800\,\mu\text{m}$ deep, i.e. the remaining glass is only $200\,\mu\text{m}$ thick in correspondence with the trench.

Sample C has a trench with the same layout of sample B, but on the same glass side of the heater (front side). However, in order to avoid cutting the metal electrodes, one side of the rectangular trench was implemented on the back side of the glass slide.

Sample D features three concentric rectangular trenches cut on the back side, for a total of twelve linear trenches.

For sample E, chessboard geometry was created to remove a big part of the thermal mass under the heater.

For all the samples C, D and E the trenches have the same width ($240\,\mu\text{m}$) and depth ($920\,\mu\text{m}$), i.e. trenches were stopped at about $80\,\mu\text{m}$ from the opposite surface. The spacing between parallel trenches was $240\,\mu\text{m}$. The minimum distance between the edge of the trench and the outer border of the heater was $80\,\mu\text{m}$.

Simulations take into account the electrical and thermal characteristics of the glass substrate and the metallic resistor. In particular, the glass characteristics have been taken from the COMSOL Multiphysics library. The current flowing in the thin film resistive element and the heat transfer model have been coupled setting the external source of heat flux "Q" equal to the scalar product of the electric field "E" and the current density "J". The heat transfer problem, both in static and dynamic operation, has been modeled considering the heat exchange due to conduction and convection processes and the temperature dependence of the thin film resistivity. The radiation term has been neglected.

Thermal resistance and thermal capacitance have been inferred, respectively, from static and time dependent simulations. Specifically for R_{th} evaluation, the stationary solution of the coupled thermal and electrical problems is considered when the heater of each structure is biased with a constant current. The thermal resistance is calculated from the formula $R_{th-4w} = \Delta T / P_{4w}$, where P_{4w} is the four-terminal power dissipated by the heater, i.e. the voltage–current product where the voltage is calculated between the inner voltage taps of the heater, while ΔT is the difference between the heater active area temperature (evaluated as the aver-age temperature of the metallic film located between the inner voltage taps) and the ambient temperature.

Simulations have been performed considering two limiting cases for the thermal boundary conditions: the structures are either placed in air ("air") simulating pure convective thermal exchange or they are coupled to a thick metal block ("on-plate") that can be considered as an almost ideal metal sink where the thermal exchange

is purely conductive. In all the simulations the convective coefficient h in the heat transfer model has been set to $8\,\mathrm{W/(m^2K)}$. This coefficient, for free convection in air, depends on the orientation of the surface and on surface properties.

The thermal coupling between the glass substrate and the metal block was modeled as a very thin $(75\,\mu\mathrm{m})$ air gap between the two parts.

Figs. 4.18a and b report, as lines, the simulated time evolution of the temperature in air and on-plate, respectively. The table reported in Fig. 4.19 shows the thermal resistances, time constants and thermal capacitances of the five analyzed structures. The thermal time constants have been evaluated by best fit of the achieved simulated curves with an exponential decay.
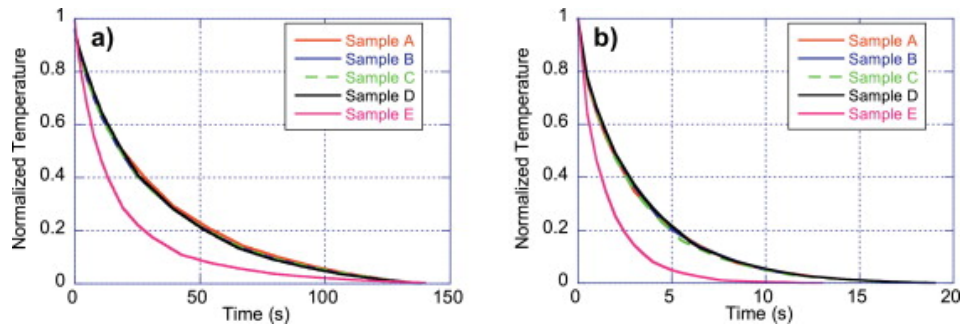
Figure 4.18. Simulated temperature evolution for the different investigated structures: (a) and (b) refer to structure in air and on-plate respectively.

Simulated thermal parameters of the five samples.

Sample		$R_{th\text{-}4w}$ (K/W)	τ (s)	C_{th} (mJ/K)
A	on-plate	49.7	3.145	63.3
	in air	333.6	36.65	109.8
B	on-plate	54.0	3.035	56.2
	in air	370.3	34.1	92.1
C	on-plate	54.3	3.17	58.3
	in air	369.2	34.29	92.9
D	on-plate	55.7	3.23	58.0
	in air	411.5	33.7	81.8
E	on-plate	85.4	1.46	17.2
	in air	505.0	16.9	33.5

Figure 4.19. Simulated thermal parameters of the five samples.

Since the thermal capacitance is a derived quantity $(C_{th} = \tau\,/\,R_{th})$, we mainly focus on the thermal resistance and the time constant. From table a very small thermal resistance increase among samples A–D with varying trench geometry, with a maximum change of thermal resistances of about 12% on-plate and 23% in air. The thermal resistance of samples B and C are roughly identical, therefore drawing trenches on the front side of the glass instead of the back side appears to have a negligible effect. Moreover, a slight correlation is found between a threefold increase of number of trenches (sample D) and the improvement of the thermal resistance. Thermal time constants are approximately the same for samples A, B, C and D, within 2.5%. Only sample E, with chessboard geometry shows a 54% variation of the thermal time constant with respect to the reference sample A, both in air and on-plate. In particular, comparing samples E and A, the thermal resistance shows

a percentage variation of 51% and 72% in air and on plate, respectively. These observations bring us to the preliminary conclusion that the thermal parameters are substantially affected only by a considerable material removal in the glass bulk.

4.5.1.2   Fabrication

A Cr/Al/Cr sandwich has been chosen as heater material for its good adhesion characteristics on glass and for its relatively high temperature coefficient of resistance (TCR_0, calculated at $0\,°C$) of about $4\times10^{-3}\,°C^{-1}$, which guarantees good sensitivity when the heater is also used as a resistance temperature sensor device. The integrated structure has been fabricated on a ultrasonically cleaned glass substrate of $50\,\text{mm} \times 50\,\text{mm} \times 0.75\,\text{mm}$ with the following technological steps:

1. Vacuum evaporation of a $30\,\text{nm}/200\,\text{nm}/30\,\text{nm}$-thick Cr/Al/Cr stacked structure;

2. Definition of the thin film heater by conventional photolitography and wet etching of the metal layers; the device area is $8.5\,\text{mm} \times 8.7\,\text{mm}$, while the distance between the center of the voltage taps and the center of the heater is $3.2\,\text{mm}$;

3. Annealing of the metallization at $120\,°C$ for 3h on a hot plate. This final process is carried out at a temperature greater than the maximum temperature usually reached by the thin film heater, but lower than the maximum temperature that the glass can withstand. The main goal is to stabilize the microstructure of the metal film in order to avoid hysteresis during repetitive temperature sweeps. In fact, without the final annealing step we found the TCR_0 of the Cr/Al/Cr structure changed even after a single temperature sweep from ambient temperature to $100\,°C$. Instead, after the annealing step the stability of the TCR_0 was ascertained after 5 temperature sweeps.

Devices underwent an additional procedure dedicated to the fabrication of trenches on the back side and/or the front side of the glass. Trenches, featuring a width of $240\,\mu\text{m}$, were dug by means of a semi-automatic sawing machine ADT 7100 Series–Vectus. The same trench geometries previously described were experimentally fabricated on the microheaters. The fabricated structures are shown in Fig. 4.20. We initially characterized the reliability of this process on glass slides and found that the maximum remaining thickness obtainable with a sewing machine is about $80\mu m$ from the opposite surface. If this remaining thickness is decreased down to $50\,\mu\text{m}$ the samples are very fragile and tend to develop cracks after just one thermal cycle. The sawing process was performed without dedicated markers for automatic alignment of the sample.

4.5.1.3   Experimental Result

Accurate 4-wire measurements and thermal characterization of the microheaters were accomplished. In this case the heater on glass is kept in direct contact with the hot plate using thermally conductive paste and kapton tape. Measured parameters were the TCR_0, the four-wire thermal resistance R_{th-4w} and the thermal capacitance C_{th}.
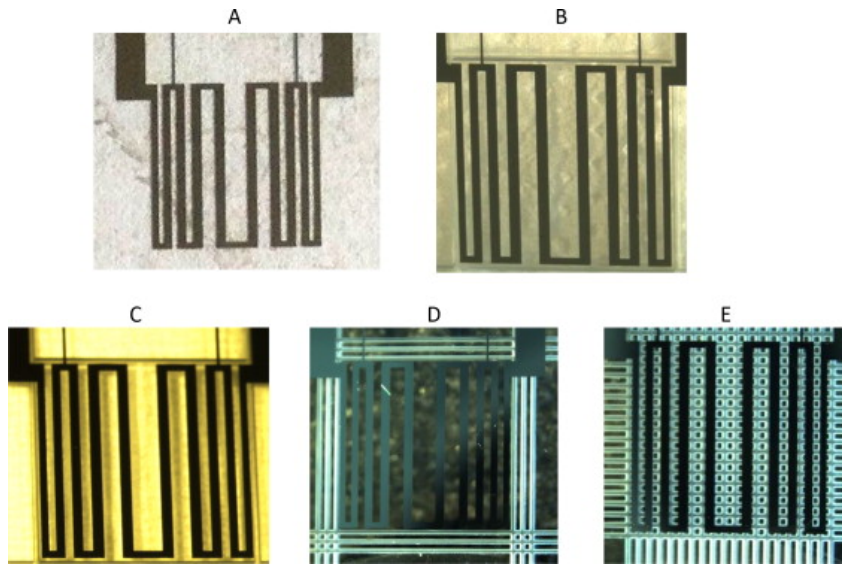
Figure 4.20. Micrographs of the manufactured samples. For sample E a micrograph of the back side highlights the trench geometry.

The first measurement regards the TCR_0 and it has been performed by defining different temperature steps during which the 4-wire electrical resistance R_{4w} is measured as a function of the hotplate (and active area) temperature T: $R_{4w} = R_{0-4w}(1 + TCR_0 T)$, where where R_{0-4w} is the electrical resistance at $0\,°C$. Fig. 4.21 shows the measured curves for all the previously described samples.
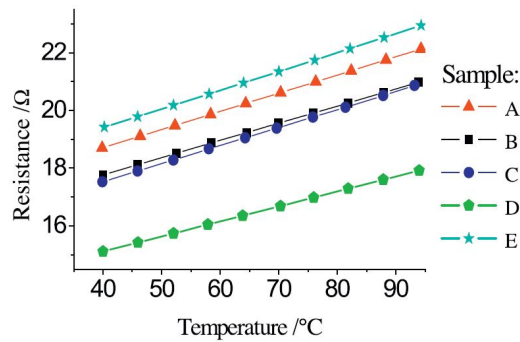
Figure 4.21. Heater (and hot plate) temperature as a function of heater 4-wire resistance R_{4w}.

As expected, the resistance varies linearly with the temperature and therefore the thermal coefficients of resistance TCR_0 can be derived. They are reported in table in Fig. 4.22 for the different structures, showing a percentage variation around 7%. This difference is partly due to the measurement experimental error and partly to the batch to batch deposition repeatability. The R_{4w} vs. T curves will be used in the next phase for extracting the heater temperature from the measured heater resistance value.

The thermal resistance and the thermal capacitance have been evaluated when the

Comparison of the experimental thermal parameters of the five samples.

Sample		TCR_0 ($^\circ C^{-1}$)	$R_{\text{th-4w}}$ (K/W)	$Power_{4w}$ (W) @ 94°C	τ (s)	C_{th} (mJ/K)	R^2
A (ref.)	on-plate	3.82×10^{-3}	32.4	2.901	1.677 ± 0.017	52	0.9991
	in air		269.8	0.348	35.21 ± 0.33	131	0.9979
B	on-plate	3.86×10^{-3}	52.3	1.797	3.59 ± 0.01	69	0.99998
	in air		312.9	0.300	34.44 ± 0.23	110	0.9989
C	on-plate	4.16×10^{-3}	35.6	1.574	1.9334 ± 0.005	54	0.99993
	in air		288.0	0.201	35.86 ± 0.37	125	0.9988
D	on-plate	3.98×10^{-3}	54.5	1.0819	3.383 ± 0.001	62	0.99999
	in air		338.0	0.1734	36.09 ± 0.09	107	0.9993
E	on-plate	3.88×10^{-3}	102.9	0.5720	2.643 ± 0.001	26	0.99998
	in air		348.1	0.1583	17.45 ± 0.08	50	0.99671

Figure 4.22. Heater (and hot plate) temperature as a function of heater 4-wire resistance R_{4w}.

glass substrate is in air or in thermal contact with a metal block. In both cases, the heaters are initially biased with a constant current. When thermal equilibrium has been reached, the thermal resistance is extracted with the same procedure utilized to extract the simulated thermal resistance, i.e. from the formula $R_{th-4w} = \Delta T / P_{4w}$, where the parameters have previously been defined. Once the heater reaches thermal equilibrium, the heating current is turned off and the heater resistance is monitored injecting a small bias current through the external electrical pads and measuring the voltage across the internal pads. Taking into account the results of Fig. 4.21, the heater temperature can be derived. This procedure is the same implemented in the simulations to monitor the average temperature across the heater.

Thermal time constants were calculated by fitting the measured temperature time dependencies for all samples with the glass substrate placed both on a metal plate and in air. The fitting curve is a simple exponential $T(t) - T_a = Ae^{-t/\tau}$, where the time constant is $\tau = R_{th-4w}C_{th}$. Fig. 4.23 shows the temperature decay of the sample E as an example of temperature behavior as a function of time. In particular, Figs. 4.23(a) and (b) show the measured points and the fitting curves for the time evolution of the temperature on-plate and in air, respectively.
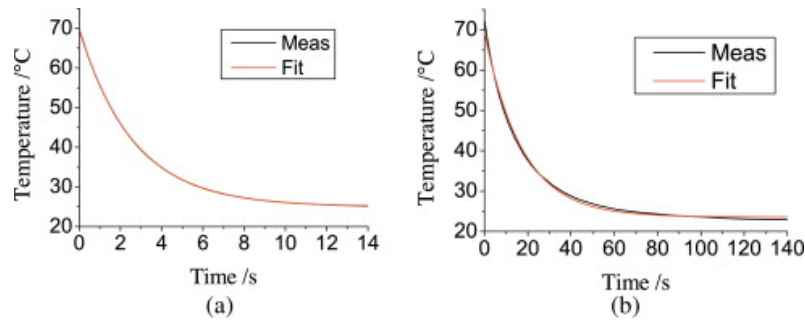
Figure 4.23. Temperature decay of sample E (a) in thermal contact with the plate at ambient temperature; (b) in air. The measured points have been acquired with a sampling rate of 20 ms, for this reason the measured curves look continuous.

The preliminary conclusion depicted in simulation paragraph, i.e. that the thermal parameters are substantially affected only by a considerable material removal in the glass bulk, is confirmed by the experimental results summarized in these figures. The geometry of trenches, which maximizes the effect on thermal parameters,

is the chessboard geometry, where, as expected, the removal of a big part of the thermal mass has a considerable effect both on the increase of thermal resistance and the decrease of the thermal capacitance. In particular, the time constant shows a percentage variation of 50% and 58% in air and on-plate, respectively, as well as the thermal resistance shows a percentage variation of 30% and 217% in air and on-plate, respectively.

We observe that the simulated and experimental time constants show a reasonable agreement, whereas the simulated and experimental thermal resistances mainly disagree in the "on-plate" scenario. In fact, the "on-plate" thermal resistance is strongly dependent on the thermal contact between the glass and the metal plate, which is very difficult to reproduce among different samples, being strongly dependent on the pressure of the glass plate on the metal thermal sink or on the quality or flatness of the glass/plate interface. In our simulation we modeled the thermal contact between the glass and the metal plate with a $75\,\mu$m thick air gap and we realized that the thickness of this air gap has a major effect on the thermal resistance. Taking into account that no fitting procedures have been performed in the simulations, we conclude there is a reasonable agreement between modeling and experiments, showing the implementation of a successful experimental approach to improve the thermal performance of a thin film heater on glass substrate for LoC applications.

4.5.2   On-chip detection of celiac disease epitopes[4]

This work presents a lab-on-chip system combining a glass-polydimethilsiloxane microfluidic network and an array of amorphous silicon photosensors for the diagnosis and follow-up of Celiac disease. The microfluidic chip implements an on-chip enzyme-linked immunosorbent assay (ELISA), relying on a sandwich immunoassay between antibodies against gliadin peptides (GPs) and a secondary antibody marked with horseradish peroxidase (Ig-HRP). This enzyme catalyzes a chemiluminescent reaction, whose light intensity is detected by the amorphous silicon photosensors and transduced into an electrical signal that can be processed to recognize the presence of antibodies against GPs in the serum of people affected by Celiac syndrome. The correct operation of the developed lab-on-chip has been demonstrated using rabbit serum in the microfluidic ELISA. In particular, optimizing the dilution factors of both sera and Ig-HRP samples in the flowing solutions, the specific and non-specific antibodies against GPs can be successfully distinguished, showing the suitability of the presented device to effectively screen celiac disease epitopes.
My contribution to this project has been the fabrication and characterization of the glass hosting the array of a-Si:H photosensors for the on-chip analysis and the microfluidic network fabrication.

---

[4]This paragraph is based on the paper *"Lab-on-chip system combining a microfluidic-ELISA with an array of amorphous silicon photosensors for the detection of celiac disease epitopes"* Costantini, F., et al., Sensing and Bio-Sensing Research (2015)[15]

4.5.2.1 Celiac disease

Celiac disease (CD) is a chronic inflammatory disease of the small intestine that affects genetically susceptible individuals. It is a chronic disorder caused by dietary gluten in genetically susceptible individuals characterized by an inappropriate immune response against some peptides of gluten (CD epitopes). A number of about 30 deamidated gluten peptides have been identified as the most common CD epitopes, which can be used as biomarkers of CD. Thus, different individuals are sensitive to a different subset of CD epitopes and therefore a patient specific fingerprinting could have both a diagnostic value and therapeutic impact. Lab-on-chip devices appear excellent candidates for such screening.

4.5.2.2 Experimental

The microfluidic chip includes (i) a $4 \times 4 \, \text{cm}^2$ glass substrate covered with PHEMA brush layer functionalized with succinic anhydride (SA) and a PDMS microfluidic network bonded together.

The microfluidic network ($4 \times 4 \, \text{cm}^2$) consists of 4 parallel channels ($1500 \, \mu\text{m}$ width $\times \, 50 \, \mu\text{m}$ depth $\times \, 2.85 \, \text{cm}$ length) having separate inlets and outlets. The mold for the PDMS channels was fabricated by standard photolithography using SU-8 2050 (Microchem) on silicon wafers, with a final thickness of $\approx 50 \, \mu\text{m}$, following the recommended procedure by the manufacturer. In order to fabricate the microfluidic channels, PDMS components were combined in specific ratios (1:10 curing agent and base material) and cured at specified conditions, as reported in par. 3.2.1. This PDMS slab was removed from the mold and it was then bonded to the glass slide previously functionalized with PHEMA-SA, using the transfer bonding technique with uncured PDMS as the adhesive. CD epitopes are then immobilized inside the channels and, subsequently, solutions containing primary antibodies towards CD epitopes and secondary antibody marked with enzyme Horseradish Peroxidase (Ig-HRP) are flowed through the microfluidic channels.

A qualitative description of the microchannel inside, during this analytical procedure, is reported in Fig. 4.24.
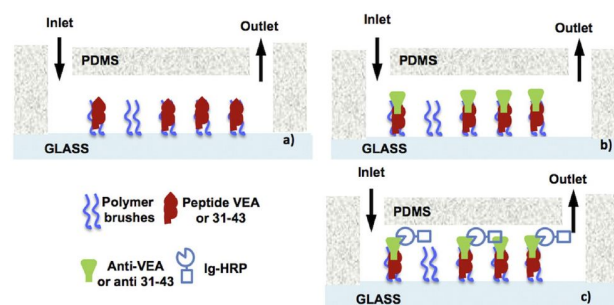
Figure 4.24. Functionalization of the microchannels with a) gliadin peptides (VEA or 31-43), b) anti-VEA or anti-31-43 rabbit antisera and c) secondary anti-rabbit antibody marked with HRP.

Briefly, in this work we introduced a microfluidic-ELISA based on GPs functionalized microfluidic network, to overcome the issues deriving from the sample handling,

combined with the array of a:Si-H photosensors for the detection of the chemilumine-scent signal deriving from the interaction of GPs with the specific antibody. The lab on chip was designed to have an array of 30 a-Si:H photosensors deposited on a glass substrate (Fig. 4.25). The photosensors are organized as a 5×6 matrix. All
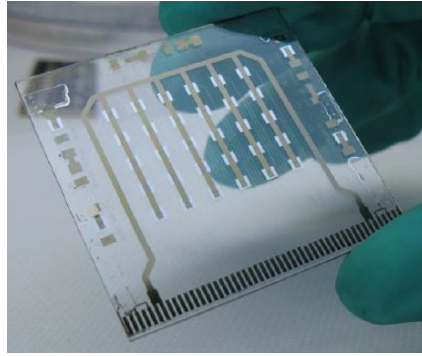
Figure 4.25. Fabricated chip for the analysis.

the n-type a-Si:H layers of the photodiodes are connected together by the metal top electrode, which includes the six brown vertical lines and the brown C-shaped geometry. Each p-type a-Si:H layer is instead connected to its own electrical contact, which is individually brought to the edge of the glass substrate for the connection to the read-out electronics. These individual connections are not visible because they are made in ITO. Indeed, the ITO used in this work presents a resistivity equal to $3.25 \cdot 10^{-4} \, \Omega/\text{cm}$ and a transmittance greater than 80% for wavelength above 420 nm. This last result is particularly important because, since the peak emission spectra of the HRP occurs 425 nm, it ensures that mostly part of the chemiluminescence radiation passes unabsorbed through the ITO layer. The photosensors are fabricated with the technological processes described in par. 2.2.3. In particular the fabrication was performed through the following steps:

1. deposition and pattering by photolithography of the ITO window layer for the definition of the front electrode of the photodiodes;

2. deposition by PECVD of the a-Si:H layers;

3. deposition by evaporation of Cr layer, which acts as back electrode of the sensors;

4. mesa patterning of the device structure by wet and reactive ion etching (R.I.E.) for the metal stack and a-Si:H layers respectively;

5. deposition and patterning for via hole definition of a $5 \, \mu\text{m}$-thick SU-8 layer acting as insulation layer between the back metal and the front ITO contacts;

6. deposition by evaporation of a stack of three metal layers (Cr/Al/Cr) for the definition of external connection of the photodiodes;

7. patterning of the metal layers (Cr/Al/Cr) external contacts by photolithography.

We found that the current-voltage characteristics of the photosensors are quite uniform over the all the array. The current density J measured in dark condition in the small reverse voltage region (below $+100\,\text{mV}$ applied to the n-region) shows a value around $10^{-11}\,\text{A/cm}^2$. From the quantum efficiency measurements, we found that the quantum yield at $425\,\text{nm}$ is equal to 0.28 with a corresponding responsivity of $100\,\text{mA/W}$.

A functionalized microfluidic chip, having four parallel channels is aligned with the array of photosensors, which serves for the detection of the chemiluminescent signal deriving from the immunoassay occurring in the microfluidic chip. The microfluidic chip is functionalized with PHEMA polymer brushes. Briefly, PHEMA is grown on a glass substrate and functionalized with succinic anhydride to obtain carboxylic functional groups on the brush layer (PHEMA-SA). The glass substrate is then bonded with the array of four parallel channels made in polidimethylsiloxane PDMS. In each channel is flowed a water solution containing NHS-EDC and this solution kept inside for 1h. After rinsing with purified water, a different peptide is flowed in each channel and left inside over night at $4\,°\text{C}$. Finally the channels are rinsed out using purified water.

The microfluidic device was aligned on the array of photosensors and inserted in the base of a small box ($6 \times 8 \times 12\,\text{cm}^3$) containing the electronic read-out and the microfluidic tubes (Fig. 4.26). Each channel has separated inlet and outlet for liquid handling. Holes drilled in the lid of the box (partially shown in the figure) allow the microfluidic connection to a peristaltic pump to perform the immunoassay and at the same time shielding of the photosensors from the ambient radiation.
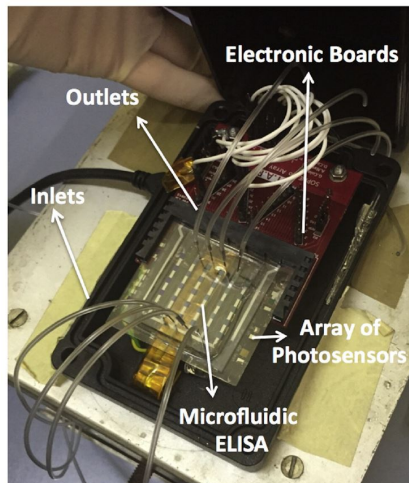
Figure 4.26. Picture of the inside of the box containing the electronic read-out board, the photosensor array, the microfluidic chip and the microfluidic connections needed to perform the ELISA. The lid hosts the holes for the microfluidic connections and permits a shielding of the ambient light.

As a proof of principle, for each microfluidic chip, we functionalized two channels with the GPs named VEA and two channels with 31-43 (see Fig. 4.24a). Reaction buffer solution of Rabbit sera containing primary antibodies against VEA (anti-VEA) or 31-43 (anti-31-43) (see Fig. 4.24b) were flowed into the four parallel channels

with the following scheme:

- a reaction buffer solution containing anti-VEA was flowed into the channel functionalized only with VEA;

- a reaction buffer solution containing anti-31-43 was flowed into the channel functionalized only with GP 31-43;

- a reaction buffer solution contain anti-VEA was flowed into the channel functionalized only with GP 31-43;

- reaction buffer solution without rabbit sera was flowed into the channel functionalized only with peptide VEA (peptide-only).

Subsequently, in each channel was flowed a solution of a secondary antibody labeled with HRP (Ig-HRP) and incubated for 10 min (see Fig. 4.24c).

4.5.2.3 Results

In the immunoassay analysis, a chemiluminescent (CK) cocktail based on luminol and hydrogen peroxide (H_2O_2) is flowed into the channels. The HRP catalyzes the oxidation of luminol by H_2O_2, yielding a chemiluminescent signal, which is detected by the photodiodes and read-out by the electronic board. In a typical experiment, the photocurrent signal detected by the photosensors increases, reaches a peak whose value depends on the type of interaction and then decreases.

This behavior is illustrated in Fig. 4.27, which reports the results obtained using reaction buffer solutions of rabbit antisera and Ig-HRP diluted 500 and 200 times, respectively. We observe that the photocurrent signal originated by the interaction between a GP and its specific antibody (i.e. GP with its specific rabbit antiserum) is always higher than that detected when the same GP reacts with the nonspecific rabbit antisera or when no antisera is flowed in to the functionalized channel. This implies that the LoC system can be successfully used to screen the antibodies in the serum.

The optimized dilution conditions for both rabbit sera and Ig-HRP were also investigated. In particular, reaction buffer solutions of rabbit sera were prepared diluting the serum between 50-500 times and the standard solution of Ig-HRP between 200-2000 times finding that the optimized buffer dilutions are 500 and 2000 for the rabbit antisera and Ig-HRP, respectively.

As a final remark, we would like to note that the total time of analysis, once the microfluidic chip has been functionalized with PHEMA-SA, is around one hour. This time includes the analytical procedure and the analysis with the array of a-Si:H photosensors. Therefore, the presented lab-on-chip system requires half of the time that is usually necessary for an ELISA analysis.
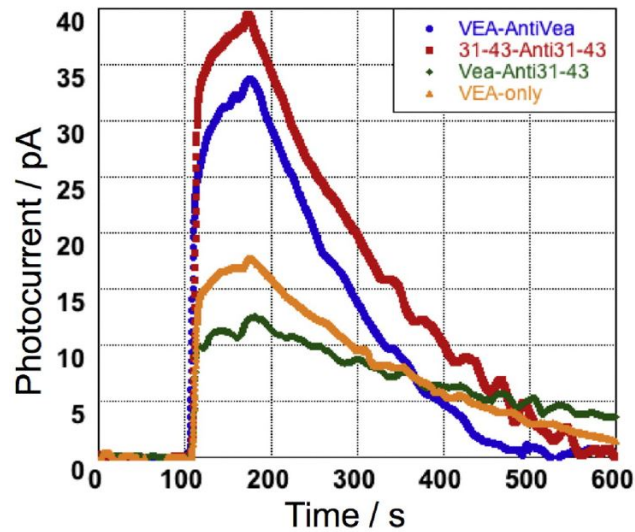
Figure 4.27. Photocurrent signal versus time obtained by flowing the CK cocktail into the microchannels functionalized with rabbit antisera and Ig-HRP diluted 500 and 200 times, respectively.

4.5.3   On-chip detection of Ochratoxin A by aptamer-based sandwich assay[5]

This work presents a multichannel glass-PDMS microfluidic chip functionalized with a novel aptasensor for the detection of *Ochratoxin A (OTA)*. The aptasensor is built on a glass substrate covered with a polymer brush layer subsequently functionalized with an aptamer having high affinity towards OTA. The assay relies on an aptamer-linked immobilized sorbent assay (ALISA) using two different OTA aptamers, which, in presence of OTA, assemble to form a sandwich-like structure generating a chemiluminescent signal. The chip is combined with an array of amorphous silicon photosensors that transduce the chemiluminescent signal into an electrical signal that can be processed to detect and quantify the OTA in the sample. The successful detection of OTA has been demonstrated in standard solutions and in beer samples spiked with OTA. The results show that the values measured for OTA, applying the ALISA assay, are comparable to those measured by the reference methods.
My contribution to this project has been the fabrication and characterization of the array of a-Si:H photosensors and the microfluidic network fabrication.

4.5.3.1   What is OTA?

Ochratoxin A (OTA) is a mycotoxin produced by various Aspergillus and Penicillium strains, which are natural opportunistic biodeterioration agents and is one of the most common mycotoxins contaminating feed and foodstuffs [25]. Upon

---

[5]This paragraph is based on the paper *"Aptamer-Based Sandwich Assay for on Chip detection of Ochratoxin A by an Array of Amorphous Silicon Photosensors"* Costantini, F., et al., Sensors and Actuators B: Chemical (2016)[17]

ingestion, OTA has a number of acute and chronic effects. OTA is widely found in cereals such as corn, wheat, barley, oats and cereals-derived products such as flour, beer and vodka. OTA has been found also in wine, coffee beans, cocoa and dried fruits and spices throughout the world and in animal feed, so that OTA has been traced also in meat and milk.

Due to the European regulation about the limits of OTA concentration in food and feedstuffs, a selective and sensitive method for OTA detection is required in order to guarantee food and feed safety and minimize the risk for human and environmental health. OTA is generally determined by chromatographic techniques such as HPLC (high performance liquid chromatography) and TLC (thin layer chromatography). Other techniques exist for the detection of OTA and among those, ELISA (enzyme linked immunosorbent assay) is very popular due to its relatively low cost and easy application. ELISA is based on molecular recognition by target specific antibodies. ELISA kits for OTA detection are also commercially available. Some of these techniques need sophisticated bulky equipment and trained personnel. Thus, they are not suitable for an initial screening in the field. In this context, research has been focused on the possible miniaturization of the detection methods, which is based on LoC systems, essentially ensuring the portability of the analytical instrument and possible analysis in the field. Indeed as OTA is widespread food contaminant, the demand for fast, inexpensive, selective, and sensitive detection methods has been growing. In particular, systems for rapid screening of samples for the early identification of OTA are needed to trigger further analysis at the accredited laboratory in case of suspected contamination.

4.5.3.2 Results and discussion

The inner of the microchannels is functionalized with Poly(2-hydroxyethtyl methacrylate) (PHEMA) polymer brushes which are chemically activated to immobilize the aptamer 1.12.2 having high affinity versus OTA. Solutions with different concentra- tion of OTA are introduced in the microchannel and captured by the immobilized aptamers. Subsequently, a solution of aptamer A08 labelled with biotin is flowed into the channels to interact with the already immobilized aptamers 1.12.2. A solution of avidin labelled with the enzyme horseradish peroxidase (avidin-HRP) and a solution of luminol and hydrogen peroxide are then flowed to generate a chemiluminescent signal, which induces a photocurrent proportional to the light intensity, in the amorphous silicon photosensors (see the schematic representation in Fig. 4.28).
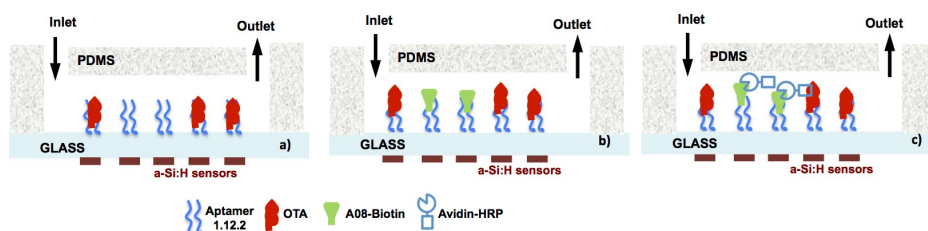
Figure 4.28. Schematic representation of the Enzyme Linked Aptamer Assay (ELAA) surface chemistry in the presented LoC system.

In particular PHEMA polymer brush layer was grown on a glass substrate $4 \times 4 \, \text{cm}^2$ and functionalized with succinic anhydride (SA), in order to obtain PHEMA-SA layer. The device ($5 \times 5 \, \text{cm}^2$) consists of 6 parallel channels ($1500 \, \mu\text{m}$ width $\times \, 50 \, \mu\text{m}$ depth $\times \, 2.85 \, \text{cm}$ length) having separate inlets and outlets. The mold for the PDMS channels was fabricated by standard photolithography using SU-8 2050 (Microchem) on silicon wafers, with a final thickness of $\approx 50 \, \mu\text{m}$, following the recommended procedure by the manufacturer. In order to fabricate the microfluidic channels, PDMS components were combined in specific ratios (1:10 curing agent and base material) and cured at specified conditions, as reported in par. 3.2.1. This PDMS slab was removed from the mold and it was bonded to the glass slide previously functionalized with PHEMA-SA, using the transfer bonding technique with uncured PDMS as the adhesive. Each microfluidic channel was then functionalized with OTA aptamer Amino-1.12.2 and solutions of OTA at different concentration (1-10 mg/l) were prepared. For the fluorescence microscopy study, $20 \, \mu\text{l}$ of each OTA solution (1-10 mg/l) were incubated with the patterned PHEMA-aptamer lines varying the incubation time (10-40 min). After incubation with OTA the patterned lines were rinsed and dried with a stream of nitrogen. The natural fluorescence of OTA (excitation 330 nm and emission 465 nm) was observed using the fluorescence microscope.
This chip was positioned on the array of photosensors connected with a house-made electronic read out system, all closed in a small box, equipped with holes to allow microfluidic connection.

Several preliminary tests have been done to demonstrate the correct operation of each chemical step: the formation of PHEMA pattern, the immobilization of the aptamer Amino-1.12.2 on the functionalized PHEMA and the effectively PHEMA-aptamer film/ mycotoxin bonding.
In order to investigate the binding of OTA to the aptasensors constituted by the PHEMA-aptamer brush film, several patterned PHEMA-aptamer films were first prepared on simple glass substrates. A solution of OTA in test buffer ($20 \, \mu\text{l}$) at different concentrations ($1 - 10 \, \text{mg/l}$) were spotted on the patterned film and incubated for different times. Subsequently, the PHEMA-aptamer layer was analyzed by fluorescence microscopy by observing the natural fluorescence of OTA. The analysis of the patterned PHEMA-aptamer revealed the presence of a fluorescence signal after only 10 min incubation time for all the concentrations applied (Fig. 4.29).

Furthermore with the scope of evaluating the possible interference of other mycotoxins to the binding between OTA and PHEMA-aptamer film, Ochratoxin B (OTA B) and Aflatoxin B1 (AFB1), both at the concentration of 2 mg/l, were incubated for 10 min with patterns of PHEMA-aptamer. The analysis of the patterns did not show any fluorescence signal, proving the selectivity of the PHEMA-aptamer towards OTA. The stability of the aptasensor has also been tested. In particular, we incubated OTA with the aptamer-PHEMA layer and after rinsing we measured the intensity fluorescence signal by using the microscope. Afterwards, the sample was stored for one week in the fridge and the fluorescent intensity measured again. We found about the same value of the fluorescence signal.
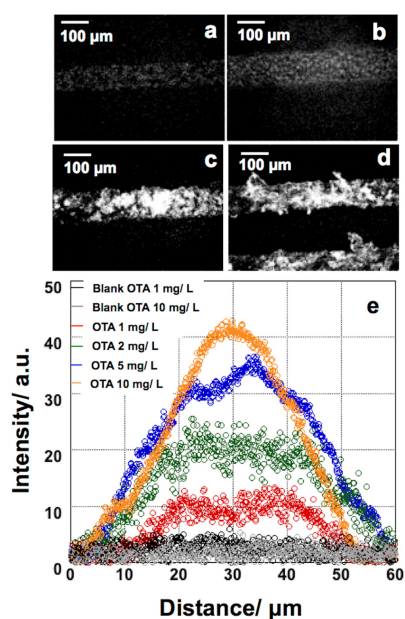
Figure 4.29. Example images of patterned PHEMA-aptamer incubated for 10 min with OTA: a) 1 mg/l, b) 2 mg/l, c) 5 mg/l and d) 10 mg/l and e) plot of fluorescent intensity versus distance obtained from the analysis of the same images.

In particular, for OTA analysis we selected an aptamer-linked immobilized sorbent assay (ALISA) method for the detection of OTA. ALISA relies on the formation of a sandwich-like structure between the target and two target-related aptamers. One aptamer is bound to the PHEMA brush layer (capture probe) to capture OTA from the sample solution and the second is an aptamer biotin-labeled (reporter probe), which would form a complex with OTA upon its binding to the first aptamer (Fig. 4.28). The subsequent use of avidin-labeled with Horseradish Peroxidase (avidin-HRP) would give a chemiluminescent signal after binding the biotin, in presence of luminol and hydrogen peroxide (H_2O_2). The chemiluminescent signal indicates that the immobilization of OTA into the PHEMA-aptamer film occurred, and its intensity is related to the amount of OTA captured inside the channel. The signal is detected by an array of amorphous silicon photosensors (a-Si:H) positioned under the microfluidic chip, whose microchannels are aligned with the columns of the array. In this way, the chemiluminescent light is absorbed by the a-Si:H photosensors which in turn generate a photocurrent proportional to the light intensity. The use of chemiluminescence instead of using the natural florescence of OTA permits the device to function without an external light source, improving its portability and eventually allowing the assay to be extended to other mycotoxins. The photosensors are organized in a 5 array fabricated on a $5 \times 5 \, cm^2$ glass substrate. A picture of the fabricated device is reported in Fig. 4.25. Each element of the array is a two terminal p-type/intrinsic/n-type stacked structure. Taking into account the distance between the microfluidic channel and the photosensors as well as the width of the microchannels, the area of the diode has been chosen equal to $2 \, mm^2$ as a tradeoff between the maximization of the chemiluminescent signal collection and minimization of the cross-talk between different photosensor columns.

The array of microchannels were positioned on the top of the array of a-Si:H photosensors connected to an electronic board (Fig. 4.30) and the chemiluminescent substrate containing hydrogen peroxide and luminol was flowed into the device at the flow rate of $50\,\mu$l/min for 2 min to ensure the complete filling of the microfluidic channels. Subsequently, the pump was stopped and the chemiluminescent reaction was monitored by the a-Si:H photodiodes in stop flow condition.
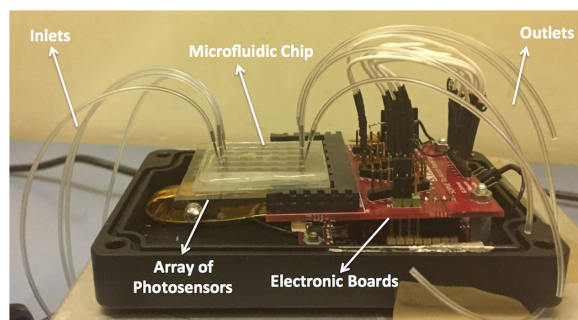
Figure 4.30. Set-up of photosensors integrated with the functionalized microfluidic chip.

Fig. 4.31 shows the results of a typical experiment. After flowing the chemiluminescent substrate, in a few minutes, the photocurrent increases up to a maximum value, which is proportional to the concentration of OTA, and subsequently the signal slowly decreases due to the consumption of the chemiluminescent substrate by the HRP. Moreover, the rapid response of this device is noteworthy. Indeed, within 4 min it was possible to detect the chemiluminescent signal related to the presence of OTA in solution.
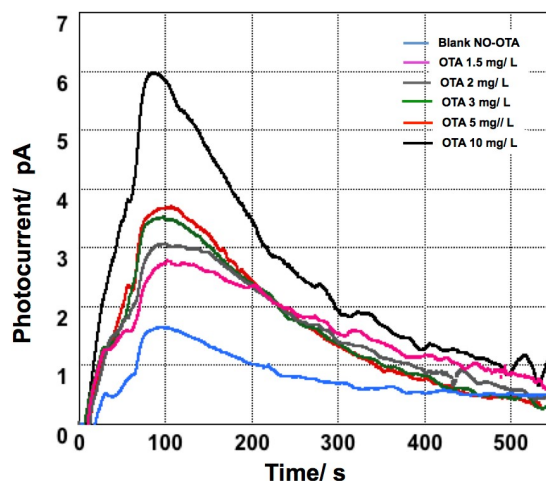
Figure 4.31. Plot of photocurrent intensity versus time.

From the experimental results, achieved flowing different concentration of OTA in the microfluidic channels, we found that the sensitivity of this analytical method is $0.32\,$pAl/mg, while LOD and LOQ are equal to 0.82 and $2.5\,$mg/l, respectively. We also performed experiments using beer sample fortified with OTA. The results

indicate that the system response is quantitatively comparable with those of standard commercial methods. The obtained results establish the development of a novel polymer brush material having high stability and specificity for binding OTA.

A more complete analysis campaign on the validation of the presented method has to be performed, however these preliminary results demonstrate the suitability of the presented assay to successfully detect OTA in complex matrices such as food commodities.

Chapter 5

Towards SELEX chip

In this chapter, taking into account results shown in Chapter 4, I will discuss my final chip design, since the final attempt is the integration of the different modules on a single glass substrate to achieve the on-chip SELEX.

5.1 New SELEX chip design

A first simplification was introduced thanks to the collaborations with chemists and biologists. Indeed one of the most critical steps in the SELEX procedure is obtaining single stranded DNA after the PCR amplification step. This will serve as input for the next cycle so it is of vital importance that all the DNA is single stranded and as little as possible is lost. As reported in par. 4.3, a first attempt has been done using the streptavidin/biontin bond. Nevertheless it is very difficult to break without damaging other polymers or other structures on the glass. Therefore, it is not possible to use the same site more than once, and a number of sites equal to the SELEX cycles is necessary. For this reason we gave up this idea, too difficult to implement on a compact chip, and we considered the possibility to use the exonuclease. Enzymatic degradation of the unwanted strand can be performed by tagging this strand using a phosphate-probed primer, as it is recognized by enzymes such as exonuclease [93]. Exonucleases are enzymes that work by cleaving nucleotides one at a time from the end (exo) of a polynucleotide chain. A hydrolyzing reaction that breaks phosphodiester bonds at either the 3' or the 5' end occurs. In this way the action of the enzyme can progress to complete chain digestion (see Fig. 5.1).
The new chip design will include: a site for the PCR amplification, with heaters and temperature sensors (to monitor the different temperatures necessary during the thermal cycles) and light sensors (for a real-time quantification of the amount of amplified DNA), a site in which the amplified sample will be mixed with exonuclease and a site for the aptamers selection, which is also equipped with a heater to reach the denaturation temperature and with temperature sensors to monitor the achieved temperature. In the device the possibility to use trigger valve is also considered. A trigger valve stops the flow of a first liquid at a point until it is triggered by the flow of a second liquid entering through a second conduit. An image of a trigger valve operation principle is shown in Fig. 5.2.
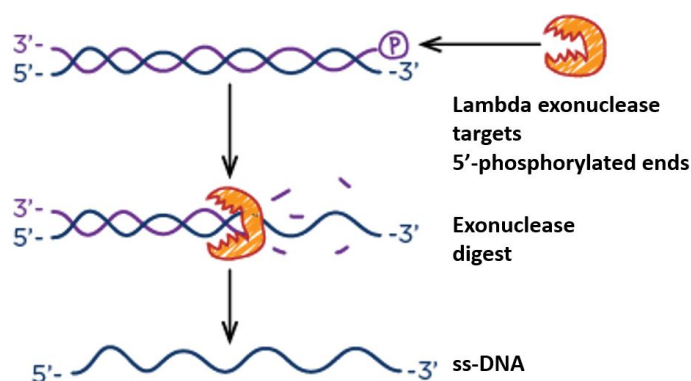
Figure 5.1. Schematic exonuclease activity.
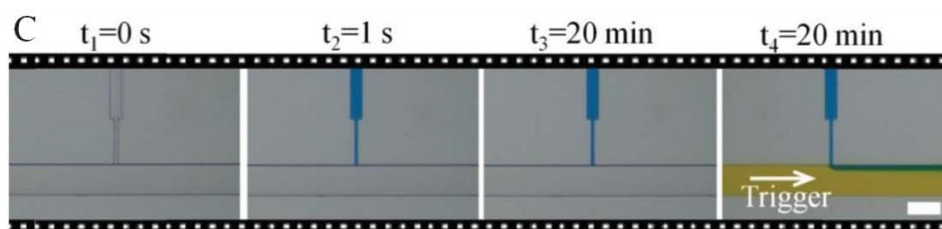
Figure 5.2. Trigger valve working principle.

A second simplification was introduced choosing the pneumatic valves to stop the fluid. Since our purpose is to realize a more compact and complete chip, it became impossible to limit the temperature influence caused by the high number of thermo-actuated valves on the device. For this reason it was introduced the initial possibility to connect the chip to a compressed air line in such a way to use the pneumatic valves.

A first chip design is shown in Fig. 5.3. In red the microfluidic network is reported, in grey the heater, in magenta the pneumatic valves, in blue the bottom metal contact of the sensors, in white the mesa, in orange the SU-8 via holes and in green the top metal contact.

The position of the single module for sensors and heater is similar to the precisely designed for DARWIN'S (Sec. 2.1). Just as an example for the working principle of the next systems, I will describe the different modules and their relative connections. The PCR site has remained virtually unchanged, with the only exception of pneumatic valves (shown in magenta in the Fig. 5.3). The sample is then inserted from the inlet and it's pushed by an external syringe pump into the PCR chamber. The pneumatic valves are activated to confine the fluid within the chamber and it is possible to start the thermal cycles necessary for the PCR amplification. At the end, the valves are opened and the fluid can be pushed toward the next site. Passing near the trigger valve connected to an exonuclease reservoir, mixed fluids continue toward the site where the ds-DNA will turn to ss-DNA. Subsequently the sample is pushed towards the site for selection of aptamers. Initially, the ss-DNA will bind to the
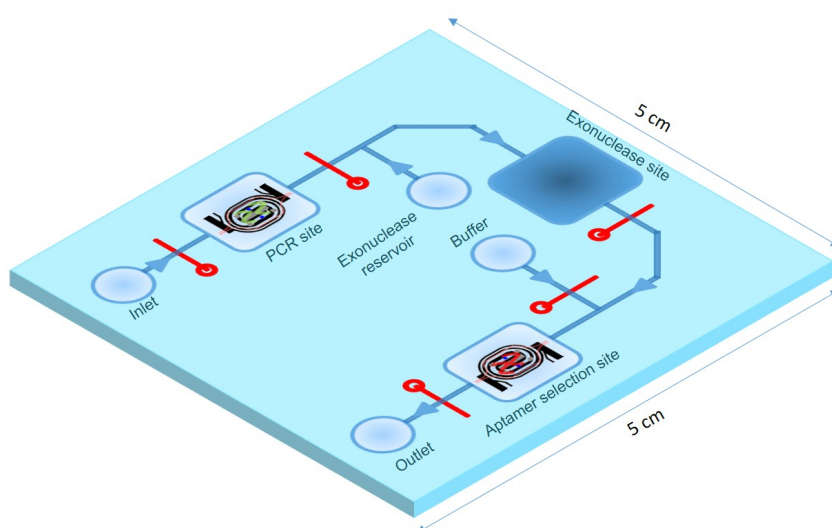
Figure 5.3. New chip designed for one SELEX cycle.

complementary target immobilized on the surface and the not bound oligonucleotides will be washed away by a buffer solution inserted from the outside. Then it's possible to activate the heater to break the aptamer/target bonds and continue to push to collect the selected aptamers. The biggest limit of this configuration is that it's impossible to implement a second SELEX cycle using an external pump, unless the sample is drawn and re-inserted again. But this would not make sense.

Therefore a second configuration shown in Fig. 5.4 has been designed. As for the previous design, in red the microfluidic network is reported, in grey the heater, in magenta the pneumatic valves, in blue the bottom metal contact of the sensors, in white the mesa, in orange the SU-8 via holes and in green the top metal contact.
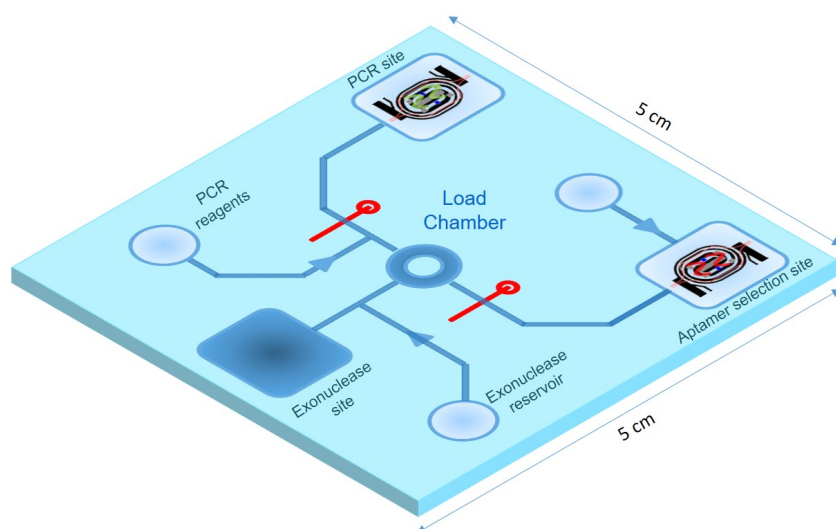
Figure 5.4. New chip design for on chip SELEX with a load-lock chamber.

This design involves a central chamber to load the sample which will pass through it before going in all other sites. In this way you can use a syringe pump to push and pull the sample in the different sites to implement the several cycles (at least 6-8) for the SELEX selection.

The sample, passing through the channel, is mixed together with the PCR reagents and reaches the PCR chamber. A pneumatic valve confines the sample in the reaction chamber so as it's possible to implement the thermal cycles necessary for the PCR amplification. Indeed the site is provided with spiral heater and temperature and light sensors to monitor respectively the temperature and the amount of amplified DNA. Subsequently the sample is pulled and then pushed towards the site where the exonuclease, present in a reservoir, will cause ds-DNA to reduce to ss-DNA. In fact the fluid, passing close to the trigger valve connected to the exonuclease reservoir, will bring the exonuclease to the following site. After the time necessary to perform this step, the sample is pulled and pushed again this time towards the site for the aptamers selection. In this design, as in the previous ones, only the positive selection is foreseen: the target is immobilized on the surface and the aptamer is complementary to the immobilized target. In future chip developments, I will try to also provide for the negative and competitive selections to increase the purity of the sample. The ss-DNA is then pushed towards the selection site where only the oligonucleotides complementary to the target are immobilized, the others will be washed away with the buffer solution and will come out to the waste. At this point, closing the pneumatic valve at the entrance of the chamber for a few minutes, it's possible to turn on the heater to break the aptamer/target bonds. Opening the valve and pulling again, the sample with the selected aptamers can be collected and pushed toward the PCR site to start a new SELEX cycle.

Conclusions

The present thesis described the development of a LoC for the implementation of the SELEX technique. The project required a multidisciplinary approach: diverse areas of knowledge such as microfabrication techniques, biology, chemistry, physics, electronics and fluid behavior were called upon. Thanks to several collaborations a first idea of SELEX chip was developed. We decided to proceed with a modular design of the different parts and their subsequent manifacture, taking into account the technological compatibility of the different steps.

In particular, a device that can be used as a multifunctional platform for several purposes was developed. For the first time, the integration on a single glass substrate of different thin film technologies in order to develop a compact and versatile device for on-chip thermal treatments and on-chip detection of biomolecules has been achieved. The proposed DARWIN'S device hosts thin metal films acting as heating sources; hydrogenated amorphous silicon diodes acting both as temperature sensors to monitor the temperature distribution and photosensors for the on-chip detection and a ground plane ensuring that the heater operation does not affect the photodiode currents.

All its parts have been purposely designed with proper specifications. The heater design was focused on the research of optimum performance in terms of thermal field uniformity; the use of a powerful finite element analysis software (COMSOL Multiphysics) allowed to find a satisfactory solution to the problem in the double spiral geometry. Based on this choice, the complete system integrating on the same glass substrate a-Si:H temperature and light sensors on a multilevel structure was achieved.

The device integration has been developed taking into account the compatibility between the whole fabrication process and the characteristics of the glass substrate, leading to an optimization of the technological steps sequence and to the choice of appropriate thin film materials and thicknesses.

The characterization has been performed through I-V curve for both photosensors and temperature sensors, Quantum Yield for the photosensors, thermal characterization with a thermo-camera for heaters and temperature sensors.

During the experiments, the DARWIN'S has been connected to an electronic system driving the heaters and controlling the temperature and light sensors. Each time it has been optically and thermally coupled with another glass hosting a microfluidic network made in polydimethylsiloxane with thermally actuated microvalves and a process chamber.

This platform was used for different experiments. First of all it has been tested for

the implementation of DNA amplification through the Polymerase Chain Reaction (PCR) with thermal cycling among three different temperatures on a single site. The successful DNA amplification has been verified off-chip by using a standard fluorometer.

DARWIN'S was also used to test the separation module. The thin film metal heater provided the heating at 90-95 °C for the separation of the two strands of DNA produced during the PCR step. Another glass hosted a PDMS microfluidic chip functionalized with streptavidin, by means of polymer brushes. A very good recovery of ss-DNA was obtained. Howeverwith this approach, it is not possible to use the functionalized site more than once due to the strong streptavidin/biotin bond, very difficult to break. . In order to address this issue the separation by exonuclease enzyme is envisaged.

Other projects have also been reported:

- DARWIN'S application for viral DNA amplification and real-time quantitative detection under constant temperature (65 °C).

- the design of proper trench geometries useful for increasing the thermal resistance of microheaters fabricated on glass substrates, thus decreasing the thermal dissipation of the devices. A significant result was only achieved when a big part of the thermal mass under the microheater was removed.

- the development of a lab-on-chip system for the diagnosis and follow-up of celiac disease. The system optically couples a glass-PDMS microfluidic network, where an immunoassay recognition occurs, and a glass hosting an array of amorphous silicon photosensors, which detect the chemiluminescent reactions occurring inside the microfluidic channels. The system has been tested using rabbit serum.

- the development of a lab-on-chip system based on a novel type of Enzyme Linked Aptamer Assay (ELAA). The device is composed by a poly(dimethylsiloxane) (PDMS) microfluidic network, having four parallel channels, aligned with the columns of an array of amorphous silicon photosensors deposited on a glass substrate. The result demonstrates that this novel ELAA method can be successfully implemented in lab-on-chip systems for detecting OTA, opening the way to a rapid and inexpensive tool for the analysis of feed and foodstuffs.

As a future developments for the project of my PhD, the next ideas are presented:

- on chip detection for the PCR experiment;

- tests on the aptamer selection site;

- integration and fabrication of the different modules on one single substrate to perform an on-chip SELEX. A final design has been developed and presented. From a microfluidic point of view, it comprises a load-lock chamber to push and pull the sample in the different sites, trigger valves and pneumatic valves. Regarding the electronic part, the DARWIN'S structure, whose design, fabrication and testing is the core of this thesis, is used for the three SELEX modules.

List of Pubblications

Giulia Petrucci received the master degree in Biomedical Engineering at the University of Rome "La Sapienza" in 2013. During her PhD in Information and Communication Technology (ICT- curriculum Electronic Engineering) at the same University, she worked at Laboratory of Microelectronic Technologies and the Characterization Laboratory at DIET, at the Department of Chemistry at "Sapienza" University of Rome and at INESC-MN (Instituto de Engenharia de Sistemas e Computadores para os Microsistemas e as Nanotecnologias) research center in Lisbon. Her research activity is focused on development of Lab-on-Chip system integrating microfluidics, photosensors and thin film heaters.

JOURNALS

1. **G. Petrucci**, D. Caputo, N. Lovecchio, F. Costantini, I. Legnini, I. Bozzoni, A. Nascetti, G. de Cesare, "Multifunctional System-on-Glass for Lab-on-Chip applications", Biosensors and Bioelectronics, *in press* (Available on line 20 June 2016)- http://dx.doi.org/10.1016/j.bios.2016.08.060;

2. F. Costantini, C. Sberna, **G. Petrucci**, M. Reverberi, F. Domenici, C. Fanelli, C. Manetti, G. de Cesare, M. De Rosa, A. Nascetti and D. Caputo, "Aptamer-Based Sandwich Assay for on Chip detection of Ochratoxin A by an Array of Amorphous Silicon Photosensors", Sensors and Actuators B: Chemical, Vol. 230, pp. 31-39 (2016), DOI: 10.1016/j.snb.2016.02.036;

3. F. Costantini, C. Sberna, **G. Petrucci**, C. Manetti, G. de Cesare, A. Nascetti, D. Caputo, "Lab-on-chip system combining a microfluidic-ELISA with an array of amorphous silicon photosensors for the detection of celiac disease epitopes", Sensing and BioSensing Research, Vol. 6, pp. 51-58 (2015), http://dx.doi.org/10.1016/j.sbsr.2015.11.003;

4. A. Scorzoni, D. Caputo, **G. Petrucci**, P. Placidi, S. Zampolli, G. de Cesare, M. Tavernelli, A. Nascetti, "Design and experimental characterization of thin film heaters on glass substrate for Lab-on-Chip applications", Sensors and Actuators

A: Physical, Vol. 229, pp. 203-210 (2015), http://dx.doi.org/10.1016/j.sna.2015.03.011;

5. M. Mirasoli, M. Zangheri, A. Roda, F. Bonvicini, G. Gallinella, A. Nascetti, G. De Cesare, **G. Petrucci**, N. Lovecchio, D. Caputo, "On-chip LAMP-BART reaction for viral DNA real-time bioluminescence detection", *submitted to* Biosensors and Bioelectronics.

CONFERENCES

1. F. Costantini, N. Lovecchio, **G. Petrucci**, M. Nardecchia, G. de Cesare, A. Nascetti, D. Caputo, "A versatile aptasensor material for lab-on-chip analytical applications", *submitted to* 5th International Conference on Biosensing Technology, 7-10 MAy 2017, Riva del Garda, Italy;

2. D. Caputo, **G. Petrucci**, F. Costantini, N. Lovecchio, M. Nardecchia, A. Nascetti, G. de Cesare, "Lab-on-Chip system based on thin film technologies for real-time PCR", *submitted to* 5th International Conference on Biosensing Technology, 7-10 MAy 2017, Riva del Garda, Italy;

3. N. Lovecchio, M. Nardecchia, A. Buzzin, **G. Petrucci**, F. Costantini, A. Nascetti, G. de Cesare, D. Caputo, "In-Channel electrowetting technology for lab-on-chip applications", *submitted to* 5th International Conference on Biosensing Technology, 7-10 MAy 2017, Riva del Garda, Italy;

4. **G. Petrucci**, N. Lovecchio, M. Nardecchia, C. Parrillo, F. Costantini, A. Nascetti, G. de Cesare, D. Caputo, "Enhancement in pdms-based microfluidic network for on chip thermal treatment of biomolecules" *submitted to* AISEM 2017 Conference, February 21-23 2014, Lecce, Italy;

5. M. Nardecchia , D. Paglialunga, **G. Petrucci**, N. Lovecchio, F. Costantini, G. de Cesare, D. Caputo, A. Nascetti , "Autonomuous microfluidic capillary network for on chip detection of chemiluminescence" *submitted to* AISEM 2017 Conference, February 21-23 2014, Lecce, Italy;

6. N. Lovecchio, F. Costantini, V. Viri, M. Nardecchia, **G. Petrucci**, M. Tucci, P. Mangiapane, A. Nascetti, G. de Cesare, D. Caputo, "Optoelectronic system-on- glass for on-chip detection of fluorescence" *submitted to* AISEM 2017 Conference, February 21-23 2014, Lecce, Italy;

7. I. F. Pinto, **G. Petrucci**, R. R. G. Soares, V. Chu, M. R. Aires-Barros, J. P. Conde, A. M. Azevedo, "A nanoliter-scale chromatography system with integrated pneumatic valves for the rapid screening of multimodal ligand-target interactions", ISPPP2016, 6-9 November 2016 Salzburg-Austria;

8. D. Caputo, F. Costantini, N. Lovecchio, V. Viri, M. Tucci, P. Mangiapane, A. Ruggi, **G. Petrucci**, A. Nascetti and G. de Cesare, "Highly miniaturized system for on-chip detection of DNA", in Proceedings of 20th International Conference on Miniaturized Systems for Chemistry and Life Sciences 9-13 October, 2016, Dublin, Ireland, pp. 1234-1235 (2016);

9. I. F. Pinto, D. R. Santos, **G. Petrucci**, R. R. G. Soares, M. R. Aires-Barros, V. Chu, J. P. Conde, A. M. Azevedo, "Development of a microfluidic device with integrated valves and photodiodes for rapid optimization of chromatography separations of monoclonal antibodies", in Proceedings of 20th International Conference on Miniaturized Systems for Chemistry and Life Sciences 9-13 October, 2016, Dublin, Ireland, pp. 1424-1425 (2016);

10. D. Caputo, E. Parisi, A. Nascetti, M. Mirasoli, M. Nardecchia, N. Lovecchio, **G. Petrucci**, F. Costantini, A. Roda, G. de Cesare, "Integration of Amorphous Silicon Balanced Photodiodes and Thin Film Heaters for Biosensing Application", XXX Conference Eurosensors2016, 4-7 September 2016, Budapest- Hungary, in Procedia Engineering, Vol. 168, pp. 1434-1437 (2016);

11. M. Nardecchia, E. Bellini, P.R. Llorca, D. Caprini, N. Lovecchio, **G. Petrucci**, D. Caputo, G. de Cesare, A. Nascetti, "Integration of Capillarity and EWOD Technologies for Autonomous and Low-Power Consumption Micro-Analytical Systems", XXX Conference Eurosensors2016, 4-7 September 2016, Budapest-Hungary, in Procedia Engineering, Vol. 168, pp. 1370-1373 (2016);

12. **G. Petrucci**, N. Lovecchio, F. Costantini, A. Nascetti, G. de Cesare, D. Caputo, "Integrated optoelectronic system for biomolecular analysis based on thin film technologies", BIOSENSORS 2016 Conference, 25-27 May 2016, Gothenburg- Sweden;

13. **G. Petrucci**, F. Costantini, M. De Rosa, L. Tedeschi, C. Domenici, G. de Cesare, A. Nascetti, D. Caputo, "Design of a SELEX-chip for aptamer selection", BIOSENSORS 2016 Conference, 25-27 May 2016, Gothenburg- Sweden ;

14. N. Lovecchio, D. Caputo, **G. Petrucci**, A. Nascetti, M. Nardecchia, F. Costantini, G. de Cesare, "Amorphous silicon temperature sensors integrated with thin film heaters for thermal treatments of biomolecules", 3° Convegno Nazionale Sensori - Rome 3-5 February 2016, *in press* on Procedia Engineering;

15. N. Lovecchio, **G. Petrucci**, D. Caputo, S. Alameddine, M. Carpentiero, L. Martini, E. Parisi, A. Nascetti and G. de Cesare- "Thermal control system based on thin film heaters and amorphous silicon diodes", in Proceedings of 6th IEEE International Workshop on Advances in Sensors and Interfaces (IWASI), Gallipoli, Italy, 18-19 June 2015, pp.277-282, doi:10.1109/IWASI.2015.7184977 (2015);

16. F. Costantini, A. Nascetti, C. Sberna, **G. Petrucci**, C. Manetti, D. Caputo, G. de Cesare, "Fully integrated ochratoxin-A biosensor functionalized with an aptamer-brush polymer layer", BITE 2015 (4th International Conference on Bio-Sensing Technology), 10 - 13 May 2015, Lisbon, Portugal;

17. F. Costantini, A. Nascetti, C. Sberna, **G. Petrucci**, C. Manetti, D. Caputo, G. de Cesare, "Detection of celiac desease biomarkers bymonitoring of chemiluminescence kinetics", BITE 2015 (4th International Conference on Bio-Sensing Technology), 10 - 13 May 2015, Lisbon, Portugal;

18. **G. Petrucci**, D. Caputo, G. de Cesare, S. Alameddine, N. Lovecchio, A. Nascetti- "Thermal Characterization Of Thin Film Heater For Lab-On-Chip Application", in Proceedings of XVIII AISEM Annual Conference, 02-05 February 2015, Trento, Italy, DOI: 10.1109/AISEM.2015.7066835;

19. N. Lovecchio, D. Caputo, A. Nascetti, **G. Petrucci**, A. Zahra, G. de Cesare - "Drop Position Sensing In Digital Microfluidics Based On Capacitance Measurement", in Proceedings of XVIII AISEM Annual Conference, 02-05 February 2015, Trento, Italy, DOI: 10.1109/AISEM.2015.7066850;

20. D. Caprini, D. Caputo, G. de Cesare, **G. Petrucci**, A. Nascetti- "Rapid Prototyping Of Glass Microfluidic Chips Based On Autonomous Capillary Networks For Physiological Solutions", in Proceedings of XVIII AISEM Annual Conference, 02-05 February 2015, Trento, Italy, DOI: 10.1109/AISEM.2015.706 6839;

21. A. Zahra, D. Caputo, A. Nascetti, **G. Petrucci**, N. Lovecchio, R. Scipinotti, G. de Cesare- "Thermally actuated microfluidic system for lab on chip applications", in Proceedings of XVIII AISEM Annual Conference, 02-05 February 2015, Trento, Italy, DOI: 10.1109/AISEM.2015.7066845;

22. F. Costantini, A. Nascetti, **G. Petrucci**, C. Manetti, D. Caputo, G. de Cesare - "Microfluidic chip with integrated amorphous silicon photosensors for Point-of-Care testing", in Proceedings of 18th International Conference on Miniaturized Systems for Chemistry and Life Sciences, 26-30 October 2014, San Antonio, Texas, USA, pp. 2053-2055 (2014), ISBN: 978-097980647-6;

23. A. Scorzoni, M. Tavernelli, P. Placidi, P. Valigi, S. Zampolli, D. Caputo, **G. Petrucci**, A. Nascetti, "Improvement of the Thermal Resistance of Thin Film Heaters on Glass Substrate for Lab-on-Chip Applications", in Procedia Engineering, vol. 87, 959-962 (2014), presented at the EUROSENSORS 2014 Conference, 7-10 September 2014, Brescia, Italy, doi:10.1016/j.proeng.2014.11. 316;

24. A. Scorzoni, M. Tavernelli, P. Placidi, P. Valigi, D. Caputo, G. de Cesare, **G. Petrucci**, A. Nascetti, "Thermal characterization of a thin film heater on glass substrate for lab-on-chip applications", in Proceedings of IEEE Instrumentation and Measurement Technology Conference (I2MTC), Montevideo, Uruguay, 12-15 May 2014, art. no. 6860910, pp. 1089-1094 (2014), DOI: 10.1109/I2MTC. 2014.6860910.

Bibliography

[1] ANDERSON, J. R., CHIU, D. T., WU, H., SCHUELLER, O., AND WHITESIDES, G. M. Fabrication of microfluidic systems in poly (dimethylsiloxane). *Electrophoresis*, **21** (2000), 27.

[2] ASHLEY, J., JI, K., AND LI, S. F. Selection of bovine catalase aptamers using non-selex. *Electrophoresis*, **33** (2012), 2783.

[3] ASIELLO, P. J. AND BAEUMNER, A. J. Miniaturized isothermal nucleic acid amplification, a review. *Lab on a Chip*, **11** (2011), 1420.

[4] ASSOCIATION, G. P. ET AL. *Physical properties of glycerine and its solutions.* Glycerine Producers' Association (1963).

[5] AU, A. K., LAI, H., UTELA, B. R., AND FOLCH, A. Microvalves and micropumps for biomems. *Micromachines*, **2** (2011), 179.

[6] BEREZOVSKI, M., MUSHEEV, M., DRABOVICH, A., AND KRYLOV, S. N. Non-selex selection of aptamers. *Journal of the American Chemical Society*, **128** (2006), 1410.

[7] BEREZOVSKI, M. V., MUSHEEV, M. U., DRABOVICH, A. P., JITKOVA, J. V., AND KRYLOV, S. N. Non-selex: selection of aptamers without intermediate amplification of candidate oligonucleotides. *Nature protocols*, **1** (2006), 1359.

[8] BYRNE, M. B., TRUMP, L., DESAI, A. V., SCHOOK, L. B., GASKINS, H. R., AND KENIS, P. J. Microfluidic platform for the study of intercellular communication via soluble factor-cell and cell-cell paracrine signaling. *Biomicrofluidics*, **8** (2014), 044104.

[9] CAPUTO, D. AND DE CESARE, G. New a-si: H two-terminal switching device for active display. *Journal of non-crystalline solids*, **198** (1996), 1134.

[10] CAPUTO, D., DE CESARE, G., MANETTI, C., NASCETTI, A., AND SCIPINOTTI, R. Smart thin layer chromatography plate. *Lab on a Chip*, **7** (2007), 978.

[11] CAPUTO, D., DE CESARE, G., NARDINI, M., NASCETTI, A., AND SCIPINOTTI, R. Monitoring of temperature distribution in a thin film heater by an array of a-si: H temperature sensors. *IEEE Sensors Journal*, **12** (2012), 1209.

[12] CAPUTO, D., DE CESARE, G., NASCETTI, A., AND SCIPINOTTI, R. a-si: H temperature sensor integrated in a thin film heater. *physica status solidi (a)*, **207** (2010), 708.

[13] CHIOU, J., MATSUDAIRA, P., SONIN, A., AND EHRLICH, D. A closed-cycle capillary polymerase chain reaction machine. *Analytical chemistry*, **73** (2001), 2018.

[14] CHITTICK, R., ALEXANDER, J., AND STERLING, H. The preparation and properties of amorphous silicon. *Journal of the Electrochemical Society*, **116** (1969), 77.

[15] COSTANTINI, F., SBERNA, C., PETRUCCI, G., MANETTI, C., DE CESARE, G., NASCETTI, A., AND CAPUTO, D. Lab-on-chip system combining a microfluidic-elisa with an array of amorphous silicon photosensors for the detection of celiac disease epitopes. *Sensing and Bio-Sensing Research*, **6** (2015), 51.

[16] COSTANTINI, F., ET AL. On-chip detection of multiple serum antibodies against epitopes of celiac disease by an array of amorphous silicon sensors. *RSC Advances*, **4** (2014), 2073.

[17] COSTANTINI, F., ET AL. Aptamer-based sandwich assay for on chip detection of ochratoxin a by an array of amorphous silicon photosensors. *Sensors and Actuators B: Chemical*, **230** (2016), 31.

[18] COX, J. C., RUDOLPH, P., AND ELLINGTON, A. D. Automated rna selection. *Biotechnology progress*, **14** (1998), 845.

[19] DANIELS, D. A., CHEN, H., HICKE, B. J., SWIDEREK, K. M., AND GOLD, L. A tenascin-c aptamer identified by tumor cell selex: systematic evolution of ligands by exponential enrichment. *Proceedings of the National Academy of Sciences*, **100** (2003), 15416.

[20] DARMOSTUK, M., RIMPELOVA, S., GBELCOVA, H., AND RUML, T. Current approaches in selex: An update to aptamer selection technology. *Biotechnology advances*, **33** (2015), 1141.

[21] DE CESARE, G., CAPUTO, D., AND TUCCI, M. Electrical properties of ito/crystalline-silicon contact at different deposition temperatures. *IEEE Electron Device Letters*, **33** (2012), 327.

[22] DE CESARE, G., GAVESI, M., PALMA, F., AND RICCO, B. A novel a-si: H mechanical stress sensor. *Thin solid films*, **427** (2003), 191.

[23] DE CESARE, G., NASCETTI, A., AND CAPUTO, D. Amorphous silicon pin structure acting as light and temperature sensor. *Sensors*, **15** (2015), 12260.

[24] DJORDJEVIC, M. Selex experiments: new prospects, applications and data analysis in inferring regulatory pathways. *Biomolecular engineering*, **24** (2007), 179.

[25] DUARTE, S., LINO, C., AND PENA, A. Mycotoxin food and feed regulation and the specific case of ochratoxin a: a review of the worldwide status. *Food Additives and Contaminants*, **27** (2010), 1440.

[26] DUFFY, D. C., MCDONALD, J. C., SCHUELLER, O. J., AND WHITESIDES, G. M. Rapid prototyping of microfluidic systems in poly (dimethylsiloxane). *Analytical chemistry*, **70** (1998), 4974.

[27] EATON, R. M., SHALLCROSS, J. A., MAEL, L. E., MEARS, K. S., MINKOFF, L., SCOVILLE, D. J., AND WHELAN, R. J. Selection of dna aptamers for ovarian cancer biomarker he4 using ce-selex and high-throughput sequencing. *Analytical and bioanalytical chemistry*, **407** (2015), 6965.

[28] EL-ALI, J., PERCH-NIELSEN, I. R., POULSEN, C. R., BANG, D. D., TELLEMAN, P., AND WOLFF, A. Simulation and experimental validation of a su-8 based pcr thermocycler chip with integrated heaters and temperature sensor. *Sensors and Actuators A: Physical*, **110** (2004), 3.

[29] ELLINGTON, A. AND SZOSTAK, J. Selection in vitro of single-stranded dna molecules that fold into specific ligand-binding structures. *Nature*, **355** (1992), 850.

[30] ELLINGTON, A. D. AND SZOSTAK, J. W. In vitro selection of rna molecules that bind specific ligands. *nature*, **346** (1990), 818.

[31] EULBERG, D., BUCHNER, K., MAASCH, C., AND KLUSSMANN, S. Development of an automated in vitro selection protocol to obtain rna-based aptamers: identification of a biostable substance p antagonist. *Nucleic acids research*, **33** (2005), e45.

[32] FETTINGER, J., MANZ, A., LÜDI, H., AND WIDMER, H. Stacked modules for micro flow systems in chemical analysis: concept and studies using an enlarged model. *Sensors and Actuators B: Chemical*, **17** (1993), 19.

[33] FORDYCE, P., DIAZ-BOTIA, C., DERISI, J., AND GOMEZ-SJOBERG, R. Systematic characterization of feature dimensions and closing pressures for microfluidic valves produced via photoresist reflow. *Lab on a Chip*, **12** (2012), 4287.

[34] FRITZSCHE, H., TANIELIAN, M., TSAI, C., AND GACZI, P. Hydrogen content and density of plasma-deposited amorphous silicon-hydrogen. *Journal of Applied Physics*, **50** (1979), 3366.

[35] GOERTZ, P. W., COX, J. C., AND ELLINGTON, A. D. Automated selection of aminoglycoside aptamers. *Journal of the Association for Laboratory Automation*, **9** (2004), 150.

[36] HANSEN, C. AND QUAKE, S. R. Microfluidics in structural biology: smaller, faster... better. *Current opinion in structural biology*, **13** (2003), 538.

[37] HELLER, M. J. Dna microarray technology: devices, systems, and applications. *Annual review of biomedical engineering*, **4** (2002), 129.

[38] HIERLEMANN, A., BRAND, O., HAGLEITNER, C., AND BALTES, H. Microfabrication techniques for chemical/biosensors. *Proceedings of the IEEE*, **91** (2003), 839.

[39] HOWBROOK, D. N., VAN DER VALK, A. M., O'SHAUGHNESSY, M. C., SARKER, D. K., BAKER, S. C., AND LLOYD, A. W. Developments in microarray technologies. *Drug discovery today*, **8** (2003), 642.

[40] HSIEH, T.-M., LUO, C.-H., HUANG, F.-C., WANG, J.-H., CHIEN, L.-J., AND LEE, G.-B. Enhancement of thermal uniformity for a microthermal cycler and its application for polymerase chain reaction. *Sensors and Actuators B: Chemical*, **130** (2008), 848.

[41] HSIEH, T.-M., LUO, C.-H., WANG, J.-H., LIN, J.-L., LIEN, K.-Y., AND LEE, G.-B. A two-dimensional, self-compensated, microthermal cycler for one-step reverse transcription polymerase chain reaction applications. *Microfluidics and nanofluidics*, **6** (2009), 797.

[42] HUANG, C.-J., LIN, H.-I., SHIESH, S.-C., AND LEE, G.-B. Integrated microfluidic system for rapid screening of crp aptamers utilizing systematic evolution of ligands by exponential enrichment (selex). *Biosensors and bioelectronics*, **25** (2010), 1761.

[43] HÜNNIGER, T., WESSELS, H., FISCHER, C., PASCHKE-KRATZIN, A., AND FISCHER, M. Just in time-selection: A rapid semiautomated selex of dna aptamers using magnetic separation and beaming. *Analytical chemistry*, **86** (2014), 10940.

[44] HYBARGER, G., BYNUM, J., WILLIAMS, R. F., VALDES, J. J., AND CHAMBERS, J. P. A microfluidic selex prototype. *Analytical and bioanalytical chemistry*, **384** (2006), 191.

[45] ILIUK, A. B., HU, L., AND TAO, W. A. Aptamer in bioanalytical applications. *Analytical chemistry*, **83** (2011), 4440.

[46] JHA, S. K., JOO, G.-S., RA, G.-S., LEE, H. H., AND KIM, Y.-S. Development of pcr microchip for early cancer risk prediction. *IEEE Sensors Journal*, **11** (2011), 2065.

[47] JIANG, Y., FANG, X., AND BAI, C. Signaling aptamer/protein binding by a molecular light switch complex. *Analytical chemistry*, **76** (2004), 5230.

[48] JUNG, W., HAN, J., CHOI, J.-W., AND AHN, C. H. Point-of-care testing (poct) diagnostic systems using microfluidic lab-on-a-chip technologies. *Microelectronic Engineering*, **132** (2015), 46.

[49] KNIPP, D., HERZOG, P. G., AND STIEBIG, H. Stacked amorphous silicon color sensors. *IEEE Transactions on Electron Devices*, **49** (2002), 170.

[50] KOPF-SILL, A. R. Profile successes and challenges of lab-on-a-chip. *Lab on a Chip*, **2** (2002), 42N.

[51] LAO, A. I., LEE, T. M., HSING, I.-M., AND IP, N. Y. Precise temperature control of microfluidic chamber for gas and liquid phase reactions. *Sensors and Actuators A: Physical*, **84** (2000), 11.

[52] LEE, S.-J. J. AND SUNDARARAJAN, N. *Microfabrication for microfluidics.* Artech House (2010).

[53] LI, Q., ZHAO, X., LIU, H., AND QU, F. Low ph capillary electrophoresis application to improve capillary electrophoresis-systematic evolution of ligands by exponential enrichment. *Journal of Chromatography A*, **1364** (2014), 289.

[54] LIN, H.-I., WU, C.-C., YANG, C.-H., CHANG, K.-W., LEE, G.-B., AND SHIESH, S.-C. Selection of aptamers specific for glycated hemoglobin and total hemoglobin using on-chip selex. *Lab on a Chip*, **15** (2015), 486.

[55] LOU, X., ET AL. Micromagnetic selection of aptamers in microfluidic channels. *Proceedings of the National Academy of Sciences*, **106** (2009), 2989.

[56] LUPPA, P. B., SOKOLL, L. J., AND CHAN, D. W. Immunosensors- principles and applications to clinical chemistry. *Clinica Chimica Acta*, **314** (2001), 1.

[57] MANSOOR, M., HANEEF, I., AKHTAR, S., DE LUCA, A., AND UDREA, F. Silicon diode temperature sensors—a review of applications. *Sensors and Actuators A: Physical*, **232** (2015), 63.

[58] MANZ, A., GRABER, N., AND WIDMER, H. Á. Miniaturized total chemical analysis systems: a novel concept for chemical sensing. *Sensors and actuators B: Chemical*, **1** (1990), 244.

[59] MANZ, A., HARRISON, D., FETTINGER, J., VERPOORTE, E., LUDI, H., AND WIDMER, H. Integrated electroosmotic pumps and flow manifolds for total chemical analysis systems. In *Solid-State Sensors and Actuators, 1991. Digest of Technical Papers, TRANSDUCERS'91., 1991 International Conference on*, pp. 939–941. IEEE (1991).

[60] MARIMUTHU, C., TANG, T.-H., TOMINAGA, J., TAN, S.-C., AND GOPINATH, S. C. Single-stranded dna (ssdna) production in dna aptamer generation. *Analyst*, **137** (2012), 1307.

[61] MCKEAGUE, M. AND DEROSA, M. C. Challenges and opportunities for small molecule aptamer development. *Journal of nucleic acids*, **2012** (2012).

[62] MELIN, J. AND QUAKE, S. R. Microfluidic large-scale integration: the evolution of design rules for biological automation. *Annu. Rev. Biophys. Biomol. Struct.*, **36** (2007), 213.

[63] MENDONSA, S. D. AND BOWSER, M. T. In vitro evolution of functional dna using capillary electrophoresis. *Journal of the American Chemical Society*, **126** (2004), 20.

[64] Miralles, V., Huerre, A., Malloggi, F., and Jullien, M.-C. A review of heating and temperature control in microfluidic systems: techniques and applications. *Diagnostics*, **3** (2013), 33.

[65] Mirasoli, M., Nascetti, A., Caputo, D., Zangheri, M., Scipinotti, R., Cevenini, L., De Cesare, G., and Roda, A. Multiwell cartridge with integrated array of amorphous silicon photosensors for chemiluminescence detection: development, characterization and comparison with cooled-ccd luminograph. *Analytical and bioanalytical chemistry*, **406** (2014), 5645.

[66] Müller, U. R. and Nicolau, D. V. *Microarray technology and its applications.* Springer (2005).

[67] Notomi, T., Mori, Y., Tomita, N., and Kanda, H. Loop-mediated isothermal amplification (lamp): principle, features, and future prospects. *Journal of Microbiology*, **53** (2015), 1.

[68] Novo, P., Chu, V., and Conde, J. P. Integrated fluorescence detection of labeled biomolecules using a prism-like pdms microfluidic chip and lateral light excitation. *Lab on a Chip*, **14** (2014), 1991.

[69] Oh, K. W. and Ahn, C. H. A review of microvalves. *Journal of micromechanics and microengineering*, **16** (2006), R13.

[70] Petrucci, G., Caputo, D., Lovecchio, N., Costantini, F., Legnini, I., Bozzoni, I., Nascetti, A., and de Cesare, G. Multifunctional system-on-glass for lab-on-chip applications. *Biosensors and Bioelectronics*, (2016).

[71] Petrucci, G., Caputo, D., Nascetti, A., Lovecchio, N., Parisi, E., Alameddine, S., de Cesare, G., and Zahra, A. Thermal characterization of thin film heater for lab-on-chip application. In *AISEM Annual Conference, 2015 XVIII*, pp. 1–4. IEEE (2015).

[72] Pimentel, A. C., Pereira, A., Chu, V., Prazeres, D., and Conde, J. Detection of chemiluminescence using an amorphous silicon photodiode. *IEEE Sensors Journal*, **3** (2007), 415.

[73] Polini, A., Mele, E., Sciancalepore, A. G., Girardo, S., Biasco, A., Camposeo, A., Cingolani, R., Weitz, D. A., and Pisignano, D. Reduction of water evaporation in polymerase chain reaction microfluidic devices based on oscillating-flow. *Biomicrofluidics*, **4** (2010), 036502.

[74] Quake, S. R. and Scherer, A. From micro-to nanofabrication with soft materials. *Science*, **290** (2000), 1536.

[75] Robertson, D. L. and Joyce, G. F. Selection in vitro of an rna enzyme that specifically cleaves single-stranded dna. *Nature*, **344** (1990), 467.

[76] Safavieh, M., Kanakasabapathy, M. K., Tarlan, F., Ahmed, M. U., Zourob, M., Asghar, W., and Shafiee, H. Emerging loop-mediated

isothermal amplification-based microchip and microdevice technologies for nucleic acid detection. *ACS Biomaterials Science & Engineering*, **2** (2016), 278.

[77] Samel, B., Chowdhury, M. K., and Stemme, G. The fabrication of microfluidic structures by means of full-wafer adhesive bonding using a poly (dimethylsiloxane) catalyst. *Journal of Micromechanics and Microengineering*, **17** (2007), 1710.

[78] Scorzoni, A., Caputo, D., Petrucci, G., Placidi, P., Zampolli, S., De Cesare, G., Tavernelli, M., and Nascetti, A. Design and experimental characterization of thin film heaters on glass substrate for lab-on-chip applications. *Sensors and Actuators A: Physical*, **229** (2015), 203.

[79] Scorzoni, A., Tavernelli, M., Placidi, P., Valigi, P., and Nascetti, A. Accurate analog temperature control of a thin film microheater on glass substrate for lab-on-chip applications. In *IEEE SENSORS 2014 Proceedings*, pp. 1216–1219. IEEE (2014).

[80] Sefah, K., Shangguan, D., Xiong, X., O'Donoghue, M. B., and Tan, W. Development of dna aptamers using cell-selex. *Nature protocols*, **5** (2010), 1169.

[81] Selva, B., Marchalot, J., and Jullien, M.-C. An optimized resistor pattern for temperature gradient control in microfluidics. *Journal of Micromechanics and Microengineering*, **19** (2009), 065002.

[82] Selva, B., Mary, P., and Jullien, M.-C. Integration of a uniform and rapid heating source into microfluidic systems. *Microfluidics and Nanofluidics*, **8** (2010), 755.

[83] Shangguan, D., Bing, T., and Zhang, N. Cell-selex: aptamer selection against whole cells. In *Aptamers Selected by Cell-SELEX for Theranostics*, pp. 13–33. Springer (2015).

[84] Smith, D. *Thin-film deposition: principles and practice*. McGraw Hill Professional (1995).

[85] Song, S., Wang, L., Li, J., Fan, C., and Zhao, J. Aptamer-based biosensors. *TrAC Trends in Analytical Chemistry*, **27** (2008), 108.

[86] Spear, W. and Le Comber, P. Substitutional doping of amorphous silicon. *Solid state communications*, **17** (1975), 1193.

[87] Stoltenburg, R., Reinemann, C., and Strehlitz, B. Flumag-selex as an advantageous method for dna aptamer selection. *Analytical and bioanalytical chemistry*, **383** (2005), 83.

[88] Stoltenburg, R., Schubert, T., and Strehlitz, B. In vitro selection and interaction studies of a dna aptamer targeting protein a. *PloS one*, **10** (2015), e0134403.

[89] Street, R. Hydrogenated amorphous silicon cambridge solid state science series, ed. cahn, rw, davis, ea, and ward, im (1991).

[90] Street, R. Amorphous silicon electronics. *MRS Bulletin*, **17** (1992), 70.

[91] Street, R. *Technology and applications of amorphous silicon*, vol. 37. Springer Science & Business Media (2013).

[92] Studer, V., Hang, G., Pandolfi, A., Ortiz, M., Anderson, W. F., and Quake, S. R. Scaling properties of a low-actuation pressure microfluidic valve. *Journal of applied physics*, **95** (2004), 393.

[93] Svobodová, M., Pinto, A., Nadal, P., and O'Sullivan, C. Comparison of different methods for generation of single-stranded dna for selex processes. *Analytical and bioanalytical chemistry*, **404** (2012), 835.

[94] Tang, J., Xie, J., Guo, L., Yan, Y., and Shao, N. Capillary electrophoresis as a tool for screening aptamer with high affinity and high specificity to ricin. *Frontiers of Chemistry in China*, **2** (2007), 431.

[95] Tuerk, C., Gold, L., et al. Systematic evolution of ligands by exponential enrichment: Rna ligands to bacteriophage t4 dna polymerase. *Science*, **249** (1990), 505.

[96] Unger, M. A., Chou, H.-P., Thorsen, T., Scherer, A., and Quake, S. R. Monolithic microfabricated valves and pumps by multilayer soft lithography. *Science*, **288** (2000), 113.

[97] Whitesides, G. M. The origins and the future of microfluidics. *Nature*, **442** (2006), 368.

[98] Whitesides, G. M., Ostuni, E., Takayama, S., Jiang, X., and Ingber, D. E. Soft lithography in biology and biochemistry. *Annual review of biomedical engineering*, **3** (2001), 335.

[99] Xia, Y. and Whitesides, G. M. Soft lithography. *Annual review of materials science*, **28** (1998), 153.

[100] Yamamoto, T., Fujii, T., and Nojima, T. Pdms–glass hybrid microreactor array with embedded temperature control device. application to cell-free protein synthesis. *Lab on a Chip*, **2** (2002), 197.

[101] Yokoyama, Y., Takeda, M., Umemoto, T., and Ogushi, T. Thermal micro pumps for a loop-type micro channel. *Sensors and Actuators A: Physical*, **111** (2004), 123.

[102] Zahra, A., Scipinotti, R., Caputo, D., Nascetti, A., and De Cesare, G. Design and fabrication of microfluidics system integrated with temperature actuated microvalve. *Sensors and Actuators A: Physical*, **236** (2015), 206.

[103] Zhang, C., Xu, J., Ma, W., and Zheng, W. Pcr microfluidic devices for dna amplification. *Biotechnology advances*, **24** (2006), 243.

[104] Zhang, Y. and Ozdemir, P. Microfluidic dna amplification—a review. *Analytica chimica acta*, **638** (2009), 115.

[105] Zhu, Y. and Petkovic-Duran, K. Capillary flow in microchannels. *Microfluidics and Nanofluidics*, **8** (2010), 275.

[106] Zou, Q., Sridhar, U., Chen, Y., and Singh, J. Miniaturized independently controllable multichamber thermal cycler. *IEEE sensors journal*, **3** (2003), 774.